

ADSORPTION AND CAPILLARY TRANSITION-CONTROLLED THERMAL DIODES  
AND SWITCHES USING HETEROGENEOUS NANOSTRUCTURES

A Dissertation by

Tadeh Avanesian

Master of Science, Shahid Bahonar University, Iran, 2013

Bachelor of Science, Shiraz University, Iran, 2010

Submitted to the Department of Mechanical Engineering  
and the faculty of the Graduate School of  
Wichita State University  
in partial fulfillment of  
the requirements for the degree of  
Doctor of Philosophy

December 2017

© Copyright 2017 by Tadeh Avanesian

All Rights Reserved

ADSORPTION AND CAPILLARY TRANSITION-CONTROLLED THERMAL DIODES  
AND SWITCHES USING HETEROGENEOUS NANOSTRUCTURES

The following faculty members have examined the final copy of this dissertation for form and content, and recommend that it be accepted in partial fulfillment of the requirement for the degree of Doctor of Philosophy, with a major in Mechanical Engineering.

---

Gisuk Hwang, Committee Chair

---

Vis Madhavan, Committee Member

---

Hamid Lankarani, Committee Member

---

Muhammad Rahman, Committee Member

---

Shuang Gu, Committee Member

Accepted for the College of Engineering

---

Royce Bowden, Dean

Accepted for the Graduate School

---

Dennis Livesay, Dean

## DEDICATION

To my beloved parents

## ACKNOWLEDGMENT

I wish to express my deep and sincere gratitude to Dr. Gisuk Hwang, faculty member of the Department of Mechanical Engineering at Wichita State University. His wide knowledge, logical way of thinking, understanding, and support have been of great value to me. Without his guidance, this research would not have been possible.

I extend gratitude to my committee members, Dr. Hamid Lankarani, Dr. Muhammad Rahman, Dr. Shuang Gu, and Dr. Vis Madhavan for their valuable comments and suggestions.

I take this opportunity to express my sincere gratitude to my father, mother, and brother for providing me spiritual and moral support.

My thanks also go to all faculty and staff of the Department of Mechanical Engineering for their constant support and guidance throughout the duration of my studies at Wichita State University.

## ABSTRACT

Thermal diodes and switches are systems that enable us to control thermal transport, preferentially in one direction, and switch “on”/“off” on demand. The main challenges of existing thermal diodes and switches are poor steady-state performance, limited operation conditions, slow transient response, and/or extremely difficult manufacturing. In this study, adsorption-controlled and capillary-controlled thermal diodes and switches are examined by employing argon gas-filled heterogeneous nanostructures using molecular simulations. For the adsorption-controlled mechanism, asymmetric adsorption onto the heterogeneous nanogap with respect to the different temperature gradient direction results in the asymmetric gas pressure and thermal accommodation coefficients (TACs), giving a maximum degree of diode,  $R_{max} \sim 7$ . For a thermal switch, Ar-filled nanogaps with two heterogeneous surfaces are designed to demonstrate a fast thermal switch mechanism without having extra mechanical controlling system with the maximum degree of thermal switch,  $S_{max} \sim 13$ . In order to achieve higher magnitudes of  $R$  and  $S$ , the adsorption and capillary transition on the heterogeneous nanostructures are elucidated using Ar-filled Pt-based nanogaps with one surface having nanoposts using Grand Canonical Monte Carlo Simulation (GCMC). The study shows that the nanoposts decrease capillary transition pressure at given temperature (or increase temperature at given pressure). The large thermal conductivity contrast between the controlled adsorption and capillary states using the structural and/or material heterogeneity is shown to allow for  $R_{max} \sim 140$  in a demonstrated thermal diode with operating temperatures  $-40 \text{ K} < \Delta T < +40 \text{ K}$ . It also leads to a new nanoscale thermal switch mechanism providing  $S_{max} \sim 45$  and  $\sim 170$  for  $\Delta T = 10 \text{ K}$  and  $60 \text{ K}$ , respectively, for a nanogap size of  $5 \text{ nm}$ . These results provide new insights into the design of advanced thermal management systems such as thermal transistors, thermal logic gates, and computers.

## TABLE OF CONTENTS

Chapter	Page
1-	INTRODUCTION AND LITERATURE REVIEW .....1
1.1	INTRODUCTION .....1
1.2	THERMAL DIODE .....2
1.2.1	Nonlinear thermal conduction.....4
1.2.2	Electronic thermal conduction .....4
1.2.3	Phononic thermal conduction .....6
1.2.3.1	Heterogeneous material junctions: solid/solid.....6
1.2.3.2	Heterogeneous junctions: solid/liquid .....8
1.2.3.3	Homogeneous junctions: asymmetric geometry.....8
1.2.3.4	Heterogeneous junctions: quantum system .....13
1.2.3.5	Homogeneous junction: asymmetric mass distribution.....13
1.2.3.6	Other approaches: assisted by external controller .....14
1.2.4	Nonlinear thermal convection.....16
1.2.5	Nonlinear thermal radiation .....18
1.2.6	Outlook for future research.....22
1.3	THERMAL SWITCH.....23
1.3.1	Micro- to macro-scale, mechanical-based thermal switch.....25
1.3.1.1	Differential thermal expansion thermal switches .....25
1.3.1.2	Gas-filled microgap .....26
1.3.1.3	Paraffin-based (phase change material) thermal switch .....27
1.3.1.4	Heat pipe.....28
1.3.2	Atomic-scale phononics-based thermal switch, transistors, and computers.....29
1.3.3	Outlook for future research.....31
1.4	CONCLUSION.....32
1.5	STATEMENT OF OBJECTIVE AND SCOPE OF PROPOSAL.....33
2-	ADSORPTION-CONTROLLED THERMAL DIODE IN HETEROGENEOUS NANOSTRUCTURES .....36
2.1	INTRODUCTION .....36
2.2	ADSORPTION-CONTROLLED THERMAL DIODE.....37
2.3	METHODOLOGY .....39
2.4	RESULTS AND DISCUSSION .....42
2.5	CONCLUSION.....47

TABLE OF CONTENTS (continued)

Chapter	Page
3- ADSORPTION-CONTROLLED THERMAL SWITCH IN HETEROGENEOUS NANOSTRUCTURES .....	49
3.1 INTRODUCTION .....	49
3.2 NON-EQUILIBRIUM MOLECULAR DYNAMICS SIMULATION (NEMD).....	51
3.3 VALIDATION OF NEMD RESULTS WITH KINETIC THEORY .....	54
3.4 RESULTS AND DISCUSSION .....	56
3.5 CONCLUSION.....	60
4- ADSORPTION-CAPILLARY TRANSITION IN HETEROGENEOUS NANOSTRUCTURES .....	61
4.1 INTRODUCTION .....	61
4.2 SIMULATION METHOD .....	65
4.3 SIMULATION VALIDATION.....	68
4.4 RESULTS AND DISCUSSION .....	70
4.4.1 Nanopost pitch distance ( $l_p^*$ ) effect.....	70
4.4.2 Nanopost height ( $l_z^*$ ) effect.....	72
4.4.3 Surface interaction ( $\varepsilon^*$ ) effect.....	74
4.4.4 Nanogap size ( $L_z$ ) effect.....	76
4.4.5 Hysteresis.....	77
4.5 CONCLUSION.....	79
5- CAPILLARY-CONTROLLED THERMAL DIODE IN HETEROGENEOUS NANOSTRUCTURES .....	81
5.1 INTRODUCTION .....	81
5.2 WORKING PRINCIPLE.....	83
5.3 SIMULATION METHOD .....	85
5.4 RESULTS AND DISCUSSION .....	88
5.4.1 Nanopillar height ( $l_z^*$ ) effect .....	88
5.4.2 Nanogap size ( $L_z$ ) effect.....	90
5.4.3 Surface interaction ( $\varepsilon^*$ ) effect in nanogaps with both bare surfaces .....	92
5.4.4 Surface interaction ( $\varepsilon^*$ ) effect in nanogaps with one structured surface....	94
5.5 CONCLUSION.....	96

TABLE OF CONTENTS (continued)

Chapter	Page
6- CAPILLARY-CONTROLLED THERMAL SWITCH IN HETEROGENEOUS NANOSTRUCTURES .....	98
6.1 INTRODUCTION .....	98
6.2 WORKING PRINCIPLE.....	100
6.3 SIMULATION METHOD .....	102
6.4 VALIDATION .....	104
6.5 RESULTS AND DISCUSSION .....	106
6.5.1 Nanopost height ( $l_z^*$ ) effect.....	106
6.5.2 Nanopost pitch distance ( $l_p^*$ ) effect.....	109
6.5.3 Surface interaction ( $\varepsilon^*$ ) effect.....	112
6.5.4 Temperature difference ( $\Delta T$ ) effect .....	117
6.6 CONCLUSION.....	119
7- CONCLUSION.....	121
7.1 CONTRIBUTIONS .....	121
7.2 PROPOSED FUTURE WORK .....	124
7.3 OUTLOOK.....	128
REFERENCES .....	131

## LIST OF FIGURES

Figure	Page
1.1.	Schematic of thermal diode principle showing heat flux, where $q_+$ is large when the temperature gradient is positive, and the reverse heat flux, $q_-$ , is minimal when the temperature gradient is reversed. Insert shows concept of thermal diode qualitatively. .... 3
1.2.	Experimental setup for the thermal diode using Cu/CuO <sub>2</sub> interface [14]. ..... 5
1.3.	Various interfacial structures between Ar/Kr materials for thermal diode using molecular dynamics simulations [5]. ..... 7
1.4.	Asymmetric nanostructure for the thermal diode using partially-unzipped carbon nanotube (PUCNTs) [32]. ..... 10
1.5.	A schematic drawing of water-filled heterogeneous wetting surfaces for thermal diode, $R_{\max} \sim 100$ [68]. ..... 17
1.6.	A schematic drawing of asymmetric photon scattering through pyramid collimator [11]. ..... 19
1.7.	Summary of previously reported degree of thermal rectification, $R$ , using both experimental and theoretical/computational approaches in nonlinear conduction, convection, and radiation heat transfer mechanisms. Variations of thermal diode (or rectification) with respect to operating temperature range (average temperature) and target thermal rectification (present study) are also shown. .... 22
1.8.	Schematic diagram of atomic-scale thermal transistor with thermal bath for thermal transport/control [92]. ..... 30
2.1.	A schematic of the adsorption-controlled thermal diode using gas-filled nanogap. (a) $\langle q_+ \rangle \gg 0$ for $T_1 > T_2$ , and (b) $\langle q_- \rangle \sim 0$ for $T_1 < T_2$ due to the adsorption-controlled asymmetric isotherm and thermal accommodation coefficient (TAC). The surface temperatures, $T_1$ and $T_2$ , heat fluxes, $\langle q_+ \rangle$ , and $\langle q_- \rangle$ , gas-solid interactions, $\epsilon_{sf,1}$ and $\epsilon_{sf,2}$ , nanogap size, $L_z$ , and the adsorbed particles are also shown. .... 37
2.2.	Variations of heat flux through the nanogap as a function of average surface temperature both in $\langle q_+ \rangle$ (solid symbols) and $\langle q_- \rangle$ (empty symbols) directions, for $\epsilon^* = 1.0, 0.75$ , and $0.5$ . The error bars and insets for the simulation setup are also shown. .... 41
2.3.	Variations of heat flux through the nanogap as a function of average surface temperature both in $\langle q_+ \rangle$ (solid symbols) and $\langle q_- \rangle$ (empty symbols) directions, for $\epsilon^* = 1.0, 0.75$ , and $0.5$ . The error bars and insets for the simulation setup are also shown. .... 42

LIST OF FIGURES (continued)

Figure	Page
2.4.	Variation of the degree of thermal diode (rectification) using the adsorption-controlled heat flux as a function of average nanogap temperature, for $\varepsilon^* = 1.0, 0.75,$ and $0.75$ [Eq. (1.2)]. Some error bars are smaller than the size of their corresponding symbols. .... 44
2.5.	The number density of adsorbed particles in the lower and upper surfaces for $\langle q_+ \rangle$ (solid symbols) and $\langle q_- \rangle$ (empty symbols), (a) $\varepsilon^* = 0.75,$ and (b) $\varepsilon^* = 0.5.$ The insets with the adsorbed Ar particles are also shown. Error bars are shown, but those are smaller than the size of their symbols. The number density of liquid Ar is also shown. .... 45
2.6.	Variations of the thermal accommodation coefficient, $aT,$ for (a) $\varepsilon^* = 1.0, 0.75$ and (b) $\varepsilon^* = 1.0, 0.5$ as a function of surface temperature both in $\langle q_+ \rangle$ (solid symbols) and $\langle q_- \rangle$ (empty symbols) directions. Error bars and insets with adsorbed particles are also shown. .... 46
2.7.	Average pressure within the nanogap far from the effect of gas-surface interaction both in $\langle q_+ \rangle$ (solid symbols) and $\langle q_- \rangle$ (empty symbols) directions for $\varepsilon^* = 1.0, 0.75,$ and $0.5.$ Error bars are smaller than symbol size. .... 47
3.1.	A schematic of the adsorption-controlled thermal switch. (a) Large heat flux for “on” mode by the high thermal accommodation coefficients and (b) small heat flux for “off” mode by poor thermal accommodation coefficients (adsorption-free surface on the middle surface). .... 52
3.2.	Comparison of the heat flux calculated for the “off” mode using NEMD and kinetic theory (KT) where $\varepsilon_1^* = \varepsilon_2^* = \varepsilon_3^* = 1.0$ ( $T_1 = 100$ K, $T_2 = 80$ K, and $T_3 = 100$ to $120$ K). Error bars are also shown. .... 55
3.3.	Variation of the Knudsen number, Kn, in the lower and upper nanogaps for $\varepsilon_3^* = 0.4, 0.5,$ and $1.0,$ and $T_3$ from $100$ to $120$ K. Error bars are also shown. .... 55
3.4.	Heat flux in the thermal switch in “off” mode ( $T_1 = 100$ K, $T_2 = 80$ K) as a function of $T_3$ from $100$ K to $120$ K for $\varepsilon_3^* = 0.4, 0.5,$ and $1.0$ (for both upper and lower nanogap). Error bars are also shown. .... 57
3.5.	Variations of the gas pressure, $\langle p \rangle$ in the lower and upper nanogaps as a function of $T_3$ from $100$ to $120$ K for $\varepsilon_3^* = 0.4, 0.5,$ and $1.0.$ Error bars are also shown. .... 58
3.6.	Variations of the degree of the thermal switch, $S,$ in the lower and upper nanogaps for $\varepsilon_3^* = 0.4, 0.5,$ and $1.0,$ and $T_3 = 100$ to $120$ K. Average heat fluxes are used for $S$ (no error bars). .... 59
4.1.	Schematic drawings of (a) nanogap with nanoposts on one surface and (b) nanogap with bare surfaces. The dimensions for the nanogap and nanoposts are also shown. .... 66

LIST OF FIGURES (continued)

Figure	Page
4.2.	Comparison of the predicted adsorption isotherm of Ar in a Pt-based nanogap, $L_z = 5$ nm, at $T = 87$ K using GCMC with the measured one for Ar in a MCM-41 with a 5.1 nm pore diameter [188]. ..... 69
4.3.	Variation of Ar number density, $n_f$ , for $l_z^* = 0.63$ , $\varepsilon^* = 1.0$ , and $l_p^* = 0$ (bare surface with $L_z \sim 2$ nm), 0.33, 0.5, 0.67, and 1.0 (bare surface with $L_z = 5$ nm); a) as a function of relative pressure, $\langle p_g \rangle / p_o$ , at $\langle T \rangle = 86.8$ K; b) as a function of temperature, $\langle T \rangle = 80$ to 140 K in $\langle p_g \rangle = 1.66$ atm. The insets correspond to the nanogaps with bare surfaces and one surface with nanoposts. (B) represents the bare surface. Error bars are too small to be observed. .... 71
4.4.	Variation of the Ar number density, $n_f$ , for $l_p^* = 0.5$ , $\varepsilon^* = 1.0$ , and $l_z^* = 0$ (bare surface with $L_z = 5$ nm), 0.23, 0.41, 0.63, 0.81, and bare surface with $L_z \sim 1$ nm; a) as a function of the relative pressure, $\langle p_g \rangle / p_o$ , at $\langle T \rangle = 86.8$ K; b) as a function of the temperature, $\langle T \rangle = 80$ to 140 K in $\langle p_g \rangle = 1.66$ atm. The insets correspond to the nanogaps with bare surfaces and one surface with nanoposts. (B) represents the bare surface. Error bars are too small to be observed. .... 73
4.5.	Variations of Ar number density, $n_f$ , for nanogaps with bare surfaces and one surface having nanoposts ( $l_p^* = 0.5$ and $l_z^* = 0.81$ ) at gas-solid interactions, $\varepsilon^* = 0.5, 1.0$ , and 2.0; a) as a function of the relative pressure, $\langle p_g \rangle / p_o$ , at $\langle T \rangle = 90$ K; b) as a function of the temperature, $\langle T \rangle = 70$ to 140 K in $\langle p_g \rangle = 1.66$ atm. The insets correspond to the nanogaps with bare surfaces and one surface with nanoposts. (S) represents the one surface having nanoposts and (B) represents the bare surface. Error bars are too small to be observed.. 75
4.6.	Predicted Ar number density, $n_f$ , in nanogaps with bare surfaces and one surface having nanoposts ( $l_p^* = 0.5$ and $l_z^* = 0.63$ ); a) as a function of the relative pressure, $\langle p_g \rangle / p_o$ , at $\langle T \rangle = 86.8$ K; b) as a function of the temperature, $\langle T \rangle = 70$ to 140 K in $\langle p_g \rangle = 1.66$ atm. The insets correspond to the nanogaps with bare surfaces and one surface with nanoposts. (S) represents the nanogap with nanoposts on one surface, and (B) represents the bare surface. Error bars are too small to be observed. .... 76
4.7.	Hysteresis in nanogaps with bare surfaces and one surface with nanoposts ( $l_p^* = 0.5$ and $l_z^* = 0.63$ ); a) as a function of the relative pressure, $\langle p_g \rangle / p_o$ , at $\langle T \rangle = 86.8$ K; b) as a function of the temperature, $\langle T \rangle = 70$ to 140 K at $\langle p_g \rangle = 1.66$ atm. The insets for the nanogaps with bare surfaces and one surface with nanoposts are also shown. (S) represents the one surface with nanoposts, and (B) represents the bare surface. Error bars are too small to be observed. .... 79

LIST OF FIGURES (continued)

Figure	Page
5.1. Schematic of capillary-controlled thermal diode using Ar-filled Pt-based heterogeneous nanogap (a) $q_+ \gg 0$ for $T_1 > T_2$ due to the high thermal conductivity of liquid-like (capillary) state, and (b) $q_- \sim 0$ for $T_1 < T_2$ due to the low thermal conductivity of gas (adsorption) state. The surface temperatures, $T_1$ and $T_2$ , heat fluxes, $q_+$ , and $q_-$ , dimensionless fluid-solid interactions, $\varepsilon_1^*$ and $\varepsilon_2^*$ , nanogap and nanopillar size parameters, $L_z$ , $l_p$ , $l_x$ , $l_z$ , and Ar particles are also shown. ....	84
5.2. Variation of (a) heat flux through the nanogap as a function of the upper surface temperature, $T_2$ , and (b) the degree of thermal diode, $R$ , as a function of absolute surface temperature difference, $ \Delta T $ , through the nanogap with $L_z = 5$ nm and $l_z^* = 0$ (bare surfaces), 0.23, 0.41, and 0.63. “B”, “E”, and “F” represent bare surface, emptying, and filling curves, respectively. Insets correspond to heat flux by Ar particles in positive (capillary state) and negative (gaseous state) directions through the nanogap. Error bars are too small to be observed. ....	89
5.3. Comparison of (a) heat flux through the nanogap as a function of the upper surface temperature, $T_2$ , and (b) the degree of thermal diode, $R$ , as a function of absolute surface temperature difference, $ \Delta T $ , through the nanogaps with different nanogap size, $L_z = 5$ and 10 nm, for $l_z^* = 0$ (bare surfaces) and 0.63. “B”, “E”, and “F” represent bare surface, emptying, and filling, respectively. Insets correspond to heat transfer by Ar particles in positive (capillary state) and negative (gaseous state) directions through the nanogap. Error bars are too small to be observed. ....	91
5.4. Variation of (a) heat flux through the nanogap as a function of the upper surface temperature, $T_2$ , and (b) the degree of thermal diode, $R$ , as a function of absolute surface temperature difference, $ \Delta T $ , through the nanogaps with $L_z = 5$ nm and $l_z^* = 0$ (bare surfaces), where the solid-fluid interaction, $\varepsilon^*$ , on each surface may be different as indicated in the inset table. “E” and “F” represent emptying and filling, respectively. Insets correspond to heat transfer by Ar particles in positive (capillary state) and negative (adsorption state) directions through the nanogap. Error bars are too small to be observed. ....	93
5.5. Variation of (a) heat flux through the nanogap as a function of the upper surface temperature, $T_2$ , and (b) the degree of thermal diode, $R$ , as a function of absolute surface temperature difference, $ \Delta T $ , through the nanogaps with $L_z = 5$ nm and $l_z^* = 0.63$ , where the solid-fluid interaction, $\varepsilon^*$ , on each surface may be different as indicated in the inset table. “E” and “F” represent emptying and filling, respectively. Insets correspond to heat transfer by Ar particles in positive (capillary state) and negative (gaseous state) directions through the nanogap. Error bars are too small to be observed. ....	95

LIST OF FIGURES (continued)

Figure	Page
6.1.	Schematic drawing of adsorption-capillary-controlled thermal switch at given pressure and temperature. (a) Nanoposts are located outside the nanogap, aiming at delaying the capillary transition (gas state only) for switch “off” mode. (b) A snapshot of the intermettant stage between switch “on” and “off” under given gas pressure. (c) Nanoposts are mechanically moved into the nanogap to facilitate capillary transition (condensation) at the given temperature, thereby resulting in switch “on” mode. The dimensions for the nanogap and nanoposts are also shown. .... 101
6.2.	Local temperature distributions across the Ar-filled nanogap with bare surfaces and nanoposts on one surface only, including the interfacial temperature jumps, i.e., Kapitza resistance. The insets show the schematic drawings of the simulation setups and the direction of the temperature gradient. .... 105
6.3.	Variations of heat flux, $q$ , and the degree of thermal switch, $S$ , at $T_{ave} = 93, 97, 100, 104, 105, 110,$ and $120$ K as a function of the nanopost height, $l_z^*$ . (a) Heat flux, $q$ , and (b) degree of thermal switch, $S$ , where the structured surface is the cold side, (c) heat flux, $q$ , and (d) degree of thermal switch, $S$ , where the structured surface is the hot side. Insets correspond to nanogaps having nanoposts on one surface only. Error bars are too small to be observed. .... 107
6.4.	(a) Variations of heat flux, $q$ , for $l_p^* = 0.67, 0.5,$ and $0.33$ as a function of the nanopost height, $l_z^*$ , at $T_{ave} = 100$ K. (b) Variations of the degree of thermal switch, $S$ , for $l_p^* = 0.67, 0.5,$ and $0.33$ as a function of the nanopost height, $l_z^*$ , at $T_{ave} = 100$ K. (c) Variations of heat flux, $q$ , for $l_p^* = 1, 0.67, 0.5,$ and $0.33$ as a function of the average nanogap temperature, $T_{ave}$ , at $l_z^* = 0.81$ . (d) Variations of the degree of thermal switch, $S$ , for $l_p^* = 1, 0.67, 0.5,$ and $0.33$ as a function of the average nanogap temperature, $T_{ave}$ , at $l_z^* = 0.81$ . Insets correspond to nanogaps having nanoposts on one surface only. Error bars are too small to be observed. .... 110
6.5.	(a) Variations of heat flux, $q$ , for $\varepsilon^* = 0.5, 1,$ and $2$ as a function of the dimensionless nanopost height, $l_z^*$ , at $l_p^* = 0.33$ and $T_{ave} = 100$ K. (b) Variations of the degree of thermal switch, $S$ , for $\varepsilon^* = 0.5, 1,$ and $2$ as a function of the nanopost height, $l_z^*$ , at $l_p^* = 0.33$ and $T_{ave} = 100$ K. (c) Variations of heat flux, $q$ , for $\varepsilon^* = 0.5, 1,$ and $2$ as a function of the average nanogap temperature, $T_{ave}$ , at $l_p^* = 0.33$ and $l_z^* = 0.81$ . (d) Variations of the degree of thermal switch, $S$ , for $\varepsilon^* = 0.5, 1,$ and $2$ as a function of the average nanogap temperature, $T_{ave}$ , at $l_p^* = 0.33$ and $l_z^* = 0.81$ . Insets illustrate nanogaps with bare surfaces and nanogaps having nanoposts on one surface only. Error bars are too small to be observed. .... 113
6.6.	Variations of (a) heat flux, $q$ , and (b) the degree of thermal switch, $S$ , through the nanogap for $T_c = 80$ K, $l_p^* = 0.33,$ and $l_z^* = 0.81$ as a function of the hot surface temperature, $T_h$ . Insets correspond to nanogaps with bare surfaces and nanogaps having nanoposts on one surface only. .... 118

LIST OF FIGURES (continued)

Figure	Page
7.1. A schematic of the adsorption-controlled thermal diode with nanostructured strong surface. (a) $\langle q_+ \rangle \gg 0$ for $T_1 > T_2$ , and (b) $\langle q_- \rangle \sim 0$ for $T_1 < T_2$ due to the adsorption-controlled asymmetric isotherm and thermal accommodation coefficient (TAC). The surface temperatures, $T_1$ and $T_2$ , heat fluxes, $\langle q_+ \rangle$ , and $\langle q_- \rangle$ , gas-solid interactions, $\varepsilon_{sf,1}$ and $\varepsilon_{sf,2}$ , nanogap size, $L_z$ , and the adsorbed particles are also shown. ....	125
7.2. A schematic of the adsorption-controlled thermal switch with nanoposts on the strong surface with the high temperature. (a) Large heat flux for “on” mode by the high thermal accommodation coefficients and (b) small heat flux for “off” mode by poor thermal accommodation coefficients (adsorption-free surface on the middle surface). ....	126
7.3. Schematic drawing of adsorption-capillary-controlled thermal transistor at given pressure and temperature distribution in a double-gap nanostructure with lower surface interaction at the bottom. (a) “Off” mode; Middle surface temperature, $T_b$ , is close to the top surface temperature, capillary state at the top and adsorption state at the bottom of the structure. (b) “On” mode; $T_b$ slightly decreases and Ar in the lower gap condensates as a result of capillary transition. (c) Back to “Off” mode by temporarily increasing the middle surface temperature to empty the nanogaps. ....	127
7.4. Proposed MEMS-based platform for measuring the heat flux and the degree of thermal diode, $R$ , or switch, $S$ , through a nanogap [243]. ....	129
7.5. Nanogap generated with nano-coated substrate and AFM tip for measuring the heat flux and the degree of thermal diode, $R$ , or switch, $S$ . ....	130

# CHAPTER 1

## INTRODUCTION AND LITERATURE REVIEW<sup>1</sup>

### 1.1 Introduction

The United States consumes 97.1 quadrillion Btu of energy annually (~ 776 billion gallons of gasoline) [1]; however, nearly 59% of this energy is being wasted in the form of thermal energy [2], which negatively impacts climate and the environment. Thus, it is imperative to find an innovative solution to improve the efficiency of energy transport/conversion, minimize degradation, and develop new applications using waste heat, with the goal of mitigating climate/environmental impacts. Novel thermal management systems (thermal diode and switch) are crucial to recycling waste heat energy [3-5], using building energy efficiently [6], and developing new energy-saving applications, i.e., thermal computers [7-11]. High-efficiency thermal diodes and switches are critical components to control thermal energy transport, conversion, and storage efficiency as basic building blocks aimed at developing thermal energy-saving/scavenging and thermal circuit/computing systems [8-10]. Recently, rigorous advances in theory and experimental demonstrations have been achieved using multiscale thermal transport phenomena. Especially, recent emerging micro- and nanotechnologies have led to the realization of experiments demonstrating such suggested theoretical mechanisms.

---

<sup>1</sup> Sections 1.1 to 1.4 of this chapter have been published in the following source:

- Hwang, G. and Avanesian, T., Multiscale Thermal Diode and Switch for Advanced Thermal Management Systems, in Multiscale Thermal Transport in Energy Systems, H. Y.-L. and Y. Zhang, Editors. 2016, Nova Science Publisher Inc.: New York.

Thermal diode and switch mechanisms have been explored via various nonlinear, tailored thermal transport mechanisms for desired functionalities. Extensive reviews can be found for the thermal diode [10, 12] and switch [13]; however, the former primarily focus on atomic-scale phononics, while the later mainly discuss macro-scale phononics, especially in spacecraft applications.

This chapter reviews the various multiscale nonlinear thermal transport mechanisms based on the principal energy carriers (for thermal conduction, convection, and radiation) for the thermal diode and thermal transport control mechanisms for the thermal switch. This chapter also includes an up-to-date literature survey and outlook for future research opportunities.

## **1.2 Thermal diode**

The thermal diode (or rectifier) is a system used to control the transfer of heat, preferentially in one direction. This system has drawn considerable interest, since it has the tremendous potential to open up new avenues for thermal management systems for desired functionalities [8, 9]. Considering the significant impact of electron signal control devices such as diodes, switches, and transistors on modern industry, the invention of a similar counterpart is an essential pathway to improve the efficiency of existing thermal systems for sustainable energy and the environment as well as to lead to new thermal energy-utilization/scavenging systems like the thermal circuit/computer. The thermal diode is crucial to significantly enhancing thermal energy transport, conversion, and storage in many applications, such as sustainable energy scavenging (solar-thermal, geo-thermal, thermoelectric, and various waste-heat recovery systems), heat engine, electronic cooling, automotive, aerospace, smart building, and biomedical systems. The thermal diode helps to easily access available thermal energy from heat sources and resists transferring heat when the temperature gradient is reversed.

Heat transfer occurs through a combination of temperature gradient and thermal conductivity between hot and cold junctions, i.e., Fourier's law,

$$\mathbf{q} = -k\nabla T, \quad (1.1)$$

where  $\mathbf{q}$  is the heat flux vector,  $k$  is the thermal conductivity, and  $T$  is the temperature. The thermal diode refers to nonlinear heat transfer, favorably in one direction (see Figure 1.1).

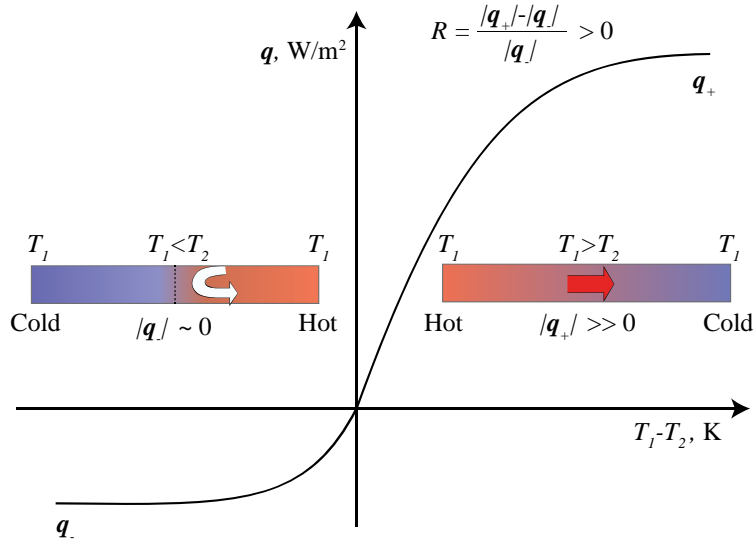


Figure 1.1. Schematic of thermal diode principle showing heat flux, where  $q_+$  is large when the temperature gradient is positive, and the reverse heat flux,  $q_-$ , is minimal when the temperature gradient is reversed. Insert shows concept of thermal diode qualitatively.

The degree of the thermal diode (or rectification) is defined as the relative heat transfer difference between the favorable (positive) and unfavorable (negative) heat flux compared to the negative heat flux, given as

$$R = \frac{|q_+| - |q_-|}{|q_-|}, \quad (1.2)$$

where  $R$  is the degree of the diode (or rectification),  $q_+$  is the positive (right) heat-flux direction, and  $q_-$  is the negative (left) heat-flux direction. In the thermal diode, the positive-direction heat

flux is greater than the negative-direction heat flux, which in turn results in  $R > 0$ , where a high  $R$  is desirable for efficient thermal rectification systems.

Thermal diodes employ nonlinear thermal transport properties across the heat source/sink via thermal conduction, radiation, and convection. In fact, an extensive review on phononics, such as a phonon-driven thermal diode, logic gate, transistor, and memory for an eventual thermal computer design, is found in the literature [10]. Here, the thermal diode mechanisms are reviewed based on the working principles as summarized below.

### **1.2.1 Nonlinear thermal conduction**

Nonlinear thermal conduction is probably the first and most popular approach to demonstrate the thermal diode. Asymmetric thermal conduction has been demonstrated through the tailored thermal transport of principal energy carriers such as phonons and electrons, and main approaches include asymmetric electrical thermal conductivity, mass distribution across heterogeneous material junctions (both solid/solid and solid/liquid interfaces), asymmetric geometries in homogeneous materials, temperature-dependent thermal conductivity, defects, and the asymmetric quantum system.

### **1.2.2 Electronic thermal conduction**

Free electrons are one of the principal thermal energy carriers, and their transport could be tailored through heterogeneous (conducting/insulating) materials. Also, electron transport could be nonlinear because it is manipulated in a quantum state. The former has been achieved via a macro-scale approach, while the latter has been demonstrated via an atomic-scale approach. Starr [14] experimentally observed the thermal diode for the first time at the interface between  $\text{Cu}_2\text{O}$  and Cu throughout a symmetric thermal conductance (mainly electrical thermal conductance) via

tailored electron transport across the interface as shown in Figure 1.2, reporting  $R_{max} = 1.67$  (maximum degree of thermal diode).

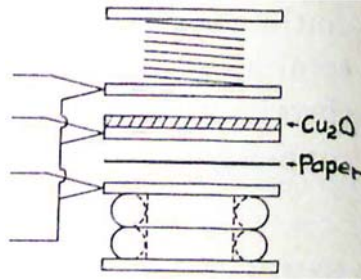


Figure 1.2. Experimental setup for the thermal diode using Cu/CuO<sub>2</sub> interface [14].

Recently, Ruokola and Ojanen [15] have examined a single-electron thermal diode using “metallic islands with a continuous spectrum” or “quantum dots with discrete states” connecting two electronic reservoirs at different temperatures using the quantum theory. Heat flow in the favorable direction is enabled by a four-step sequential tunneling cycle, while in the unfavorable direction, this process is suppressed due to Coulomb blockade effects. In order to achieve  $R \sim 10$ , a  $T_H/T_C$  of 3 or greater is required. In addition, this model should be used at temperatures near 1 K. For a realistic set up,  $T_C = 100$  mK and  $T_H = 250$  mK are proposed. Ren and Zhu [16] have shown that Kapiza resistance across a topological insulator/ superconductor junction is able to provide the thermal diode effect,  $R \sim 1$  at  $T = 70$  K. Operating temperatures lower or higher than  $T = 70$  K may result in lower degrees of rectification,  $R$ . Both  $d$ - and  $s$ -wave superconductors can be used for this setup. The Kapiza resistance here results from the different temperature responses of the topological insulator and the superconductor. Martínez-Pérez and Giazotto [17] have examined a theoretical approach to design the thermal diode using the Josephson tunneling junction. This junction potentially could be designed like an electronic transistor such as an insulating barrier sandwiched by two different superconducting electrodes. The key approach is to employ the temperature-dependent superconducting density of state (DOS), although this requires

a very large temperature gradient across the junction for the thermal diode. Predicted results have shown that the thermal diode allows for  $R_{max} \sim 8$ .

### **1.2.3 Phononic thermal conduction**

#### **1.2.3.1 Heterogeneous material junctions: solid/solid**

Segal and Nitzan [18] have shown that the manipulation of spin-boson nano-junctions result in the thermal diode effect. This is caused by a combination of the system's inherent anharmonicity and its structural asymmetry, and it is studied in a simple anharmonic system, i.e., a spin-boson nano-junction (N-atom chain). It employs two modeling approaches: a linear separable model and a nonseparable model (analytical solutions), depending on the coupling between the system and the heat bath. The first model shows that asymmetry is induced by considering different boson creation and annihilation operators for the phonon modes of the harmonic bath, resulting in  $R \sim 0.1$ . In the second model, asymmetry stems from the nonseparable system-bath coupling on hot and cold sides, causing  $R \sim 0.5$ . The sink and source temperatures here are  $T = 300$  K and 400 K, respectively. Hu et al. [19] studied the feasibility of the thermal diode caused by the asymmetric heat transfer stemming from the asymmetric phonon-phonon coupling of the atomic chain with the thermal bath, and elaborated on this using a two-segment Frenkel-Kontorova (FK) model. Considering an FK chain including two segments each containing half of the system size,  $N/2$  particles, connected by a harmonic spring, they have reached degrees of rectification as high as 1.5. However, a main technical challenge for this experimental demonstration is that the thermal diode effect is strongly dependent on the number of particles and the spring constant, which may not be straightforward to control in the experimental setup. Roberts and Walker [5, 20] have demonstrated the asymmetric thermal transport at the Ar/Kr interface using molecular dynamics simulation (MDS) as shown in Figure 1.3. They observed that the phonon scattering at the

structured, heterogeneous interface results in a thermal diode showing  $R_{max} \sim 0.06$  at  $T \sim 50$  K and device length scale of  $\sim 50$  nm.

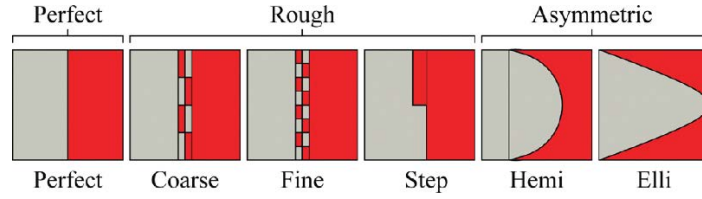


Figure 1.3. Various interfacial structures between Ar/Kr materials for thermal diode using molecular dynamics simulations [5].

Chen et al. [21] have examined the thermal transport across the graphene/hexagonal-boron nitride (h-BN) nanoribbon interface using nonequilibrium molecular dynamics simulation (NEMD) and found that the favorable heat flux direction is from the h-BN to graphene, resulting in  $R_{max} \sim 1.45$ . In this heterogeneous structure, the temperature drop across the interface is related to the Kapitza interfacial resistance, which is asymmetric due to the different phonon scatterings from different directions. The different interfacial structure leads to the different level of  $R$ , i.e., the armchair interface provides a higher  $R$  than the zigzag interface, due to the beneficial effect of the delocalized modes there. They have also found that the large  $\Delta T$ , low temperature, short length, and small number of interfaces allow for the large  $R$ .

Carlomagno et al. [22] have designed a thermal diode using a composition-graded system with theoretical materials, where the composition changes along the length of the system, considering the size effect, i.e., from a macro- to nanoscale system. For a macroscale system, a quadratic composition profile along the length of the system allows for  $R \sim 0.3$ , while a minimal  $R$  is observed for the linear concentration distribution. As the system size becomes small, i.e., from micro- to nanoscale ( $L = 10^{-6}$  and  $10^{-9}$  m),  $R$  becomes independent of the composition distribution, which allows for 1.3 and 1.25, respectively.

### 1.2.3.2 Heterogeneous junctions: solid/liquid

Hu et al. [23] have theoretically analyzed the potential thermal diode design using water in self-assembled monolayer (SAM,  $(\text{CH}_2)_n\text{OH}$ ) interface chemically bonded to a silica surface using molecular dynamics simulation. They found that the temperature-dependent, nonlinear phonon scattering near the interface between the water and solid interface results in the thermal diode effect, showing that  $R_{max} \sim 0.54$  can be achieved. This thermal diode effect increases with increasing heat flux and temperature. Murad and Puri [24] have achieved the thermal diode using the water-filled heterogeneous water-wetting gap. The working principle here is to create a density gradient across the gap to manipulate the water-wetting-driven temperature-dependent heat transfer, and this can be achieved by manipulating charges of the water molecules near Si solid walls to mimic a polar surface. Predicted results show that the thermal diode effect is maximized when the cold side becomes highly hydrophilic, and a further diode effect could be achieved using an external force applied to the flow. Yuan and Xin-Gang [25] have demonstrated a nano thermal diode using temperature-dependent phonon scattering at the argon/face-centered cubic (Ar/FCC) solid interface. With variations in the potential well depth (surface energy) and FCC solid mass NEMD, they determined the asymmetric thermal conductance across the interface and observed the maximum rectification to be  $R_{max} = 1.14$  at an average temperature of 120 K.

### 1.2.3.3 Homogeneous junctions: asymmetric geometry

Asymmetric geometry or energy transport mechanism control (atomic-structural defect, mass graded, diameter, nonlinear chain, temperature-dependent phase-change) within the homogeneous materials has been explored to demonstrate the thermal diode, due to asymmetric phonon scattering and transport from different directions of the temperature gradient. Casati [9], Li et al. [26], and Terraneo et al. [27] have simulated a nonlinear atomic chain (artificial system) and

calculated a difference in conduction between the two directions, finding that the maximum thermal diode could be achieved at  $R_{max} \sim 100$ . Chang et al. [8] have demonstrated experimentally a thermal diode using carbon nanotubes (CNTs) and boron nitride nanotubes (BNNTs) with a tilted junction as a first measurement in the nanostructure for a thermal diode. They used CNTs and BNNTs, due to their high thermal conductivity dominated by phonons [28, 29], and a nonuniform axial mass distribution has been added on the outer wall of the nanotubes by depositing amorphous  $C_9H_{16}Pt$  for a diameter of 30 to 40 nm for BNNTs and 10 to 33 nm for CNTs with a length of 10  $\mu m$ . They have found that the thermal conductance is higher when the heat transfer direction is from the high-mass to low-mass region for the thermal diode,  $R_{max} \sim 0.02$  (CNT)  $R_{max} \sim 0.07$  at ambient temperature, and they have concluded that the stronger ionic nature results in higher nonlinear thermal transport in BNNTs compared to CNTs. Tian et al. [30] have employed the tapered reduced graphene oxide (rGO), experimentally showing  $R_{max} \sim 0.25$  using nonlinear thermal conduction via asymmetric geometries. Hu et al. [31] have demonstrated the thermal diode through tapered graphene nanoribbons (GNRs) and have found that the magnitude of  $R$  depends on the chirality of the bottom base and its vertex angle. Although the thermal conductivity of zigzag GNR is 20–50% higher than the armchair GNR, a higher magnitude of  $R_{max} \sim 1.2$  (at 180 K) is predicted for the armchair-based triangular GNR. The different phonon scatterings is the main reason for having different values of  $R$ , and the positive direction is from the wider to narrower edge of the triangle. The largest thermal rectification is found in the triangular GNR with armchair bottom edge and vertex angle of  $30^\circ$ . Structural defects such as circular vacancies and edge roughness decrease thermal conductivity as well as the degree of rectification. Trapezoid-shaped GNRs also provide the thermal diode effect but to a smaller degree than triangular-shaped

GNRs. Ni et al. [32] have designed heterogeneous CNTs, so-called partially-unzipped carbon nanotubes (PUCNTs) using MDS for the thermal diode as shown in Figure 1.4.

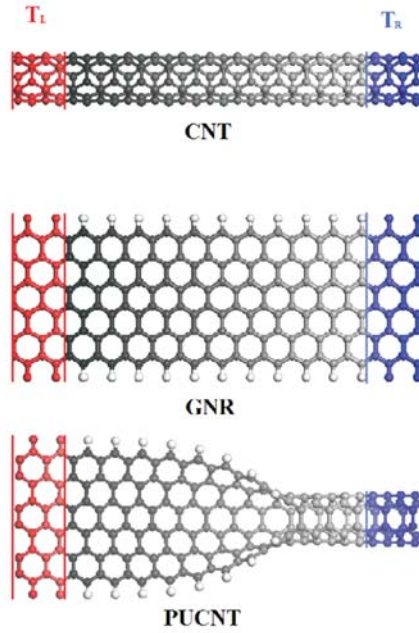


Figure 1.4. Asymmetric nanostructure for the thermal diode using partially-unzipped carbon nanotube (PUCNTs) [32].

They found that the nonlinear thermal conductivity is caused by the higher localization modes on the boundary induced by junction scattering. The degree of thermal rectification is higher for the armchair (3,3) PUCNTs compared with zigzag ones (5,0) and increases with temperature. The degree of thermal rectification is related to the relative length of the preserved CNT to the entire PUCNT length,  $r$ , showing that it increases with decreasing  $r$ . An increasing length of the entire structure with the constant  $r$  leads to a lower  $R$  as the effect of the junction interface is intensified. Wang et al. [33] have shown that  $R_{max} \sim 0.7$  (at  $\langle T \rangle = 200$  K) through defect engineering in the graphene nanoribbon.

Alaghemandi et al. [34] predicted  $R_{max} \sim 0.42$  in the mass-graded, single-wall carbon nanotube (SWCNT), and Pal and Puri [35] have shown the thermal diode effect at the functionalized

SWCNT with polyacetylene (PA) in only one end using MDS, which resulted in  $R_{max} = 2.04$  at  $T = 30 - 40$  K. The predicted results have shown that the thermal diode effects have been generated when the PA is adjacent to the hot side, i.e., phonon transverse scattering between PA and CNT molecules, and also the coupling of the phonon scattering with their longitudinal transport is different than the case when the PA structure is closer to the cold side. This is caused by the fact that phonon scattering is temperature dependent, in other words, the spectral mismatch is greater during the negative direction because of increased phonon-phonon scattering. Because the longer distance of PA functionalization from the center of the CNT increases asymmetry, the degree of rectification also increases. Increasing the length and diameter of the CNT increases thermal conductivity in a negative direction and thus decreases  $R$ . The proposed PA functionalization could be fabricated by existing nanotechnologies based on previous work [36-38]. Several groups have successfully predicted the thermal diode effect using a diameter-mismatched nanotube [39] using asymmetric nanostructures by a nanocone [40] as well as a nanoribbon ( $R_{max} \sim 3.5$ ) [41]. Jiang et al. [42] have studied  $R_{max} \sim 1.2$  for Möbius graphene strips (MGSs) with zigzag edges, as a function of the position of the heat baths (within the MGS) using NEMD. In the case where heat baths are located symmetrically (at  $\theta = 0$  and  $\theta = \pi$ ), they found  $R \sim 0.35$ , which does not change dramatically with the change in temperature and strip length. For MGSs with armchair edges, completely different magnitudes of  $R$  are obtained ( $\sim 0.6$  for the case with symmetrically located heat baths). Zhang and Zhang [43] have examined the thermal diode in graphene Y junctions, with the favorable direction being from the branches to the stem using molecular dynamics simulation. Layer-layer interaction increases  $R$  from  $\sim 0.4$  to  $\sim 0.65$  for a double-layer structure. The match/mismatch of the vibration Density of State (vDOS) spectra between the two ends results in thermal rectification. The authors claim that the graphene Y junction gives a higher  $R$  compared

to the carbon nanotube Y junction. Lee et al. [44] have observed thermal rectification in a 3D single crystalline diamond nanostructure using molecular dynamics simulation. The selected asymmetric nanostructure is a pyramid with a flat tip, and  $R$  increases ( $R_{max} \sim 1.5$ ) because there is a higher temperature gradient and narrower edge of the flat pyramid (higher degree of asymmetry). At the large temperature gradient, the degree of rectification increases with the degree of mismatch of the vDOS on the narrow side. They considered different heat bath-diode interface lengths and concluded that the  $R$  can be maximized when the contact area becomes as wide as the flat pyramid. Tian et al. [30] achieved  $R_{max} \sim 0.21$ – $0.28$  using a reduced graphene oxide triangle and rectangle. Wang et al. [45] have also observed a possible thermal diode mechanism from the lateral phonon confinement in the graphene nanoribbon, with  $R_{max} = 0.4$  at 100/300 K. This principle utilizes the asymmetric phonon scattering from the narrow-to-wide cross section compared to the wide-to-narrow cross section.

Zhu et al. [46] have experimentally studied a thermal diode using a tapered vanadium dioxide beam (asymmetric geometry). Platinum coils were used both as heaters and resistive thermometers for the test at  $T = 250$  and  $340$  K. The temperature range was chosen to maximize the electron-phonon scattering for the metal-insulator interface for  $\text{VO}_2$ , resulting in  $R_{max} \sim 0.28$ . Cartoixà et al. [47] have observed  $R_{max} \sim 0.5$  using silicon nanowires (SiNWs) with a significant change in diameter at the junction using NEMD. The thermal diode effect is caused by the asymmetric phonon scattering near the interface. A thermal diode effect requires a large temperature gradient, at least  $0.93$  K/nm or greater, under a noise-free heat current condition. Using NEMD, Liu et al. [48] have examined the effect of the standing wave on the thermal diode in the asymmetric InAs and Si nanowires. They found that the asymmetric heat transfer originates from the tailored phonon vibrational density of state due to phonon scattering from the asymmetric geometries, which occurs

when there is a coincidence of the natural frequencies along the two directions. This is the primary reason why  $R$  in graded InAs nanowires is higher than in Si nanowires (1.63 vs. 0.25). Pan et al. [49] have analyzed the unsteady heat flux (heat pulse) phenomenon in graphene Y junctions, which occurs as the result of different longitudinal vibrational modes due to the heat pulse in positive and negative directions. More interestingly, the favorable direction is different for two different Y junctions, namely (A8-A4-A4,  $120^\circ$ ) and (A8-Z5-Z5,  $60^\circ$ ), being armchair- and zigzag-edged graphene nanoribbons, respectively. Higher rectification,  $R \sim 1$ , is achieved by the first Y junction, with the positive direction being from the stem to the branches.

#### **1.2.3.4 Heterogeneous junctions: quantum system**

The thermal diode has been observed in quantum systems (atomic-scale). Eckmann and Mejía-Monasterio [50] have shown the thermal diode effect at the heterogeneous junction (nonlinear billiard-like collision). The billiard-like system with interacting particles induces a local dynamic response of the billiard to an external thermodynamic gradient, which leads to a steady-state, asymmetric billiard in terms of particle and energy-reflection coefficients. The thermal diode phenomena between two electrical conductors have been found through a nonlinear electron-gas-dispersion relation transport [51, 52]; a quantum dot structure [4, 53, 54], a nonlinear quantum circuit [55], and a quantum system [56]. Although these previous studies have shown the interesting scientific phenomena and approaches, the thermal diode effect in quantum systems remains as theory, without experimental demonstrations so far.

#### **1.2.3.5 Homogeneous junction: asymmetric mass distribution**

Another way to design the thermal diode is to utilize nonuniform atom mass distribution from the heat source to the heat sink. Alaghemandi et al. [34] have employed the mass-graded nanotube and calculated the degree of the thermal diode using the reverse nonequilibrium molecular

dynamics simulation (RNEMD). They have shown that the favorable heat transfer direction is from light atoms to heavy atoms, and the diode effect increases with increasing length, diameter, or mass gradient of the nanotube, with  $R_{max} \sim 0.12$  at  $T = 200$  K. The reason why heat is transferred from lighter to heavier atoms is that the lighter atoms transfer energy more efficiently from the transverse to longitudinal vibration. The larger tube diameter increases the number of transverse modes, which in turn enhances the heat transfer. The increasing nanotube length with increased number of heavier atoms leads to the enhanced anharmonic character of the lattice, and the lighter atoms carry higher thermal energy, which leads to a higher degree of thermal rectification. The increasing temperature lowers the degree of rectification. Balasubramanian et al. [57] have demonstrated the thermal diode effect using thermal conductivity reduction due to mass disorder in nanomaterials (carbon nanotubes) from the isotope, i.e., C12–C14, which in turn results in a relatively small  $R$ .

#### **1.2.3.6 Other approaches: assisted by external controller**

The nonlinear phonon transport (scattering and/or coupling) can be manipulated by external forces such as an external magnetic field or acoustic noise in the thermal diode design. Casati et al. [58] have demonstrated the asymmetric heat transport in chaotic billiard chains, when half of the chain particles are under a strong, perpendicular, uniform magnetic field, or the entire chain of particles is under a strong magnetic field gradient along the chain. Under the magnetic field, the energy carriers are charged particles moving freely inside a closed two-dimensional billiard region, and the nonlinear thermal transport stems from the difference between the size of the kinetic energy profile gap for the favorable and unfavorable directions. The main technical challenge for this system is that the thermal diode requires a high temperature, which disappears when it reaches a thermodynamic limit.

Murad and Puri [59] have utilized water (density graded) in a silicon nanogap and calculated the thermal diode. They have shown the maximum thermal diode to be  $R_{max} \sim 1$ . Here, water is distributed in the reservoir using an external force, usually an order of magnitude smaller than the intermolecular forces of each water molecule, in order to create a density gradient. In experimental work, this force can be applied by employing electric or magnetic fields. This density gradient provides an asymmetric axial thermal conductance, i.e., thermal diode in a way that the positive direction is the direction of decreasing mass density.

Bagchi [60] has predicted the thermal diode effect in a two segment classical Heisenberg spin chain with the spatial asymmetry under an external magnetic field. The nonlinear thermal transport is found by the dissimilar spin-spin coupling strengths, under the temperature difference between the two baths, interaction strength, segment size, and the magnitude of the magnetic field. The key to the diode effect is the interface (Kapiza) resistance, where the degree of rectification,  $R$ , increases as the temperature decreases, the system size becomes smaller, and the strength of the magnetic field is higher, i.e., the ballistic regime. Guimarães et al. [61] have designed a thermal diode using classical harmonic, Frenkel-Kontorova, and Fermi-Pasta-Ulam chains under an energy-conserving noise through self-consistent reservoirs for random particle velocity manipulation. The primary focus of this study was to maintain the degree of thermal rectification assisted by the energy-conserving noise, even though it is close to the thermodynamic limit. Note that the previous study shows that the thermal diode effect disappears near the thermodynamics limit [58]. Using a considerably large temperature gradient, the authors have shown that with increasing randomness of the particle velocity profiles,  $R$  reaches the asymptotic value, 0.73, independent of chain size. They have concluded that the highly chaotic behavior with the energy-conserving noise results in an ergodic system, as studied by Landi and de Oliveira [62].

Suwunnarat et al. [63] have employed the asymmetric heat transfer rate induced by the Coriolis force from the rotating platform in the harmonic chain (lattice) to design a controllable thermal diode. The angular velocity results in changing the heat flux direction, which in turn leads to a controllable thermal diode. Three co-rotating heat baths are coupled with the chain, each of which are connected to particular atoms in the lattice, and two of these reservoirs behave as the heat source and heat sink, and the third one is asymmetrically coupled with the setup to block any spatial symmetry. This system leads to  $R_{max} \sim 0.006$ , without a classical limit for the thermal diode, i.e., high operating average temperatures. Tso and Chao [64] have explored the fact that the degree of rectification,  $R_{max} \sim 90$ , can be achieved in a passive shape memory alloy (SMA)-based macroscopic thermal diode (dimensions about 10 cm). SMAs assist in making a large difference between the effective thermal conductivity in favorable and unfavorable directions (281 W/m-K and 3 W/m-K, respectively). The main challenge here is that this design is not applicable when the inlet temperature is lower than the SMA activating temperature.

#### **1.2.4 Nonlinear thermal convection**

To the best of the authors' knowledge, the experimentally demonstrated degree of rectification using asymmetric thermal convection is the largest among other approaches. For the first time, Globe and Dropkin have studied a gravity-driven asymmetric heat transfer in a confined liquid with two solid plates using nonlinear thermal convection [12, 65]. Their key approach is to employ the favorable flow direction by gravity. The typical setup is two liquid-filled solid plates under the temperature gradient, and when the temperature gradient direction is against the gravity (upward heat transfer), it favors the heat transfer because the buoyancy assists the natural convection, while when the temperature gradient is reversed, the heat transfer occurs only via thermal conduction

through the liquid (no significant natural convection). This asymmetry allows for a thermal diode with  $R_{max} \sim 9$ .

To further improve the low  $R$ , Groll et al. [66, 67] and Alario [66, 67] have employed capillary-assisted, nonlinear thermal convection, i.e., heat pipes, where heat transfers from the evaporator to the condenser via vapor, while the liquid returns to the evaporator via the capillary pressure gradient. Typically, the evaporator is designed for the smaller liquid pressure (large capillary pressure), in order to enhance the liquid supply from the condenser (characteristic geometry  $\sim 10\text{-}100\ \mu\text{m}$ ), whereas the condenser has a relatively large capillary meniscus radius (characteristic geometry  $\sim 1\ \text{mm}$ ). When the temperature gradient is from the evaporator, the heat transfer is favorable, while the reverse temperature gradient leads to a nearly negligibly small heat transfer, which in turn results in the thermal diode,  $R_{max} \sim 200$  [66] and  $R_{max} \sim 1,000$  [67].

Boreyko et al. [68] and Hirayanagi et al. [69] have designed a thermal diode using heterogeneous water wettings, i.e., hydrophilic and hydrophobic surfaces as shown in Figure 1.5.

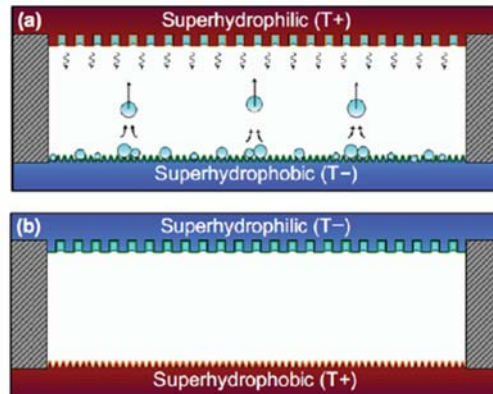


Figure 1.5 A schematic drawing of water-filled heterogeneous wetting surfaces for thermal diode,  $R_{max} \sim 100$  [68].

Here, the heat transfer favors when the temperature gradient direction is from the hydrophilic to hydrophobic surfaces due to the favorable water supply to the heat source (hydrophilic surface),

whereas the reverse temperature gradient limits the liquid supply (i.e., hydrophobic surface). These designs lead to  $R_{max} \sim 100$  and  $R_{max} \sim 0.46$ , respectively.

### 1.2.5 Nonlinear thermal radiation

The thermal diode has also been observed using temperature-dependent radiative heat transfer (photon) in tailored micro/nanostructures. In general, the operating temperature is relatively higher than other mechanisms. Otey et al. [70] demonstrated photon-mediated thermal diodes through temperature-dependent optical resonances for  $R_{max} = 0.41$  at  $T_c = 300$  and  $T_h = 600$  K in the nanogap of 100 nm using SiC as base material. The key approach here is that the surface phonon polariton frequencies of SiC-3C and SiC-6H become nonlinear, where the spectral emissivities are different from the temperature gradient. For favorable heat flux direction, the spectral emissivities of the two bodies become similar, whereas the reverse temperature gradient direction leads to different spectral emissivities, thus causing the unfavorable heat flux direction.

Similarly, the thermal diode has been improved to  $R_{max} = 0.7$  using dielectric coating [71]. Basu and Francoeur [72] have examined the thermal diode effect between a film and a half-space of doped silicon with different doping concentrations, achieving a maximum thermal rectification of 0.51 with a 10 nm vacuum gap at temperatures of 350 K. Ben-Abdallah and Biehs [73] have predicted the phase-change-driven radiative diode,  $R_{max} = 0.9$ . This phase-change stems from a sudden change in optical properties of insulator metal transition (IMT) materials like VO<sub>2</sub> due to a small change in temperature around the critical temperature. They have considered a system composed of VO<sub>2</sub> on one side and SiO<sub>2</sub> on the other side, with a vacuum gap of a certain thickness considerably larger than their thermal wavelengths in between (far-field regime). In the favorable direction,  $T_{VO_2}$  is greater than its critical temperature (340 K) and is in a metallic phase. For the unfavorable direction, the VO<sub>2</sub> temperature is lower than 340 K and is in a crystalline phase.

Results show  $R \sim 0.7$ , which could be enhanced to  $R_{max} \sim 0.94$  by increasing the temperature gradient to about 200 K.

Yang et al. [74] have designed a nanogap using  $\text{SiO}_2$  and  $\text{VO}_2$  filled with a vacuum with a 10–1,000 nm gap size, and this phase change of  $\text{VO}_2$  resulted in  $R_{max} \sim 3.2$ . Zhu et al. [75] have calculated  $R_{max} \sim 13$  in bi-modal-size nanoparticles using tuned optimal resonance. Wang and Zhang [76] have observed the thermal diode between intrinsic silicon and various materials including doped  $\text{Si}/\text{SiO}_2/\text{Au}$ , predicting  $R_{max} = 9.9$ . at 300/1000 K with a 5 nm gap size. The thermal diode could also be achieved in asymmetric thermal radiation at the blackbody sandwiched by two surfaces having different emissivities, resulting in  $R_{max} \sim 0.21$  at surfaces temperatures of 1,000/500 K [12, 77].

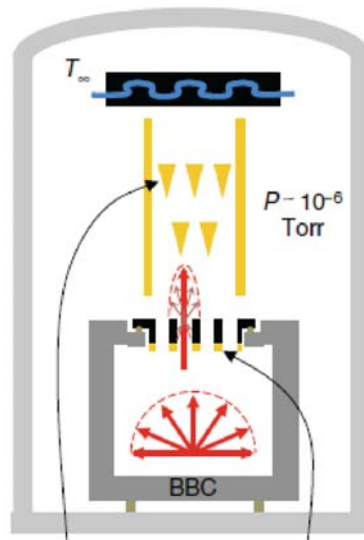


Figure 1.6 A schematic drawing of asymmetric photon scattering through pyramid collimator [11].

Chen et al. [11] have experimentally achieved a thermal diode of  $\sim 0.1$ , based on the asymmetric scattering of ballistic energy carriers (photon-based diode) by means of pyramidal reflectors and an inelastic collimator, as shown in Figure 1.6. The geometrical asymmetry stems from a taper of pyramidal mirrors, where photons of near-normal incidence angles are more easily

transmitted from the peak of the pyramids, and the photons with incidence angles near zero enter the test section better from the base of the pyramid. The required nonlinearity is caused by using an inelastic thermal collimator distorting the angle-dependent emission. Experimental results show that no diode effect is observed without the collimator, and by using an inelastic collimator with a pore aspect ratio of  $H/D = 1$ , a thermal diode of  $R \sim 0.1$  is achieved.

Increasing the aspect ratio or decreasing the hot-side temperature decreases the magnitude of the diode effect. Mascarenhas et al. [78] have theoretically examined 2D spatially nonreciprocal devices, which allow unidirectional propagation of a single or a few energy quanta at a fixed signal frequency and amplitude. This is based on the fact that a transmitted intensity at a fixed-incident amplitude and at the same frequency should be significantly different in the two opposite propagation directions. The system includes a nonlinear-linear junction. Because the energy transport is towards the linear section, the diode efficiency is higher, whereas when the junction receives a quantum state instead of a coherent field as input, the large diode effect for the linear-to-nonlinear transport is obtained when resonance occurs. The diode effect is also observed on the opposite side when detuning is compensated by nonlinearity. The proposed thermal diode design could be potentially demonstrated using the experimental setup having superconducting microwave circuits and semiconducting optical circuits. Keidar et al. [79] have designed a thermal diode based on a difference in electron emission current densities from the electrodes with different work functions and surface temperatures using a vacuum between the electrodes. They have found that this approach leads to  $R_{max} \sim 9$ ; however, this design requires very high temperature  $> 1400$  K and a large temperature gradient as high as 100 K across a small gap (order of 1  $\mu\text{m}$ ) for the thermal radiation wavelength manipulation.

Mascarenhas et al. [80] have shown that the thermal diode could be potentially achieved with a manipulated radiation field by using a quantum approach for classical driving under external noise and a single-photon pulsed excitation. This system has a one-dimensional channel with a pair of two-level quantum systems and different ground-to-excited-state transition resonances, under a classical continuous wave and a quantum photon pulse. Results show that the thermal diode enables the blocking of noise through the positive direction, while still transmitting through the negative direction. Schaller et al. [81] have observed that the stationary heat current from the hot dissipative reservoir to the cold pure dephasing reservoir is much larger compared to the one in the reverse direction. This can be achieved by using an ensemble of  $N$ -identical two-level systems asymmetrically coupled with two different thermal reservoirs—dissipative (transversal) coupling with one and pure dephasing (longitudinal) coupling with the other—under a nonequilibrium state. Results show a considerable increase in the thermal diode with quadratic scaling of the current due to supertransmittance.

In conclusion, the maximum degree of rectification,  $R_{max}$ , for various theoretical/experimental approaches are summarized as a function of the operating temperature as shown in Figure 1.7. The number of studies using these experimental approaches is smaller than those using the theoretical approach. The convective, nonlinear (macro- to micro-scale) thermal transport leads to the larger  $R_{max}$ , compared to the conduction and radiation mechanisms. Also, note that the thermal diode using the radiation requires relatively higher operating temperatures compared to the convection and conduction. The current, multiscale theoretical approach primarily supports only the limited degree of thermal rectification  $R_{max} < 10$ , although a few atomic-scale, quantum-mechanics-based theories have predicted  $R_{max} > 100$ . For practical implementations to the large-scale applications,

both theory/experiment need to be advanced to address the few technical challenges as given below.

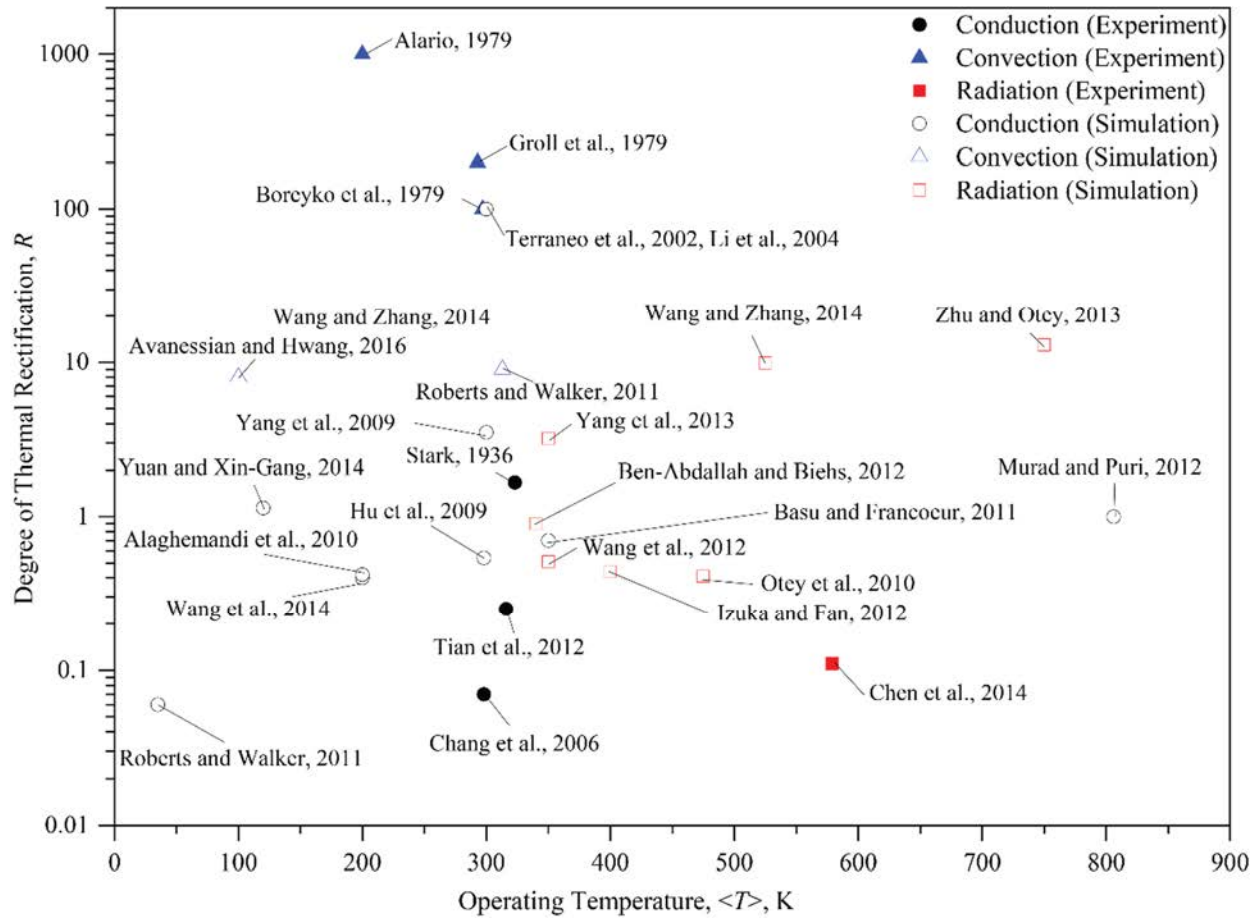


Figure 1.7. Summary of previously reported degree of thermal rectification,  $R$ , using both experimental and theoretical/computational approaches in nonlinear conduction, convection, and radiation heat transfer mechanisms. Variations of thermal diode (or rectification) with respect to operating temperature range (average temperature) and target thermal rectification (present study) are also shown.

### 1.2.6 Outlook for future research

As reviewed above, extensive efforts have been made in both fundamental theoretical working principles as well as applications to experimental demonstrations; however, implementations to the practical applications have been limited due to a few technical challenges as discussed below:

- a) Poor steady-state  $R$  and/or slow transient response

For the first time, the thermal diode has been experimentally demonstrated in a solid state,  $R_{max} \sim 1.7$  [14], but the steady-state performance still remains lower than desired, e.g., using an asymmetric carbon nanotube,  $R_{max} \sim 0.07$  [8], asymmetric graphene oxide,  $R_{max} \sim 0.25$  [30], electrochemically tuned thermal diode material,  $R_{max} \sim 0.5$  [82], and asymmetric photon transport,  $R_{max} \sim 0.11$  [11]. To improve the low  $R$ , the liquid-based system has been employed for the nonlinear convection for the thermal diode, e.g., using heat pipes,  $R_{max} \sim 200$  [66] and  $R_{max} \sim 1,000$  [67], and heterogeneous water wettings,  $R_{max} \sim 100$  [68] and  $R_{max} \sim 0.46$  [69]. However, the liquid-based systems result in a poor transient response of  $\sim 10$  min, which may significantly limit the thermal computing speed.

#### b) Expensive manufacturing and poor scalability

Thus far, numerous theoretical frameworks for efficient thermal diode mechanisms [4, 5, 9, 12, 23, 25-27, 31, 33-35, 39-41, 45, 50-57, 59, 70-77] have not been proven in experiments, perhaps due to the required very-expensive or challenging atomic-level manufacturing technologies. These mechanisms include nonlinear quantum systems [4, 50-56], which should be a long-term approach for such experiments.

#### c) Limited operation conditions

Some of the efficient radiative thermal diode mechanisms require relatively high temperatures [75, 76], and a natural convection mechanism requires gravity-favorable orientation (limited device/system installation) [12]. This may in turn result in limited impact, especially for near or subambient temperature operation applications.

### 1.3 Thermal switch

Thermal switches, also known as heat switches, are systems that enable us to control the amount of heat transfer rate, while switching roles between good thermal conductors and insulators

using active and/or passive control systems. Typically, when a thermal switch is in the “On” mode, it becomes a good thermal conductor, whereas when the switch is in the “Off” mode, it serves as a good thermal insulator. The thermal switch is a crucial component in the design of various spacecraft/automotive applications [13], power production [83], and cryogenic thermal management systems [84], in order to enhance the steady-state performance and transient response.

The thermal switch is typically installed between the heat source/sink and the target system to maintain the target system temperature, and the typical system consists of three components: heat source, heat sink, and thermal delivery component. The thermal delivery component can be operated using either an active or passive control system. The active system utilizes external power sources (typically mechanical and electrical control systems), whereas the passive control system employs a self-regulated thermal control system (generally mechanical- and/or thermal-actuator-driven switching mechanisms). The good thermal switch requires a large contrast ratio of the thermal conduction to insulation at the steady state and fast enough to switch between the “On” and “Off” modes, yet sufficiently well damped by the thermal capacitance and mechanical characteristics to avoid overshooting desired target temperatures. The degree of the thermal switch,  $S$ , is defined using the ratio of the heat transfer in its “On” mode to “Off” mode, given as

$$S = \left| \mathbf{q}_{on} \right| / \left| \mathbf{q}_{off} \right| \quad (1.3)$$

where  $\mathbf{q}_{on}$  and  $\mathbf{q}_{off}$  are the heat fluxes when they are in “On” and “Off” modes, respectively. The typical degree of the thermal switch varies from 100 to 1,000, and the transient response time is in the order of 1 s to 1 min.

This chapter provides a review of various types of thermal switches, including mechanical-movement-based and thermal-expansion in macro- to nanoscale working principles. Also, this

chapter discusses the outlook on future research directions for the efficient thermal switch and new applications, such as a thermal computer for energy-saving applications.

### **1.3.1 Micro- to macro-scale, mechanical-based thermal switch**

#### **1.3.1.1 Differential thermal expansion thermal switches**

A typical approach to thermal transport switching control is to employ physical movement for the thermal “On/Off” switch [85]. One popular way is to employ the differential thermal expansion coefficient (TEC) of two different (solid) materials in order to have control over the thermal contact at the “On/Off” interface. The TEC is typically a function of temperature, and the difference between the two materials could be different from the different operating temperatures. In general, the two different materials are placed next to each other, and at a given temperature, the materials lead to different thermal expansions, resulting in the desired physical bending/torsion for the thermal switch. This approach enables a reliable and robust design, which leads to a popular approach. However, one challenge is that the differential TEC is typically very small, i.e.,  $\sim \mu\text{m/K}$ , and for a large mechanical movement, it requires a large coefficient difference or large temperature change. Since this approach requires physical movement of the thermal switching actuator, it needs the additional physical system space, and it may not be an ideal solution for small-scale applications. The switching time is relatively fast and it usually takes on the order of 10 s. This time is typically the heating/cooling time of the differential TEC materials.

Although this approach has the aforementioned technical challenges, it has been adopted as one of the most popular options for cryogenic thermal switch design due to the reliable and relatively flexible operating temperature (especially cryogenic temperature, i.e., no freezing or phase change). A typical mechanical cryogenic thermal switch controls heat transfer through two metallic or nonmetallic materials, enabling the moving or bending for the thermal conductance

and/or insulation [85]. Vanoost et al. [85] have experimentally demonstrated an efficient cryogenic thermal switch utilizing an amplified differential thermal stress between two dissimilar materials using metal-metal contact and a flexible coupling, which shows a thermal conductance of 0.27 W/K for the “On” mode and  $5 \times 10^{-4}$  W/K for the “Off” mode, under operating temperatures between 80 and 150 K, resulting in  $S_{max} \sim 549.5$ . Wang et al. [86] have created a cryogenic thermal switch using lightweight differential thermal expansion, allowing for a thermal conductance of 0.23 W/K for the “On” mode and a thermal conductance of  $7.14 \times 10^{-4}$  W/K for the “Off” mode, resulting in  $S_{max} \sim 322$ .

### 1.3.1.2 Gas-filled microgap

A gas-filled microgap has been employed to design the thermal switch [85, 87, 88]. This approach utilizes a controllable, thermal conduction using gas as a heat carrier. During the “On” mode, the heat transfer primarily goes through gas thermal conductivity, especially at high gas pressures, i.e., dense fluid particles as a primary heat carrier, while in the “Off” mode, the heat transfer becomes negligibly small at low gas pressures, i.e., a vacuum. To operate this type of thermal switch requires a mechanical or sorption pump to control the gas pressures of the micro- or nanogaps [84, 88]. These additional systems result in extra cost, additional system design complexity, and increased system weight, which in turn leads to significant design limitations. Using He-filled micro-size gaps, at  $T = 1.7$  K, the thermal conductance of 0.1 W/K is obtained for the “On” mode (viscous regime) and  $\sim 0.06$  mW/K for the “Off” mode, by changing the gas pressure using a sorption pump [88]. At  $T = 4.2$  K, a similar thermal conductance for the “Off” mode is seen, whereas  $\sim 0.2$  W/K was observed for the “On” mode. The “On” mode conductance for both charging pressures is very similar at each temperature, which indicates that the viscous regime was indeed achieved even with 5 kPa of gas.

### **1.3.1.3 Paraffin-based (phase change material) thermal switch**

A phase-change-driven mechanical movement for a mechanical actuator leads to a reliable mechanism to design the thermal switch [85]. The paraffin-based, phase-change materials allow for a significant volume (or density) change during the freezing/melting process (upon melting, paraffin expands approximately 15%), and the volume change could provide a hydraulic force to actuate the thermal switch. The operating temperature varies depending on the melting temperature of the phase-change material, and carbon-based materials are one of the most popular approaches. The significant volume expansion during the phase change is also employed for the high-power-mechanical “actuators,” which have been a crucial component to controlling the motions of the hinges, latches, launch-caging mechanism, and other components, especially in spacecraft. In other words, the phase-change-driven volume expansion “powers” the mechanical actuators.

For the thermal switch operation, the volume expansion favorably moves the thermally conducting material to physically bridge the two heat baths in order to turn on the switch, and when it is released, it serves as an “Off” mode as it disconnects the two heat baths. Although this approach is very efficient and straightforward, there are a few technical challenges. When the temperature approaches close to the phase-change temperature, the phase-change material either partially freezes or melts, which results in releasing a significant amount of heat from the latent heat (or absorbing significant heat as a latent heat) without changing the temperature. Near the phase-change temperature, significant heat energy is needed to control the desired temperatures due to the relatively large latent heat, which causes a low transient response on the order of one minute. A key component of this technology is an engineered phase-change material for the desired functionalities, including melting/freezing temperature, specific heat, density, and

chemical/mechanical stabilities. This can be tailored using composite technology and nanotechnology such as molecular-level chemical engineering in paraffin.

#### **1.3.1.4 Heat pipe**

A heat pipe has been known to be a thermal super conductor with a minimal temperature gradient between the heat source and the sink. It utilizes the phase-change-based heat transfer mechanism from the evaporator and condenser, and the condensed working fluid returns to the evaporator to continue to deliver heat. However, under a certain condition, the heat transfer can be minimized by shutting the fluid motion off, i.e., “On/Off” mode, and no fluid motion will result in the thermal switch.

Overall, there are two types of heat pipes—traditional and loop—depending on the fluid motion control. The traditional heat pipe controls the fluid using the capillary pressure gradient between the condenser and the evaporator (passive fluid motion control), and the loop heat pipe controls the fluid motion using the active fluid controller (active fluid motion control). Both heat pipes could be employed as the thermal switch. The former controls the fluid motion using the asymmetric condenser and evaporator design to manipulate the capillary pressure (capillary pressure is related to the capillary meniscus radius), while the latter controls the heat transfer rate using the mechanical pump-driven fluid motion. During operation, the heat source and sink temperature are reversed, and the latter is controlled by the active fluid motion control: switch mode “On” for fluid motion looping and switch mode “Off” for fluid motion shut off. In the “On” mode, the vapor delivers heat from the evaporator to the condenser, while in the “Off” mode, the condenser is hotter than the evaporator, resulting in a drier condenser than the evaporator [89]. Typically, the size of the porous structures in the condenser is larger than those in the evaporator, which in turn results in relatively larger liquid pressure in the condenser. This leads to a limited

liquid supply to the condenser from the evaporator, and in turn results in a limited heat transfer. This asymmetric heat transfer provides the fluid-motion-controlled thermal switch. The advantages to this approach are that it can be easily scaled up, is flexible to install, and has very low thermal resistance in the “On” mode. The disadvantages are the low “Off” resistance due to the high thermal conductivity of the metallic heat pipe tube, and the fact that it requires a relatively long transient response. Also, the system is limited to a relatively high operating temperature because the fluid needs to be maintained as a liquid (low temperature solidifies the fluid, which shuts off the heat transfer).

### **1.3.2 Atomic-scale phononics-based thermal switch, transistors, and computers**

A key component of advanced thermal management systems is the thermal transistor, knowing that the electrical transistor has made a tremendous impact on modern industries such as radio, calculator, and computers [90, 91]. At the atomic scale, the thermal transistor can be designed by the nonlinear, phononic or quantum thermal transport, and the typical setup has three legs contacted to three heat baths, as shown in Figure 1.8. In general, two legs are subjected to a temperature gradient for the heat transfer, i.e., between  $T_S$  and  $T_D$ , and the switching mechanism operates by controlling the temperature at  $T_G$ , as similarly performed in the electrical transistor, i.e., the electrical potential is biased across the two terminals, while the current between the two terminals is controlled by the other terminal’s voltage. Li et al. [92] have explored the theoretical framework for the working principle using nonlinear phonon transport driven by different atomic-interaction coefficients. The possible negative differential thermal resistance could result in the thermal switch,  $S_{max} \sim 100$ , and thermal transistor, and potentially lead to the thermal logic gate for advanced thermal management system [7]. Joulain et al. [93] have designed the thermal

transistor using the thermally-driven, nonlinear, quantum spin couplings among the three thermal baths.

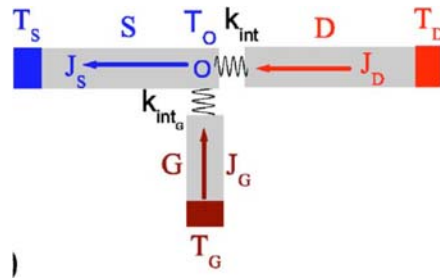


Figure 1.8. Schematic diagram of atomic-scale thermal transistor with thermal bath for thermal transport/control [92].

Using the aforementioned advanced thermal management components, the development of the thermal computer has long been an attractive science and engineering problem. Although the computer needs a combination of basic building blocks, such as thermal diode, switch, transistors, and thermal memory, due to technical challenges, to the best of the authors' knowledge, there are no commercially available thermal computers yet. However, a few significant efforts have been made in the design of practical thermal computers. One approach is to employ the spiral, multi-layered composite approach, and a thermal inversion material has been designed and demonstrated by manipulating the diffusive thermal transport [94]. The structure and material allow for heat concentration and heat current inversion, which control the desired direction of the heat current. This structure could serve as a basic building block for advanced thermal management or new applications such as the thermal computer. For the practical thermal computer, advancements in the other components are required, including thermal memory and its integration into the thermal computing system; however, this advancement is important to demonstrate the possibility of the advanced thermal management system.

### 1.3.3 Outlook for future research

As reviewed above, numerous approaches have been explored using the fundamental “On/Off” theoretical working principles to develop the multiscale thermal switch, and some of the devices have been actively used in applications, including thermal management systems in spacecraft/automobiles and smart building applications. However, these systems have been primarily developed as macroscale systems, and viable solutions to micro-/nanoscale thermal management systems are rare. Also, some of the existing thermal switch systems have limitations relative to the installation/operation/compatibility with other existing thermal management systems, as discussed below.

#### a) Limited operating temperature (cryogenic temperature)

The majority of thermal switch systems operate only at very low (cryogenic) temperatures [84, 87, 88, 95-97]. This is considered a significant bottleneck to designing a thermal switch for higher operating temperature windows (0–500°C), where typical thermal-energy-driven renewable energy systems operate and waste heat needs to be recovered.

#### b) Expensive installation/operating cost

Efficient thermal switches have typically employed additional, complex, active control systems to provide “On/Off” modes such as mechanical (pressure) [84, 87, 88, 95, 96], electromechanical [98-102], magnetomechanical [103-105], and others [106, 107]. Indeed, there is a thermally driven mechanical switch mechanism (passive), but it is limited to operating only at cryogenic temperatures [97].

#### c) Poor compatibility with other existing thermal control systems (diode and switch)

The current thermal switch mechanisms cannot be easily implemented to design desired advanced thermal control systems. This is one of the significant bottlenecks to advanced thermal

signal control systems design for new applications, e.g., thermal logic gates/computing [8-10, 26, 108, 109].

#### **1.4 Conclusion**

Thermal diodes and switches are crucial components for thermal energy savings, scavenging, and thermal management systems. Various approaches have been explored using both theoretical and experimental approaches for nonlinear thermal transport mechanisms. For the thermal diode, macro- to atomic scale thermal energy carriers have been tailored through nonlinear conduction, convection, and radiation mechanisms. Nonlinear thermal conduction has been theoretically explored through micro-/nanoscale asymmetric geometries, heterogeneous interfaces, and asymmetric quantum energy transport, where a few approaches have been experimentally shown using the emerging micro-/nanotechnologies, while the nonlinear convection heat transfer has been experimentally demonstrated for the very efficient degree of rectification in macroscale such as heat pipe or gravity-driven thermal diode. However, the commercialized or practical systems are still far from being implemented since they still remain in the laboratory-level demonstration, poor steady-state performance for micro-/nanoscale systems, or slow transient response.

The development of the thermal switch has been primarily motivated by the cryogenic thermal management system, especially for the thermal management system in NASA spacecraft. Typical approaches have been the mechanical-based thermal switching to control the heat transfer rate between the highly conductive and insulated states, i.e., “On/Off” switching, both in theory and in experimentation. The key is to provide a good degree of the thermal switch, i.e., large contrast ratio of thermal conduction to insulation at steady state, fast enough switching between “On/Off” modes, and slow enough to minimize the overshoot for temperature control. These thermal

switching mechanisms have been explored using the active/passive thermal controlling mechanisms, i.e., gas pressure-driven, differential thermal expansion, and shape-memory alloy.

Some of the developed, thermal diode/switch mechanisms have also been implemented in advanced thermal energy control, i.e., thermal transistor/logic gates, although those primarily remain in theoretical approaches including an atomic-scale approach, i.e., nonlinear, atomic/quantum thermal transport. This approach implies that it could serve as a basic building block for new applications including the thermal computer. Achieving a practical thermal computer has a long way to go and involves the development of basic working principles and practical demonstrations using multiscale thermal transport approaches.

### **1.5 Statement of objective and scope of proposal**

The primary objective of this study is to develop nanoscale thermal management devices for renewable energy engineering, waste heat recovery systems, and completely new energy-management applications, i.e., thermal computers. Nonequilibrium molecular dynamics (NEMD) and Grand Canonical Monte Carlo (GCMC) simulations are used to investigate the potential of the proposed designs in reaching required degrees of thermal diode,  $R$ , and thermal switch,  $S$ . The following chapters are divided based on the proposed models and the physical phenomena for thermal diode or switch.

Chapter 2 examines a novel thermal diode employing gas-filled nanogap (in Knudsen regime) with heterogeneous materials, i.e., heterogeneous nanostructures, so called adsorption-controlled thermal diode. The degree of the thermal diode is studied using nonequilibrium molecular dynamics simulation for Ar gas confined in Pt-based nanogap materials. The asymmetric adsorption and adsorption-controlled thermal accommodation coefficients on the heterogeneous nanogap surfaces result in nonlinear heat flux across the gas-filled nanogap with respect to the

different temperature gradient direction. This in turn leads to the thermal diode with high degree of the thermal diode (or rectification).

Chapter 3 studies a passive thermal switch using adsorption-controlled nanoscale thermal switch mechanism in heterogeneous nanostructures. Nonequilibrium molecular dynamics simulations are used to model Ar-filled two nanogaps with a middle surface having a weaker fluid-solid interaction for a thermal switch valve. The switchable nanoscale thermal transport at the fluid-solid interface through the adsorption-controlled thermal accommodation coefficient of the middle surface leads to the thermal switch “on” and “off”.

Chapter 4 fundamentally investigates the roles of the locally-heterogeneous structures on the adsorption and adsorption-capillary transition in Ar-filled Pt-based nanogaps with various solid-gas surface interactions with/without having nanoposts on one surface only, using GCMC simulations. The adsorption and adsorption-capillary transition are predicted as a function of the gas pressure at given temperature and the surface temperature at given gas pressure. This chapter also examines the effects of the nanopost distance, height, surface interactions as well as the nanogap size on the adsorption and capillary transition. The hysteresis in nanogaps with and without nanoposts is also studied. The outcome of this study provides a key working principle for capillary-controlled thermal diodes and switches using condensable gas-filled heterogeneous nanostructures.

Chapter 5 examines a new class of the thermal diode by employing a large thermal conductivity contrast between gas (adsorption) and liquid (capillary) states in heterogeneous nanostructures, so called, capillary-controlled thermal diode. The effects of the structural and material heterogeneities including the coupled structural-material heterogeneity on the thermal diode are explored using

Ar-filled Pt-based nanogap and Grand Canonical Monte Carlo (GCMC) simulation combined with Non-Equilibrium Molecular Dynamics (NEMD) simulation.

Chapter 6 investigates a new class of thermal switch by using capillary-controlled large thermal conductivity contrast in a nanogap with movable nanopost structures. The switch performance is demonstrated with controlled nanopost height on one surface only, using GCMC simulation combined with NEMD simulations. The heat fluxes across the gas-filled nanostructures and degree of thermal switch are predicted as functions of operating temperature, nanostructure geometries, and solid-fluid interaction parameters. Optimal nanopost geometries and operating conditions are also discussed. The capillary-controlled thermal switch achieves  $S_{max} \sim 170$  in an order of 10 ns.

Chapters 7 summarizes the adsorption-/capillary-controlled thermal diode and switch in condensable gas-filled heterogeneous nanostructures, and discusses the direction for future research on the fundamentals of the tailored nanoscale transport mechanism in heterogeneous nanostructures and their practical applications to the advanced thermal management systems. Also, some experimental studies are proposed to validate the simulation results.

## CHAPTER 2

### ADSORPTION-CONTROLLED THERMAL DIODE IN HETEROGENEOUS NANOSTRUCTURES<sup>1</sup>

#### 2.1 Introduction

A thermal diode (or rectifier) transfers heat only in the favorable direction, which is strongly needed to recycle the waste heat energy [3-5], efficiently use the building energy [6], and completely open new energy-saving applications, i.e., thermal computers [7-11]. However, the main challenges of such systems lie in the extremely difficult manufacturing, poor steady-state efficiency, slow transient response, limited operation conditions, and/or required expensive external thermal control systems [8, 12, 87, 95, 110, 111].

Various designs employing nonlinear heat transfer characteristics, both experimentally and theoretically, have been explored [10, 12, 111]. The first thermal diode has been experimentally demonstrated in the solid state, i.e., Cu/CuO interface,  $R_{max} \sim 1.7$  [14]. The recent emergence of nanotechnology has led to experiments involving the use of asymmetric carbon nanotube,  $R_{max} \sim 0.07$  [8]; asymmetric graphene oxide,  $R_{max} \sim 0.25$  [30]; electrochemically tuned thermal diode material,  $R_{max} \sim 0.5$  [82]; and asymmetric radiative thermal transport,  $R_{max} \sim 0.11$  [11]. To improve the relatively low  $R$ , liquid-based systems have been employed using nonlinear convection in heat pipes,  $R_{max} \sim 200$  [66] and 1,000 [67] or heterogeneous water wettings,  $R_{max} \sim 100$  [68] and 0.46 [69]. However, liquid-based systems result in a relatively slow transient response  $\sim 10$  min, which

---

<sup>1</sup> This entire chapter has been published in the following source:

- Avanesian, T. and Hwang, G., Thermal diode in gas-filled nanogap with heterogeneous surfaces using nonequilibrium molecular dynamics simulation. *Journal of Applied Physics*, 2016. **120**(16): p. 165306.

may limit their performance in some applications. Numerous theoretical frameworks for efficient thermal diode mechanisms have been explored in the literature [4, 5, 9, 12, 23, 25-27, 31, 33-35, 39-41, 45, 50-57, 59, 70-77, 111, 112], but those have not been demonstrated in experiments, due to the necessary expensive or challenging, atomic-level manufacturing technologies. These mechanisms also include nonlinear quantum systems [4, 50-56] which should be a long-term approach for the experiments. Further experimental improvement in steady-state and transient performance requires an innovative approach using a viable theoretical framework for the experimental realization.

## 2.2 Adsorption-controlled thermal diode

In this chapter, a thermal diode is examined using a gas-filled nanogap with heterogeneous gas-solid surface interactions as shown in Figure 2.1.

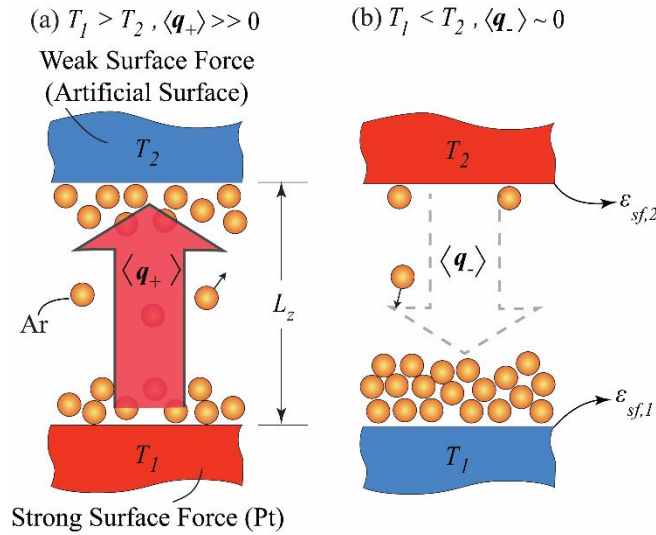


Figure 2.1. A schematic of the adsorption-controlled thermal diode using gas-filled nanogap. (a)  $\langle q_+ \rangle \gg 0$  for  $T_1 > T_2$ , and (b)  $\langle q_- \rangle \sim 0$  for  $T_1 < T_2$  due to the adsorption-controlled asymmetric isotherm and thermal accommodation coefficient (TAC). The surface temperatures,  $T_1$  and  $T_2$ , heat fluxes,  $\langle q_+ \rangle$ , and  $\langle q_- \rangle$ , gas-solid interactions,  $\epsilon_{sf,1}$  and  $\epsilon_{sf,2}$ , nanogap size,  $L_z$ , and the adsorbed particles are also shown.

This aims at developing a new class of thermal diode mechanism via nonlinear gas conduction for efficient steady-state performance and fast transient response.

The thermal conductivity in the gas-filled nanogap (Knudsen regime) is well understood using kinetic theory [113, 114]. In Knudsen regime ( $\text{Kn}_L = \lambda_f/L_z$ ), where the characteristic length of the nanogap,  $L_z$ , is similar to the mean free path,  $\lambda_f$ , the effective thermal conductivity across the gas-filled nanogap is related to the thermal accommodation coefficients (TACs) of both surfaces and the ballistic thermal transport through the gas molecules. In  $0.1 < \text{Kn}_L < 10$  (transition regime), the effective thermal conductivity of gas confined in the nanostructure is given as [113, 114]

$$\langle k_{f,t} \rangle = \langle k_{f,fm} \rangle \left( 1 + \frac{4}{15} \frac{1}{\text{Kn}_L} \frac{a_{T,1} a_{T,2}}{a_{T,1} + a_{T,2} - a_{T,1} a_{T,2}} \right)^{-1}, \quad (2.1)$$

where  $\langle k_{f,fm} \rangle$  is the effective thermal conductivity in free molecular regime ( $\text{Kn}_L > 10$ ), and  $a_{T,1}$  and  $a_{T,2}$  are the TACs at surfaces 1 and 2, respectively. TAC is defined as

$$a_T = \frac{\langle q_{f,z} \rangle - \langle q_{f,z}' \rangle}{\langle q_{f,z} \rangle - \langle q_{f,z}(T_s) \rangle}, \quad (2.2)$$

where  $\langle q_{f,z} \rangle$  and  $\langle q_{f,z}' \rangle$  are the heat flux of the impinging and reflecting gas molecules to/from the solid surface, respectively, and  $\langle q_{f,z}(T_s) \rangle$  is the heat flux between the solid and gas molecules.

The demonstration of the thermal diode in the gas-filled nanogap requires either asymmetric ballistic thermal transport via gas atoms, and/or controlled interfacial thermal transport via TACs with respect to a temperature gradient direction. To control such thermal transport, an Ar gas-filled nanogap with heterogeneous materials is employed having Pt for the lower surface ( $T_1$ ) and an artificial material for the upper surface ( $T_2$ ) that has a weaker gas-solid interaction compared to the lower surface. At an equilibrium state, i.e.,  $T_1 = T_2$ , gas atoms are more attractive to the solid surface due to the stronger gas-solid interaction than fluid-fluid interaction, so called adsorption, but the amount of adsorption onto the Pt surface is larger than that of the weaker gas-solid

interacting surface due to smaller attraction, i.e., heterogeneous adsorption. At a nonequilibrium state,  $T_1 \neq T_2$ , the amount of the adsorption is different from that of the equilibrium state, since the local thermal equilibrium of each surface changes from the different surface temperatures. In fact, the amount of adsorption is determined by the combination of the gas-solid interaction energy and the surface temperature; the stronger the surface energy, the greater is the amount of the adsorption [115]. When the temperature gradient is upward ( $T_1 > T_2$ ), both surfaces have moderate number of adsorbed particles, because the higher temperature of the Pt surface (strong interaction) desorbs Ar atoms, while the lower temperature of the upper surface (weak interaction) adsorbs them. This moderate adsorption on both surfaces leads to large amounts of TAC on both surfaces, resulting in a significant heat transfer across the interfaces. On the other hand, when the temperature gradient is in opposite direction, the high temperature with small gas-solid interaction results in a poor adsorption on surface 2, which leads to a low TAC, whereas the lower temperature with large gas-solid interaction causes a significant adsorption on surface 1 and resulting high TAC. The poor interfacial heat transfer across surface 2 in turn results in a poor overall heat transfer, and this leads to the asymmetric heat transfer, i.e., thermal diode (or rectification). A key heat transfer control mechanism is to control TAC, which requires a nanogap size of the same order of the gas mean free path.

### **2.3 Methodology**

The thermal diode is calculated using nonequilibrium molecular dynamics simulation (NEMD). 576 argon atoms are filled in a nanogap of  $L_z = 20$  nm with  $L_x = 8.864$  nm and  $L_y = 7.676$  nm. The upper and lower surfaces of the nanogap consist of three layered FCC (111) plane solid. One Fixed layer is added as the outermost layer of the upper and lower surfaces in order to keep the particles within the nanogap. Periodic boundary conditions are used for  $x$  and  $y$  directions,

while non-periodic boundary condition is used for  $z$  direction. The interaction among neighboring atoms, i.e., between Ar-Ar and Ar-solid atoms, are modeled using the Lennard-Jones potential, given as

$$\varphi_{ij}(r) = 4\varepsilon_{ij} \left[ \left( \frac{\sigma}{r_{ij}} \right)^{12} - \left( \frac{\sigma}{r_{ij}} \right)^6 \right], \quad r_{ij} < r_c \quad (2.3)$$

where  $\varepsilon_{ff} = 0.2403$  kcal/mol for Ar-Ar [116], and  $\varepsilon_{sf} = 0.1573$  kcal/mol for Ar-Pt [117], and the cut-off distance,  $r_c = 1.2$  nm, is used [117]. The  $\sigma$  is the distance with no repulsive or attractive potentials between the particles. Here,  $\sigma_{\text{Ar-Ar}} = 3.405$  Å and  $\sigma_{\text{Pt-Pt}} = 2.5346$  Å [118] are used, and  $\sigma_{\text{Ar-Pt}} = 2.938$  Å is used employing geometric mixing rule. The Pt-Pt potential interaction is modeled by harmonic potential, given as

$$\varphi_{ij}(r_{ij}) = \frac{1}{2} \Gamma (r_{ij} - r_o)^2, \quad (2.4)$$

where the spring constant,  $\Gamma = 67.360$  kcal/mol-Å<sup>2</sup>, and the equilibrium displacement,  $r_o = 2.77$  Å are used [116]. The gas pressure is calculated using the ideal gas law, given as

$$\langle p_g \rangle = \frac{N_f k_B T_g}{V_g}, \quad (2.5)$$

where  $N_f$  is the number of Ar atoms in the ideal gas region (only 18 nm in the central region excluding 1 nm from each surface),  $k_B$  is the Boltzmann constant, and  $T_g$  is the gas temperature estimated by the simulation. The ratio of  $\varepsilon_{sf,2}$  to  $\varepsilon_{sf,1}$  is shown with  $\varepsilon^*$ , and it is used to compare the strength of gas-solid interaction between the lower and upper surfaces.

Initially, Ar atoms are randomly distributed, and to reach an equilibrium state, NVT ensemble is used for 6 ns with the each time step 2 fs for desired temperature. Then, the simulation is followed by the NEMD, to calculate the ensemble-averaged heat flux,  $q_z$  under a temperature difference of  $\Delta T = 20$  K across the nanogap controlled by Langevin thermostat [119] for additional

14 ns. The various simulations are run for different average temperatures,  $T_{ave}$ ,  $[= (T_1 + T_2)/2]$  from 80 K to 130 K at  $\varepsilon^* = 1.0, 0.75$ , and  $0.5$ . For each set of  $T_{ave}$  and  $\varepsilon^*$ , the temperature gradient is reversed in order to examine the thermal diode, i.e., calculate both  $\langle q_+ \rangle$  and  $\langle q_- \rangle$ . Each simulation is repeated three times using different initial velocity distribution and positions of Ar atoms, to provide error bars.

To validate our approach, the predicted heat flux for  $\varepsilon^* = 1.0$  (homogeneous surfaces) using NEMD reasonably agrees to that using the kinetic theory, Eq. (2.1) as shown in Figure 2.2. Note that the thermal accommodation coefficients (TACs) used in Eq. (2.1) are the predicted from the NEMD (Figure 2.6).

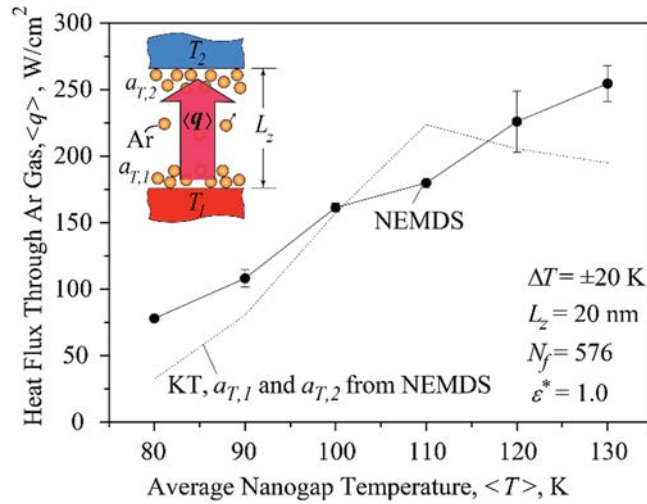


Figure 2.2. Variations of heat flux through the nanogap as a function of average surface temperature both in  $\langle q_+ \rangle$  (solid symbols) and  $\langle q_- \rangle$  (empty symbols) directions, for  $\varepsilon^* = 1.0, 0.75$ , and  $0.5$ . The error bars and insets for the simulation setup are also shown.

Note that the thermal diode is achieved by the control of thermal accommodation coefficient, which requires the nanostructure size to have the same order of the mean free path of the gas. Here,  $L_z = 20$  nm for the gas pressure of 10 to 800 kPa and the temperature of 80 to 130 K.

The resulting ensemble-averaged heat flux across the gas-filled nanogap is calculated using the given relation [119, 120],

$$\langle q \rangle = \frac{1}{V} \left[ \sum_{i=1}^N \frac{1}{2} m_i u_i^2 u_{i,z} + \sum_{i=1}^N \sum_{j>1}^N \varphi_{ij} u_{i,z} - \sum_{i=1}^N \sum_{j>1}^N (\mathbf{r}_{ij} \cdot \mathbf{F}_i) u_{i,z} \right], \quad (2.6)$$

where  $V$  is the volume,  $m_i$  is the mass of the argon particle,  $u_i$  is the particle velocity,  $\varphi_i$  is the potential energy,  $\mathbf{r}_{ij}$  is the displacement separation vector between  $i^{\text{th}}$  and  $j^{\text{th}}$  atoms, and  $\mathbf{F}_i$  is the interactive force vector. The key design parameter for the thermal diode is the asymmetric gas-solid interaction in surfaces 1 and 2. Here, the degree of the asymmetric interaction parameter is given as  $\varepsilon^* = \varepsilon_{sf,2}/\varepsilon_{sf,1}$ . We used  $\varepsilon_{sf,1} = 0.1573$  kcal/mol with  $\varepsilon^* = 0.75$  and  $0.5$  to have heterogeneous surface.

## 2.4 Results and discussion

The predicted heat fluxes [Eq. (2.6)] are shown in Figure 2.3 as a function of the average nanogap temperature, i.e.,  $80 \leq \langle T \rangle \leq 130$ , for  $\varepsilon^* = 1.0, 0.75$ , and  $0.5$ .

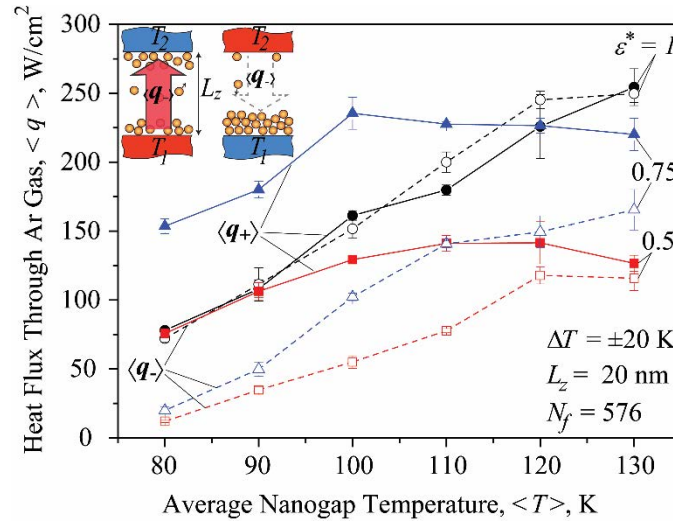


Figure 2.3. Variations of heat flux through the nanogap as a function of average surface temperature both in  $\langle q_+ \rangle$  (solid symbols) and  $\langle q_- \rangle$  (empty symbols) directions, for  $\varepsilon^* = 1.0, 0.75$ , and  $0.5$ . The error bars and insets for the simulation setup are also shown.

For  $\varepsilon^* = 1.0$ , the heat flux increases with increasing average nanogap temperature. A higher surface temperature desorbs the Ar particles (under the fixed number of Ar atoms), resulting in a higher gas pressure and heat flux. In fact, although the high surface temperature results in a lower

TAC (lower heat flux), the heat flux enhancement by the increased pressure outweighs the heat flux decrease by the lower TAC. No significant difference between  $\langle q_+ \rangle$  and  $\langle q_- \rangle$  is found due to the symmetric heat transfer for both temperature gradient directions, i.e., no diode effect,  $R \sim 0$ . However, for  $\varepsilon^* = 0.75$  and  $0.5$  (asymmetric surface interaction), the heat flux when  $T_1 > T_2$  is much higher than when  $T_1 < T_2$ . This asymmetric heat flux is more pronounced in low temperatures, due to significant asymmetric adsorptions onto the nanogap surfaces and resulting gas pressure variation when the direction of temperature gradient changes. Note that there are peaks in  $\langle q_+ \rangle$  at 100 K and 110 K for  $\varepsilon^* = 0.75$  and  $0.5$ , respectively. These deflection points are related to the combined effect of gas pressure-TACs on the heat flux; for lower temperatures, the heat flux increases by increasing the gas pressure without decreasing TACs, whereas for higher temperatures, the heat flux begins to decrease due to the poor TACs.

Using the obtained heat fluxes, the variations of  $R$  [Eq. (1.2)] for  $\varepsilon^* = 1.0, 0.75$ , and  $0.5$  are calculated as shown in Figure 2.4. For  $\varepsilon^* = 1.0$ ,  $R \sim 0$  due to the symmetric heat flux through the homogeneous nanogap. For  $\varepsilon^* = 0.75$  and  $0.5$ , the maximum degrees of the rectification are  $R_{max} = 6.7$  and  $5.6$  at  $T = 80$  K, respectively, due to the adsorption-controlled, gas pressure and TAC. The thermal diode effect decreases down to  $R \sim 0.1$ , at high temperatures, i.e.,  $T = 130$  K, due to no significant adsorption-controlled gas pressure and TAC, i.e., almost identical nanogap pressure for heat flux in positive and negative directions.

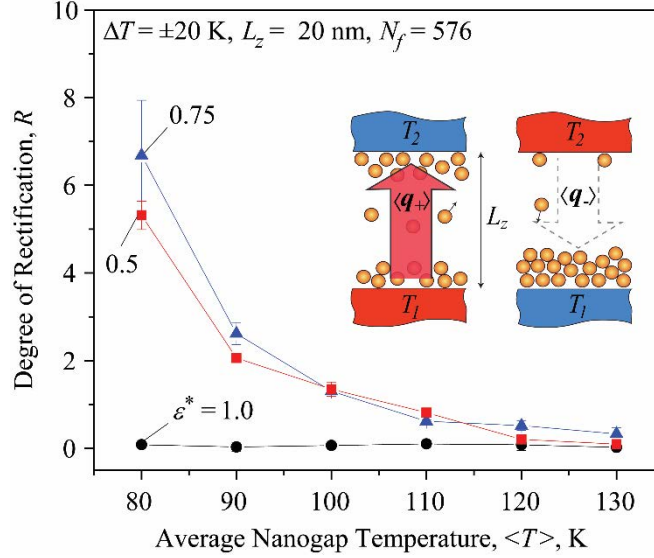


Figure 2.4. Variation of the degree of thermal diode (rectification) using the adsorption-controlled heat flux as a function of average nanogap temperature, for  $\epsilon^* = 1.0, 0.75$ , and  $0.75$  [Eq. (1.2)]. Some error bars are smaller than the size of their corresponding symbols.

To further understand the asymmetric heat flux, the number density of adsorbed Ar atoms near the surfaces,  $n_f$ , are calculated as a function of surface temperature, and the results are shown in Figure 2.5.

In Figure 2.5(a), for  $\epsilon^* = 1.0$  (homogeneous surfaces), the number density of adsorbed particles on the cold temperature surface is higher than that on the hot surface, but it is lower than the liquid Ar. As the surface temperature increases, the number density on the cold surface decreases due to desorption (or higher kinetic energy of Ar particles), while the number density on the hot surface increases due to the adsorption by increased gas pressure. More importantly, when the temperature gradient direction changes, the same number densities are determined near both cold and hot surfaces, i.e., no thermal diode effect. In case of  $\epsilon^* = 0.75$ , for  $\langle q_+ \rangle$ , both surfaces have similar number densities, decreasing with increasing surface temperature, whereas for  $\langle q_- \rangle$ , the number densities of both surfaces are significantly different due to the heterogeneous gas-solid interactions [Figure 2.5(a)]. This in turn results in asymmetric heat flux, i.e., thermal diode. In case of  $\epsilon^* = 0.5$ ,

for  $\langle q_+ \rangle$ , the number density near the cold surface is considerably higher than that near the hot surface, i.e. the difference between them is greater than that for  $\varepsilon^* = 0.75$  due to the large surface interaction heterogeneity, and this difference is more pronounced at low temperatures.

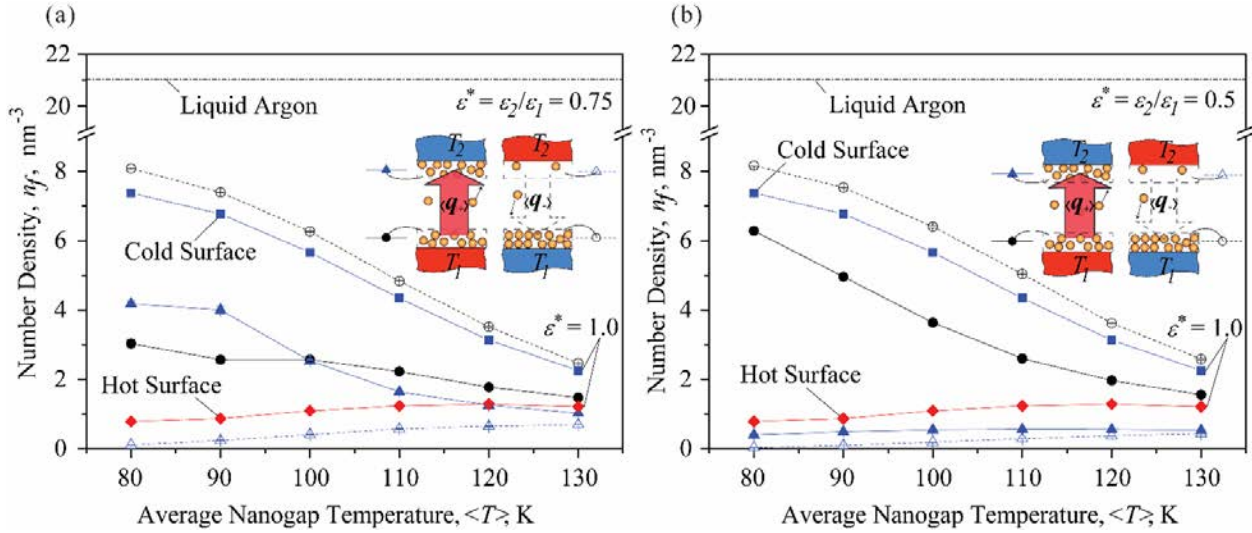


Figure 2.5. The number density of adsorbed particles in the lower and upper surfaces for  $\langle q_+ \rangle$  (solid symbols) and  $\langle q_- \rangle$  (empty symbols), (a)  $\varepsilon^* = 0.75$ , and (b)  $\varepsilon^* = 0.5$ . The insets with the adsorbed Ar particles are also shown. Error bars are shown, but those are smaller than the size of their symbols. The number density of liquid Ar is also shown.

The origin of the thermal diode effect is further articulated by calculating the asymmetric TAC on the heterogeneous gas-solid interactions,  $\varepsilon^* = 0.75$  and  $0.5$ , as shown in Figure 2.6. For  $\varepsilon^* = 1.0$ , the TAC is high,  $a_T \sim 0.9$ , at low surface temperatures due to the significant adsorption and it decreases down to  $a_T \sim 0.5$  as the surface temperature increases up to  $T = 140$  K. The predicted TACs reasonably agree to that of the previous studies [121-123]. Moreover, the TAC does not change when reversing the temperature gradient direction. However, for  $\varepsilon^* = 0.75$  [Figure 2.6 (a)], in  $\langle q_+ \rangle$ , the TAC for the strong surface is significantly higher than that for the weak surface, and TACs for both surfaces decrease with increasing surface temperatures. In  $\langle q_- \rangle$ , the TAC on the strong surface is similar to that for  $\langle q_+ \rangle$ , whereas the TAC on the weak surface is lower than that for  $\langle q_+ \rangle$ , especially at low temperatures. This asymmetric TAC causes the thermal diode. For  $\varepsilon^*$

= 0.5 [Figure 2.6 (b)], the difference between the TACs in  $\langle q_+ \rangle$  and  $\langle q_- \rangle$  is much larger than the case for  $\varepsilon^* = 0.75$ , but the TACs are symmetric between  $\langle q_+ \rangle$  and  $\langle q_- \rangle$ . Even though the TACs are symmetric, we observe the significant thermal diode effect as shown in Figure 2.4.

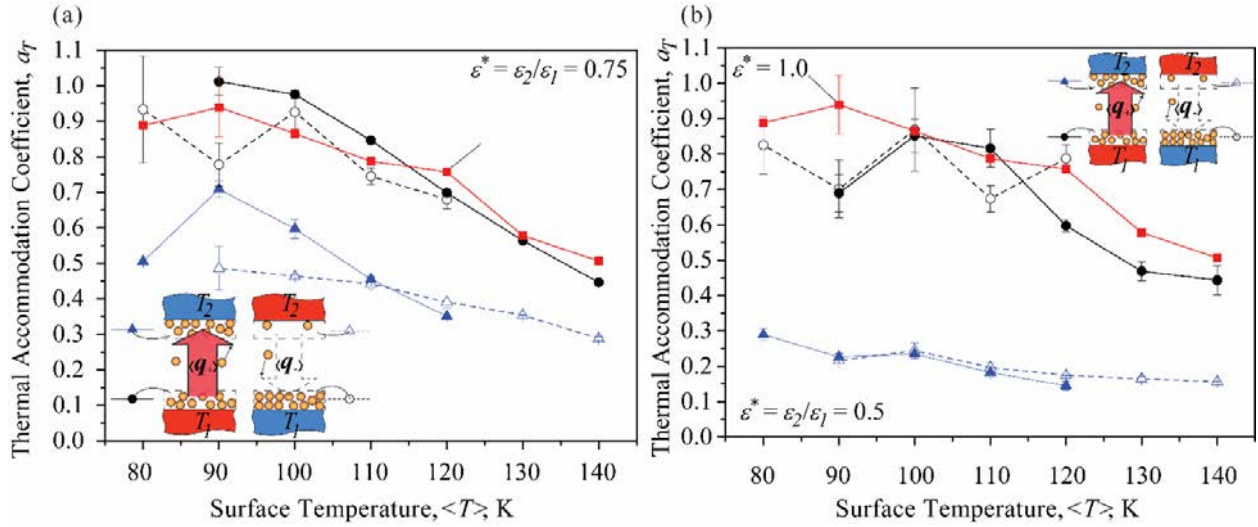


Figure 2.6. Variations of the thermal accommodation coefficient,  $a_T$ , for (a)  $\varepsilon^* = 1.0, 0.75$  and (b)  $\varepsilon^* = 1.0, 0.5$  as a function of surface temperature both in  $\langle q_+ \rangle$  (solid symbols) and  $\langle q_- \rangle$  (empty symbols) directions. Error bars and insets with adsorbed particles are also shown.

To further elucidate the origin of the thermal diode effect, the gas pressure of the nanogap is calculated as shown in Figure 2.7 as a function of average nanogap temperature. For  $\varepsilon^* = 1.0$ , the gas pressure is symmetric, however, for  $\varepsilon^* = 0.5$ , the gas pressure for  $\langle q_+ \rangle$  is much higher than that for  $\langle q_- \rangle$  due to large desorption from the strong surface for  $\langle q_+ \rangle$  and significant adsorption onto the strong surface for  $\langle q_- \rangle$ .

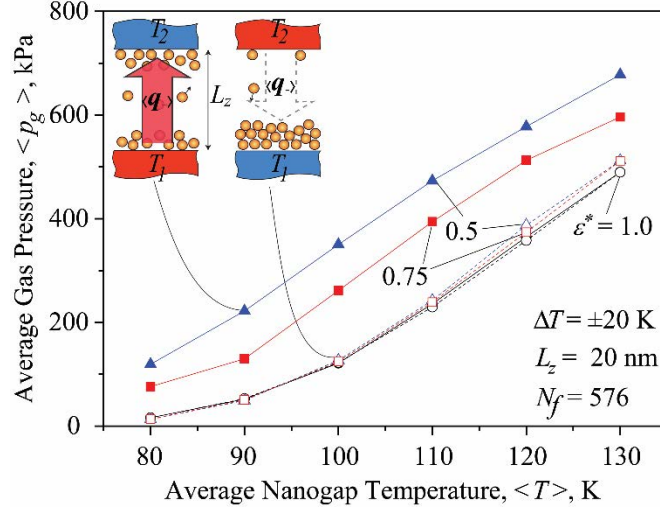


Figure 2.7. Average pressure within the nanogap far from the effect of gas-surface interaction both in  $\langle q_+ \rangle$  (solid symbols) and  $\langle q_- \rangle$  (empty symbols) directions for  $\epsilon^* = 1.0, 0.75$ , and  $0.5$ . Error bars are smaller than symbol size.

This indicates the dominant source of the thermal diode effect for reversed temperature gradient direction where TACs are symmetric, as shown in Figure 2.6(b). For  $\epsilon^* = 0.75$ , this gas pressure change is less pronounced compared to  $\epsilon^* = 0.5$ , i.e., by a factor of 2 ( $\langle p_{g,+} \rangle / \langle p_{g,-} \rangle \sim 9$  for  $\epsilon^* = 0.5$  and  $\langle p_{g,+} \rangle / \langle p_{g,-} \rangle \sim 5.5$  for  $\epsilon^* = 0.75$  at  $\langle T \rangle = 80$  K), showing that the change in gas pressure combined with the asymmetric TAC causes the thermal diode.

## 2.5 Conclusion

In this study, the adsorption-controlled thermal diode is examined using the Ar-gas-filled heterogeneous nanogap. The thermal diode effect is caused by the asymmetric gas pressure combined with TACs under different strengths of solid-gas interaction, showing the maximum degree of rectification,  $R_{max} \sim 7$  for  $\epsilon^* = 0.75$  at  $T = 80$  K. For  $\epsilon^* = 0.75$ , the thermal diode is originated by the combination of the adsorption-controlled asymmetric gas pressure and TACs, while for  $\epsilon^* = 0.5$ , it is dominantly controlled by the asymmetric gas pressure. The obtained results for the Ar-filled Pt-based nanogap with the tailored materials provides a design guideline for the thermal diode using real materials.  $\epsilon^* = 0.75$  and  $0.5$  can be designed using Pt/Ni and Pt/Al as

strong/weak surfaces based on the LJ potential in literature, respectively.[124] The developed thermal diode can serve as a basic building block to design advanced thermal systems such as thermal switches and thermal computing systems.

## CHAPTER 3

### ADSORPTION-CONTROLLED THERMAL SWITCH IN HETEROGENEOUS NANOSTRUCTURES<sup>1</sup>

#### 3.1 Introduction

A thermal switch is a system designed to switch the heat current “on” and “off” between a heat source and a heat sink. For a desired switch operation, a thermal control component using either active or passive methods is required. For active control, external (mechanical, electrical, etc.) power sources are used, while the passive control is applied by thermally self-regulated phenomena such as mechanical-/thermal-actuator driven switching mechanisms.

An efficient thermal switch should be able to act like a good conductor for the “on” mode and a good insulator in the “off” mode when the same temperature gradient is maintained between the source and the sink. In addition, this should be done abruptly and yet appropriately damped by thermal capacitance and mechanical characteristics to avoid overshooting the desired target temperatures. Degrees of thermal switch varying from 100 to 1000 with transient response time from 1 to 60 seconds have been reported in literature [111]. A common approach for thermal switching is to apply a physical movement [125]. This can be designed using the difference between the thermal expansion coefficients (TEC) of two solid materials. However, this approach has limitations such as the small differential TEC ( $\sim 1 \mu\text{m}/\text{K}$ ) and the need for a large coefficient

---

<sup>1</sup> This entire chapter has been published in the following source:

- Avanesian, T. and Hwang, G., Adsorption-Controlled Thermal Switch Using Nonequilibrium Molecular Dynamics Simulation. ASME 2016 International Mechanical Engineering Congress and Exposition. 2016. American Society of Mechanical Engineers.

difference or temperature gradient as well as an extra space for the required mechanical movement. Vanoost et al. [125] as well as Wang et al. [86] have shown cryogenic thermal switching with  $S_{max} = 550$  and 322, respectively. Another thermal switching method is using gas-filled micro-/nanogaps [87, 88, 126]. In such systems, the heat flux is controlled by the gas-pressure inside the gap and the pressure change is applied using sorption pumps [91]. A  $S_{max} \sim 3.5$  is achieved by these systems in very low temperatures ( $\sim 4$  K). In paraffin-based thermal switches, the mechanical movement is applied by the aid of volume change during the freezing/melting process which supplies the required force to activate the thermal switch [90]. The main disadvantage of this system is its low transient response ( $\sim 1$  minute). The asymmetric heat transfer in heat pipes as well can be used to design fluid-motion controlled thermal switches [7], although they have relatively low  $S$ , long transient response, and their use is limited to high operating temperatures. In atomic scale, phononic-/quantum-based thermal switches and transistors are proposed for applications such as advanced thermal management systems and degrees of thermal switch as high as  $\sim 100$  are reported [7, 90, 114].

This study examines an adsorption-controlled setup consisting of two adjacent gas-filled nanogaps with heterogeneous solid-gas interactions as a completely new class of thermal switches. In Knudsen regime, the heat transfer across the gas-filled nanogap is related to the thermal accommodation coefficient (TAC) [113, 119]. When the temperature gradient is from the stronger surface to the weaker surface (surface with weaker solid-gas interaction), gas particles will be adsorbed on both sides due to the local thermal equilibrium. This leads to a good thermal accommodation coefficient [119, 127] and consequently a good heat flux from the stronger to the weaker surface. On the other hand, when the temperature gradient is in reverse direction, the hotter surface with the weak surface interaction results in poor adsorption, which in turn leads to a small

thermal accommodation coefficient and minimal heat transfer. It is already shown in chapter 2 that this asymmetric heat transfer provides the thermal diode. The same approach is used here to design a thermal switch as shown in Figure 3.1, where surfaces 1 and 2 have a stronger gas-solid interaction than that of surface 3. For the “on” mode (no active temperature control for surface 3), the heat transfer is expected to occur along with the temperature gradient from  $T_1$  to  $T_2$  (Fourier’s law), while the middle surface serves as a “heat carrying” surface sandwiched by the gas with the two different temperatures. For the “off” mode (active temperature control of surface 3), the higher temperature of surface 3 (compared to  $T_1$  and  $T_2$ ) with weaker surface gas-solid interaction result in the larger desorption of gas particles from the surface 3 (no significant adsorption), which causes the poor heat transfer from the surface 3 to the other surfaces (“off” mode). One of the main advantages of the adsorption-controlled thermal switch is the fact that the thermal switching mechanism is controlled by the temperature of the switching lead without any mechanical moving parts or active controllers (passive control). This working principle leads to a smaller and more reliable system, and incorporates into other existing thermal management systems, e.g., thermal diode [128] in order to design advanced thermal management systems, i.e., logic gate [91].

### **3.2 Non-equilibrium molecular dynamics simulation (NEMD)**

To examine the thermal switch, we employed two adjacent, same size of nanogaps with dimensions of  $L_x = 4.432$  nm,  $L_y = 3.838$  nm, and  $L_{z,1} = L_{z,2} = 20$  nm (the entire simulation size is  $L_z = 41.81$  nm). Each nanogap is filled with 144 argon atoms to transfer heat among them. The bottom ( $T_1$ ) and top ( $T_2$ ) surfaces serve as a heat source and a heat sink, respectively, while the middle surface ( $T_3$ ) is a control lead for the thermal switch by changing the temperature. The periodic boundary conditions were used for  $x$ - and  $y$ - axes, while the fixed non-periodic boundary was used for  $z$ -axis to create the temperature gradient between the bottom and top surfaces

(nonequilibrium state). We chose the operating temperature of  $T_1 = 100$  K,  $T_2 = 80$  K, and  $90 \leq T_3 \leq 120$  K, and for the “on” mode,  $T_3$  was not controlled (allowing the simulation to determine it by  $T_1$  and  $T_2$ ), while for the “off” mode,  $T_3$  is controlled from 100 to 120 K, to study the thermal switch.

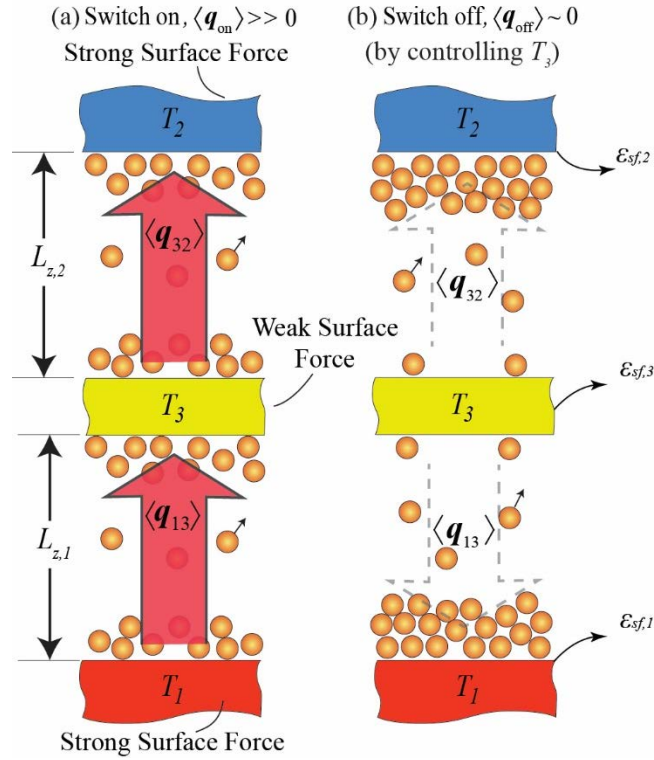


Figure 3.1. A schematic of the adsorption-controlled thermal switch. (a) Large heat flux for “on” mode by the high thermal accommodation coefficients and (b) small heat flux for “off” mode by poor thermal accommodation coefficients (adsorption-free surface on the middle surface).

The adsorption-controlled TAC requires the Knudsen regime. The pressure and temperature ranges within those of the condensable gas, i.e., temperature is greater than the triple phase temperature,  $T_{tr} = 84$  K ( $p_{tr} = 68.9$  kPa) yet lower than the critical temperature,  $T_c = 151$  K. The higher, middle, and lower surfaces of the setup consist of three layers of Face Centered Cubic (FCC, 111 plane) solid (568 Pt atoms). One fixed layer is added as the outermost layers to the highest and lowest surfaces in order to prevent the setup from moving freely, i.e., fixed atoms for

$T_1$  and  $T_2$ . Argon gas atoms are uniformly distributed through the upper and lower nanogaps as an initial setup. The velocity-Verlet algorithm is used for the time integration over time steps of 2 fs [129]. To achieve equilibrium state, the simulation was run for 6 ns using Nose-Hoover thermostat at  $T = 90$  K, for the entire system [130, 131]. Then, the temperature gradient is created by controlling the upper/lower surface temperatures using Langevin thermostat [132] for 14 ns, while the kinetic energy (temperature) of the solid atoms is maintained using the random force input as well as the appropriate “damping”. For the “on” mode, the middle surface was simulated using NVE ensemble, while for the “off” mode, the middle surface temperature was controlled using Langevin thermostat  $100 \text{ K} < T_3 < 120 \text{ K}$  (NVT). It should be noted that the middle surface has three fixed atoms in the center and two corners of its central layer to avoid free movement. Note that for the “on” mode, there is an expected heat leakage through the three fixed atoms, however, this heat leakage is negligibly small, only  $\sim 1\%$  (estimated by the ratio of the number of fix, 3, to the number of the entire middle surface atoms, 256). For “off” mode as the thermostat actively controls the middle surface temperature, the heat leakage does not influence the simulation results since it is “compensated” by the thermostat. During the non-equilibrium MD, the ensemble-averaged heat flux in  $z$  direction,  $\langle q_{g,z} \rangle$ , is calculated for both the “on” and “off” modes.

The interactions between Ar-Ar and Ar-solid particles are modeled by the Lennard-Jones potential given as

$$\varphi_{ij}(r) = 4\varepsilon_{ij} \left[ \left( \frac{\sigma}{r_{ij}} \right)^{12} - \left( \frac{\sigma}{r_{ij}} \right)^6 \right], \quad r_{ij} < r_{cut-off}, \quad (3.1)$$

where  $\varepsilon_{ff} = 0.2403$  kcal/mol for Ar-Ar [133],  $\varepsilon_{sf} = 0.1573$  kcal/mol for Ar-Pt,  $r_{cut-off} = 1.2$  nm [117], and  $\sigma$  indicates the distance for which no repulsive or attractive potential exists between particles. For Ar – Ar interaction  $\sigma_{Ar-Ar} = 3.405 \text{ \AA}$  and for Ar – Pt interactions the geometric mixing

rule is used to determine  $\sigma_{\text{Ar-Pt}} = 2.938 \text{ \AA}$  based on  $\sigma_{\text{Ar-Ar}}$  and  $\sigma_{\text{Pt-Pt}} = 2.5346 \text{ \AA}$  [118]. The Pt-Pt particle interactions are modeled by harmonic potential given as

$$\varphi_{ij}(r_{ij}) = \frac{1}{2}\Gamma(r_{ij} - r_o)^2, \quad (3.2)$$

where  $\Gamma = 67.360 \text{ kcal/mol-\AA}^2$ , and  $r_o = 2.77 \text{ \AA}$  [133]. The pressure within the nanogaps can be calculated using the ideal gas law given as

$$\langle p \rangle = \frac{N_f k_B T_g}{V_g}, \quad (3.3)$$

where  $N_f$  is the number of fluid particles in the gas region defined as the region excluding 1 nm far from each surface due to the significant adsorption within it, i.e., 18 nm only in the nanogap regions,  $k_B$  is the Boltzmann constant,  $T_g$  is the gas temperature calculated by the NEMD, and  $V_g$  is the volume of the gas region. To run the simulations, the Large-scale Atomic/Molecular Massively Parallel Simulator (LAMMPS) was used [134, 135].

The surface interaction ratio,  $\varepsilon^* = \varepsilon_{sf}/\varepsilon_{sf,Ar-Pt}$ , is used to represent the degree of the gas-solid interactions for the upper, lower, and middle surfaces. For the surface 3,  $\varepsilon^* = 0.4$  and  $0.5$  are used, where  $\varepsilon^* = 0.4$  can be designed by the Pb (compared to Pt) [118].

### 3.3 Validation of NEMD results with kinetic theory

To validate the NEMD approach and results, the heat flux calculations using NEMD for the case of  $\varepsilon_3^* = 1.0$  with  $T_1 = 100 \text{ K}$ ,  $T_2 = 80 \text{ K}$ , and  $100 < T_3 < 120 \text{ K}$  (“off” mode) are compared with those calculated by the kinetic theory as shown in Figure 3.2, showing a reasonable agreement.

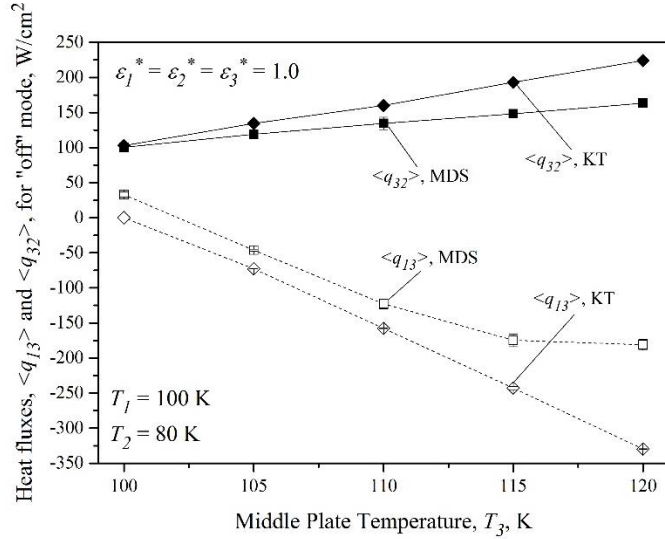


Figure 3.2. Comparison of the heat flux calculated for the “off” mode using NEMD and kinetic theory (KT) where  $\epsilon_1^* = \epsilon_2^* = \epsilon_3^* = 1.0$  ( $T_1 = 100$  K,  $T_2 = 80$  K, and  $T_3 = 100$  to  $120$  K). Error bars are also shown.

Figure 3.3 shows the variation of the Kn number for different temperatures of the middle plate ( $T_3$ ) and  $\epsilon_3^* = 0.4, 0.5,$  and  $1.0$  in “off” mode, indicating that all the simulations take place in transition regime.

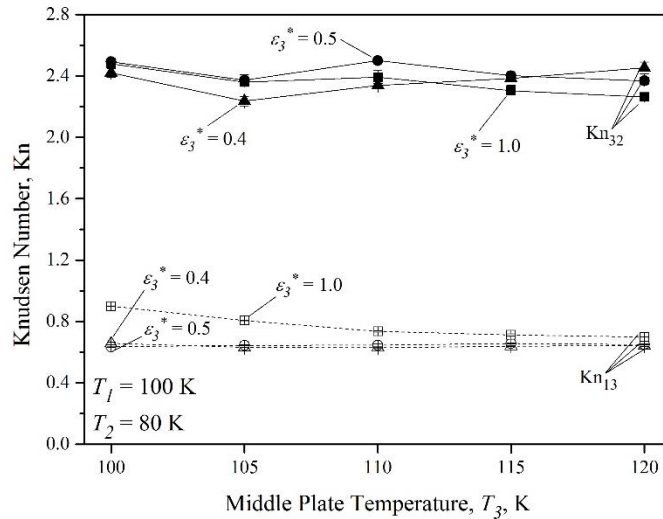


Figure 3.3. Variation of the Knudsen number, Kn, in the lower and upper nanogaps for  $\epsilon_3^* = 0.4, 0.5,$  and  $1.0$ , and  $T_3$  from 100 to 120 K. Error bars are also shown.

### 3.4 Results and discussion

For the adsorption-controlled thermal switch, we use  $\varepsilon_1^* = 1$ ,  $\varepsilon_2^* = 1$ , and  $\varepsilon_3^* = 0.4, 0.5$ , and 1.0. During the simulation, the bottom surface,  $T_1$ , and top surface,  $T_2$ , serve as a heat source and heat sink respectively, while  $T_1 = 100$  K and  $T_2 = 80$  K are maintained both for “on” and “off” modes. The middle surface,  $T_3$ , serves as a switch surface. For the “on” mode, there is no need to control  $T_3$ , while in the “off” mode,  $T_3$  is increased by the external heat bath to reduce the thermal conductance. A key idea is to decrease the gas-solid interaction, i.e., low thermal accommodation coefficient, at relatively high temperature on the weak gas-solid interaction [119, 128], which results in low overall thermal conductance across the nanostructure, i.e., “off” mode. We use  $T_2 = 80$  K since this is close to the triple phase temperature of argon, i.e., significant adsorption on the upper surface. Table 3.1 summarizes the MDS results for the heat flux  $\langle q_{32} \rangle$  from the middle surface,  $T_3$ , to the upper surface,  $T_2$ , and the heat flux  $\langle q_{13} \rangle$  from the bottom surface,  $T_1$ , to the middle surface,  $T_3$ , during the “on” mode at  $T_1 = 100$  K and  $T_2 = 80$  K and  $\varepsilon_3^* = 0.4, 0.5$ , and 1.0. Note that the overall heat flux for the “on” mode,  $\langle q_{on} \rangle$  is calculated using the average between  $\langle q_{32} \rangle$  and  $\langle q_{13} \rangle$ .

Table 3.1 Heat flux through the thermal switch in “on” mode ( $T_1 = 100$  K and  $T_2 = 80$  K)

$\varepsilon_3^*$	$T_3$ , K (predicted)	$\langle q_{13} \rangle$ , W/cm <sup>2</sup>	$\langle q_{32} \rangle$ , W/cm <sup>2</sup>	$\langle q_{on} \rangle$ , W/cm <sup>2</sup>
0.4	92.23	91.169	43.913	67.541
0.5	89.81	31.694	81.012	56.353
1.0	89.16	82.206	81.447	81.827

Figure 3.4 shows the “off” mode simulation results for the three cases of  $\varepsilon_3^* = 0.4, 0.5$ , and 1.0, while  $T_3$  is controlled from 100 to 120 K at  $T_1 = 100$  K and  $T_2 = 80$  K. Note that the smaller absolute magnitude of the heat flux between  $\langle q_{32} \rangle$  and  $\langle q_{13} \rangle$  is used for  $\langle q_{off} \rangle$  in Eq. (1.3) for the degree of thermal switch,  $S$ . For  $\varepsilon_3^* = 1.0$ , at  $T_3 = 100$  K, the heat flux in the upper nanogap,  $\langle q_{32} \rangle$ ,

is larger than that of the lower nanogap,  $\langle q_{13} \rangle$ , due to the smaller temperature gradient in the lower nanogap. However, the increase of the absolute magnitude of  $\langle q_{13} \rangle$  becomes sharper than that of  $\langle q_{32} \rangle$ , as  $T_3$  increases, although the temperature gradient between  $T_3$  and  $T_2$  is larger than that between  $T_1$  and  $T_3$ . This is because the  $T_2$  is lower than the triple phase temperature of Ar ( $T_{tr} = 84$  K), which in turn results in a significant adsorption onto the surface 2 and resulting low pressure in the upper nanogap regardless of  $T_3 = 100$  to 120 K.

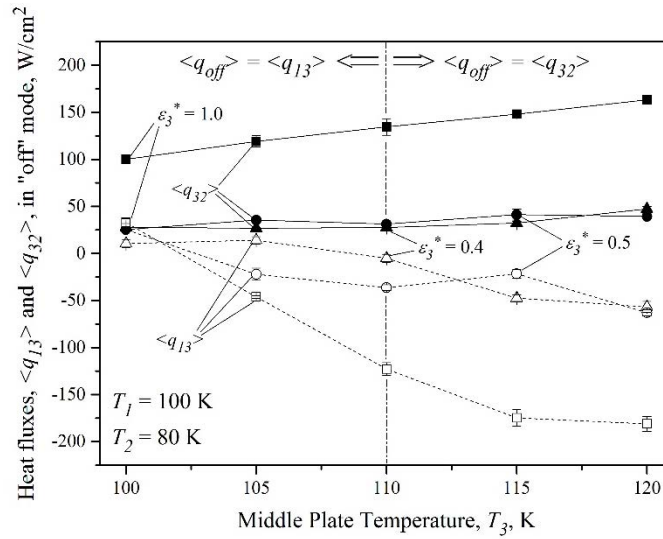


Figure 3.4. Heat flux in the thermal switch in “off” mode ( $T_1 = 100$  K,  $T_2 = 80$  K) as a function  $T_3$  from 100 K to 120 K for  $\epsilon_3^* = 0.4, 0.5$ , and 1.0 (for both upper and lower nanogap). Error bars are also shown.

For  $\epsilon_3^* = 0.4$  and 0.5, the  $\langle q_{13} \rangle$  and  $\langle q_{32} \rangle$  are smaller than those of  $\epsilon_3^* = 1.0$  for all the temperatures, due to the weaker gas-solid interaction in the surface 3. This poor heat flux could serve as the “off” mode. Note that for  $T_3 < 110$  K, the  $\langle q_{13} \rangle$  is smaller than  $\langle q_{32} \rangle$  since the temperature gradient over the lower nanogap is smaller than that of the upper nanogap, while for  $T_3 > 110$  K, the  $\langle q_{13} \rangle$  is larger than  $\langle q_{32} \rangle$  because the  $\langle q_{32} \rangle$  does not increase much (poor heat transfer) since the surface 3 has large desorption resulting from a significant adsorption onto surface 2 (low temperature). This large adsorption can be observed in the small gas pressure in the

upper nanogap as shown in Figure 3.5, meaning that there are not many argon particles travelling from the middle surface to the upper one to carry energy, i.e., poor heat flux. Thus, the “off” mode heat flux,  $\langle q_{off} \rangle$  can be represented by  $\langle q_{13} \rangle$  at  $T_3 < 110$  K, while  $\langle q_{off} \rangle = \langle q_{32} \rangle$  at  $T_3 > 110$  K.

The degree of the thermal switch,  $S$ , is calculated using Eq. (1.3) based on the data given in Table 3.1 and Figure 3.4, and the results are shown in Figure 3.6 as a function of the middle plate temperature  $T_3$  from 100 to 120 K for  $\epsilon_3^* = 0.4, 0.5,$  and  $1.0$ . Note that the  $S$  is calculated based on the average heat flux at  $\epsilon_3^*$  and  $T_3$  from the 3 different simulations with different initial velocity profiles. For  $\epsilon_3^* = 1.0$ , there is no significant switching effect,  $S < 3$ , for all the temperatures, due to a symmetric heat transfer with the homogeneous gas-solid interactions for all the surfaces. However, for  $\epsilon_3^* = 0.4$  and  $0.5$ , the  $\langle q_{13} \rangle$  and  $\langle q_{32} \rangle$  shows nonlinear heat flux (see Figure 3.4) as the  $T_3$  increases, due to the heterogeneous gas-solid interaction and nonlinear TAC, especially at high  $T_3$  [119, 128].

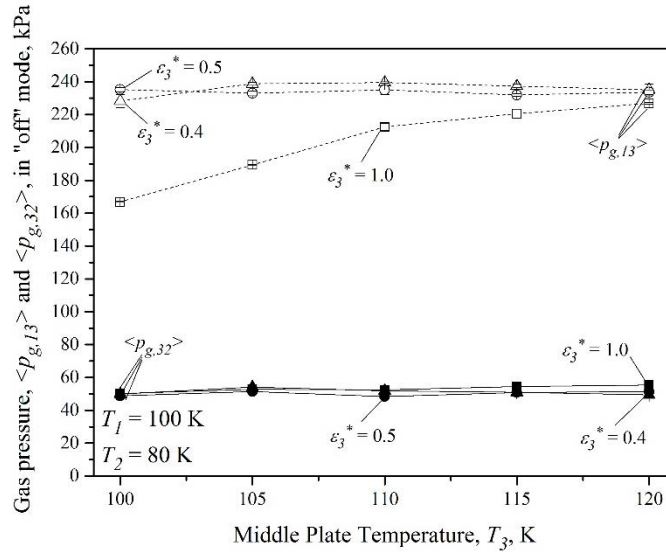


Figure 3.5. Variations of the gas pressure,  $\langle p \rangle$  in the lower and upper nanogaps as a function of  $T_3$  from 100 to 120 K for  $\epsilon_3^* = 0.4, 0.5,$  and  $1.0$ . Error bars are also shown.

Interestingly, for  $\epsilon_3^* = 0.4$ , it shows  $S_{max} \sim 13$  at  $T_3 = 110$  K. Although this is an interesting, reproducible result, the exact origin is currently under study including the adsorption-controlled

TAC, similarly performed in the previous work [119, 128]. Note that at  $T_3 = 100$  K, there is no significant temperature gradient across the lower nanogap, which the thermal switching effect is not caused by the adsorption-controlled nonlinear heat transfer but by the small temperature gradient.

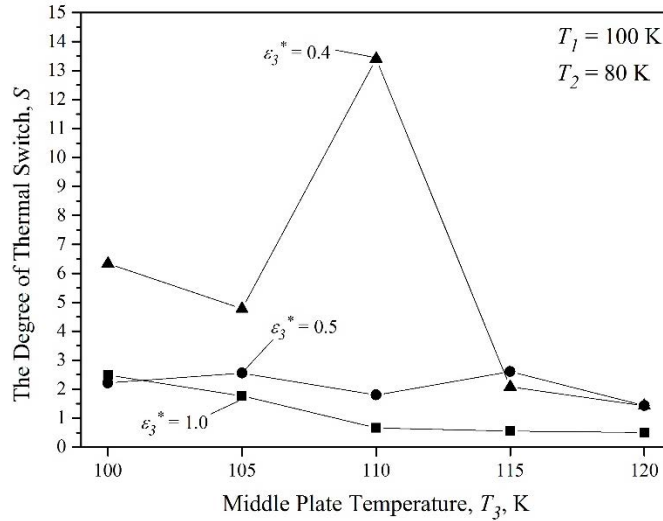


Figure 3.6. Variations of the degree of the thermal switch,  $S$ , in the lower and upper nanogaps for  $\epsilon_3^* = 0.4, 0.5$ , and  $1.0$ , and  $T_3 = 100$  to  $120$  K. Average heat fluxes are used for  $S$  (no error bars).

Indeed, the adsorption-controlled TAC is related to both the pressure (or  $Kn_L$ ) and temperature [119, 128]. As a first step, the Knudsen number for the upper and lower nanogaps are reported with respect to the middle plate temperature as shown in Figure 3.3. The maximum Knudsen number found at  $T_3 = 110$  K for  $\epsilon_3^* = 0.4$  may be resulted from the relatively poor TAC near the middle surface as a result of low solid-gas interaction. For the future work, we work on the adsorption-controlled TAC on the middle surface, including the adsorption isotherm in the nanogap with the heterogeneous surface interactions.

For further improvement, the optimal material selection, i.e., optimal combination of  $\epsilon^*$  for all the three surfaces and optimal nanostructure including the gap size and the surface structure are the factors having the biggest impact on increasing  $S$ . Also, the optimal operating conditions need

to be explored including the surface temperatures and pressure for the desired adsorption-controlled TAC aimed at high  $S$ .

### 3.5 Conclusion

In this chapter, the adsorption-controlled thermal switch is examined using Ar gas-filled nanostructures (two nanogaps) with heterogeneous solid-gas interactions, using NEMD. Results show that the maximum degree of the thermal switch,  $S_{max} \sim 13$ , can be achieved at  $T_3 = 110$  K under  $T_1 = 100$  K and  $T_2 = 80$  K, which is controlled by a weak surface interaction plate ( $\varepsilon^* = 0.4$ ) between two stronger plates ( $\varepsilon^* = 1.0$ ). The efficiency of the thermal switch can be further improved by using optimal material selections and nanostructure geometries to further decrease the TAC. This work provides a deep insight into designing advanced thermal management systems such as adsorption-controlled thermal transistors and thermal computing systems.

## CHAPTER 4

### ADSORPTION-CAPILLARY TRANSITION IN HETEROGENEOUS NANOSTRUCTURES<sup>1</sup>

#### 4.1 Introduction

Understanding adsorption and capillary transition in nano-/meso-scale porous media is crucial for the characterizations of the pore-size distribution and surface areas, and efficient operations in various energy and phase-separation processes [136, 137]. In low gas pressures, the gas molecules adhere to the solid surfaces, i.e., adsorption, due to the stronger gas-solid interactions compared to the gas-gas interactions, and as the gas pressure increases, the adsorption-capillary transition occurs by filling the entire porous structures with gas particles below the saturation pressure [138, 139].

The adsorption isotherm has been understood via various theoretical framework, including Freundlich model [140], Langmuir model [141], Brunauer, Emmet, Teller, i.e., BET model [142, 143], and Frenkel-Halsey-Hill (FHH) model [144-146] for high relative pressures. As the gas pressure increases, the adsorbed layers grow, and when those layers become closer, the adsorbed layers result in morphological transition to the capillary state, so called adsorption-capillary transition. For homogeneous porous structures, the adsorption-capillary transition pressure at given temperature is predicted using Kelvin-Cohan (KC) equation [147], given as

---

<sup>1</sup> This entire chapter has been submitted for publication to the following source:

- Avanesian, T. and Hwang G., Adsorption and capillary transition in heterogeneous nanostructures using Grand Canonical Monte Carlo simulation. International Journal of Heat and Mass Transfer, Submitted July 2017.

$$RT \ln(p / p_o) = -\frac{\sigma V_L}{r_c - t}, \quad (4.1)$$

where  $\sigma$  is the surface tension,  $V_L$  is the molar volume of the bulk liquid, and  $r_c$  is the pore radius.  $t$  is the thickness of the adsorbed layers on the verge of the capillary transition, which is predicted using the following relation [139],

$$t = \left(\frac{n}{n_m}\right)d_m. \quad (4.2)$$

$d_m$  is the effective thickness of the monolayer predicted by

$$d_m = \frac{V_L}{A_m N_A}, \quad (4.3)$$

where  $N_A$  is the Avogadro number and  $A_m$  is the average occupying area of each molecule in the adsorbed layer [139, 148]. However, Eq. (4.1) does not reasonably predict the adsorption-capillary transition for pore sizes smaller than 20 nm [149, 150]. Derjaguin–Broekhoff-de Boer [151] and Cole-Saam [152] have improved the theoretical models, especially for pore sizes larger than 7 nm [149], considering the mechanism of pore transition, hysteresis, and the effect of the curvature on the thickness of the adsorbed layers [138]. Nicholson [153] has applied mean-field calculations to a gas-confined single cylindrical capillary with various pore radii. Based on the work by Celestini [154], Pellenq et al. [155] have used a phenomenological method to describe the hysteresis in the confinement of pure fluids in cylindrical mesopores. Adolphs has modified Eq. (4.1) with the combination of the Excess Surface Work (ESW) and disjoining pressure approach to improve the prediction accuracy on the sorption isotherm in cylindrical and slit-like mesopores. However, the aforementioned theoretical approaches have poorly predicted the capillary transition in narrow mesopores [149, 156], due to lacks of atomic-level descriptions on the gas-solid interaction and oversimplified assumptions on the density of adsorbed layers [138]. Newly developed models such as zeta-isotherm have improved the accuracy to predict the

adsorption isotherm [157-159], however these theoretical models primarily focus on homogeneous porous structures, and those require articulated atomic-level descriptions to reasonably study the heterogeneous porous structures.

To further improve the atomic-level understandings on the adsorption and capillary transitions, various numerical approaches, such as Density Functional Theory (DFT) and the Grand Canonical Monte Carlo simulation (GCMC) have been employed with the inclusion of articulated inter-atomic gas-solid interactions and various geometries (slit-like, cylinders etc.) at the expense of the computational cost [139, 149]. Using the mean-field density functional approach originally introduced between a fluid and a single wall [160, 161], Evans et al. have examined the adsorption isotherm and capillary transition in both two-wall gaps [162] and cylinders [163]. Van Megan and Snook [164] and Stroud et al. [165] have used GCMC calculations to examine the adsorption isotherm and capillary transition of a Lennard-Jones fluid in a slit-like nanogap. Lane and Spurling [166, 167] and Freasier and Nordholm [168] have investigated the effect of the nanogap size on the adsorption isotherm, showing that the gas configuration is stable at larger nanogaps, and the liquid configuration is stable at smaller ones. Coasne et al. [169] have examined the adsorption isotherm of nitrogen onto silicon pores open at one or both ends, showing that unlike the predictions by Cohan [147], the hysteresis is observed for both cases.

The experimental characterization technologies further articulate the adsorption and adsorption-capillary transition in nano-/meso-scale porous structures [136, 137, 170], including volumetric [171-175], gravimetric [176-179], and nuclear resonance [180]. Characterization methods include X-ray diffraction (XRD) [171, 173-175, 177], X-ray fluorescence spectroscopy (XRF) [179], positron annihilation spectroscopy [180], neutron scattering [172], and transmission electron microscopy (TEM) [178, 181]. Employing GCMC combined with high-resolution

volumetric adsorption measurements, Prasetyo et al. [182] have studied the krypton adsorption isotherm on a highly graphitized carbon black, showing that the hysteresis is observed for non-porous surfaces, which is associated with the continuous densification and ordering of the adsorbate on the adsorbent. He et al. [171] have studied the adsorption of pure ethane, pure carbon dioxide, and their binary mixture on MCM-41 using volumetric method and XRD characterization. Grosman and Ortega [172] have investigated the hysteresis of N<sub>2</sub> in ordered mesoporous silica SBA-15 using volumetric methods and neutron scattering, showing that the hysteresis is type H1 in cylindrical pores open at both ends and unlike generally assumed, the capillary evaporation does not take place at equilibrium. Morishige et al. [173] have employed volumetric methods and XRD to measure the effect of temperature on the adsorption isotherms of Ar, N<sub>2</sub>, O<sub>2</sub>, C<sub>2</sub>H<sub>4</sub>, and CO<sub>2</sub> on MCM-41 with pore radius sizes varying from 1.2 nm to 2.1 nm, showing that the dimensionless transition temperature increases linearly with dimensionless pore size. Morishige et al. [174] have used volumetric methods and XRD to show that Ar and CO<sub>2</sub> adsorption rather than desorption onto MCM-41 with a pore radius of 4.1 nm takes place near a thermodynamic equilibrium transition. Yun et al. [175] used a volumetric method and XRD to compare the experimental results of methane, ethane, and their binary mixture adsorption on MCM-41 with ideal adsorption solution theory and GCMC simulation expressing that both methods are accurate for the binary mixture investigation, but GCMC can also accurately predict the pure-components adsorption. Morishige et al. [176] gravimetrically measured water hysteresis on Ordered Mesoporous Carbons (OMC) with and without micropores, concluding that the uptake of water decreases by temperature drop just for the OMC without micropores. Qiao et al. [177] have studied the hexane adsorption on MCM-41 for temperatures and pore diameters varying from 303 K to 323 K and 2.40 nm to 4.24 nm, respectively, using XRD. They have shown that the adsorption isotherms are of type V and

the capillary transition pressure increases with the increase in temperature and pore size. Zandavi and Ward [178] have used gravimetric methods and TEM to consider the adsorption-desorption cycles of water, heptane, and octane on MCM-41 and SBA-14, showing that the contact angle is zero just before the pore-emptying. Using N<sub>2</sub> and Ar gas mixtures on Vycor glass, Alam et al. [180] have shown that the hysteresis cycle isotherm depends on the thermophysical state of the mixture surrounding the cylindrical mesopore.

However, the previous theoretical, numerical, and experimental studies primarily focus on the homogeneous nano-/meso-scale porous structures, i.e., uniform local structures. Although realistic nano-/mesoporous materials are often locally heterogeneous, i.e., locally non-uniform structures and materials, the roles of such local heterogeneities on the adsorption and capillary transition have not been systematically studied so far.

In this study, we examine the roles of the locally-heterogeneous structures on the adsorption and adsorption-capillary transition in Ar-filled Pt-based nanogaps with various solid-gas surface interactions with/without having one surface covered with nanoposts, using GCMC simulations. The adsorption and adsorption-capillary transition are predicted as a function of the gas pressure at given temperature and the surface temperature at given gas pressure. This study also examines the effects of the nanopost distance, height, surface interactions as well as the nanogap size on the adsorption and capillary transition. The hysteresis in nanogaps with or without nanoposts is also studied. The outcome of this study can be used to design capillary transition-based thermal switches as discussed in chapter 6.

## **4.2 Simulation method**

To understand the roles of heterogeneous materials and structures on the adsorption and capillary transition, a gas-filled nanogap having one surface with nanoposts is employed as shown

in Figure 4.1(a). The height of the nanogap,  $l_z$ , the width of the nanogap,  $l_x$  or  $l_y$ , and the nanopost pitch distance among the nanoposts,  $l_{p,x}$  or  $l_{p,y}$ , are given on one surface to examine the geometric effects on the adsorption and capillary transition (structural heterogeneity), while simulations with different gas-solid interatomic potentials are used to understand the effects of the surface interaction. The predicted results are compared with the nanogap with both bare surfaces as shown in Figure 4.1(b).

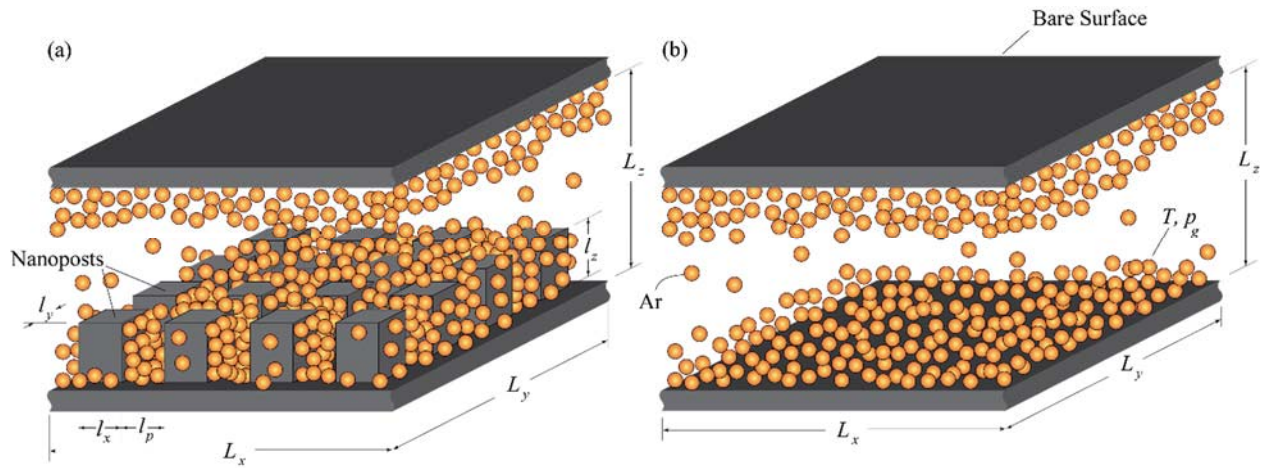


Figure 4.1. Schematic drawings of (a) nanogap with nanoposts on one surface and (b) nanogap with bare surfaces. The dimensions for the nanogap and nanoposts are also shown.

The adsorption and capillary transition is calculated as a function of temperature at given gas pressure, or gas pressure at given temperature, using GCMC simulations, i.e.,  $\mu$ VT simulations [183]. The nanogap sizes are  $L_z = 5$  and  $10$  nm with  $L_x = 8.864$  nm and  $L_y = 7.676$  nm. Periodic boundary conditions are used for the  $x$  and  $y$  directions, while non-periodic boundary condition is used for  $z$  direction. The system temperature including gas particles and solid surfaces is controlled during the simulation, using Nose-Hoover thermostat for the entire system [130, 131]. For the adsorption (filling) curve, 80 Ar atoms are initially distributed randomly in the nanogap, representing very low initial pressure ( $\sim 13$  kPa), and the number of Ar atoms increases to reach

the given chemical potential (or desired pressure at given temperature) [146]. The simulation stops where the number of Ar atoms do not change more than 1% over the last 100,000 atoms insertion/removal attempts, considering it as convergence. The number density,  $n_f$ , is calculated at convergence, while taking an average number density over the last 100,000 atoms insertion/removal attempts. For desorption (emptying curve), initially, the Ar atoms fully occupy the nanogap, representing the saturated pressure (saturated liquid), and the number of Ar atoms decrease, until it reaches the given chemical potential (desired pressure at given temperature). For adsorption isotherm, 86.8 K is chosen for the different pressure, and 1.66 atm is chosen for the different temperature. Nondimensional structural parameters,  $l_p^*$ ,  $l_z^*$ , and  $\varepsilon^*$  are used to examine the effects of the distance among nanoposts, heights, and the fluid-solid interatomic potentials on the adsorption isotherm for the specified temperature (90 K for the interaction effect and 86.8 K for the rest) or the pressure (1.66 atm), as given

$$l_p^* = \frac{l_p}{l_p + l_x} \quad (4.4) \quad l_z^* = \frac{l_z}{L_z} \quad (4.5) \quad \varepsilon^* = \frac{\varepsilon_{sf}}{\varepsilon_{sf, \text{Ar-Pt}}} \quad (4.6)$$

where  $l_p$  is the distance among the nanoposts, with nanopost dimensions of  $l_x = 1.108$ ,  $l_y = 0.960$  nm, and  $l_z$  varies from 1.15 nm to 4.05 nm. The same  $l_p^*$  are used for both  $x$ - and  $y$ -axes.

The interactions among Ar-Ar and Ar-solid particles are modeled by the Lennard-Jones potential given as

$$\varphi_{ij}(r) = 4\varepsilon_{ij} \left[ \left( \frac{\sigma_{ij}}{r_{ij}} \right)^{12} - \left( \frac{\sigma_{ij}}{r_{ij}} \right)^6 \right], \quad r_{ij} < r_{cut-off}, \quad (4.7)$$

where  $\varepsilon_{ff} = 0.2403$  kcal/mol for Ar-Ar [133],  $\varepsilon_{sf} = 0.1573$  kcal/mol for Ar-Pt,  $r_{cut-off} = 1.2$  nm [184], and  $\sigma_{\text{Ar-Ar}} = 3.405$  Å and  $\sigma_{\text{Pt-Pt}} = 2.5346$  Å [118]. The Pt-Pt particle interactions are modeled by harmonic potential given as

$$\varphi_{ij}(r_{ij}) = \frac{1}{2}\Gamma(r_{ij} - r_o)^2, \quad (4.8)$$

where  $\Gamma = 67.360 \text{ kcal/mol-}\text{\AA}^2$  and  $r_o = 2.77 \text{ \AA}$  [133]. To run the GCMC simulations, the Large-scale Atomic/Molecular Massively Parallel Simulator (LAMMPS) is used [134, 185].

For the number density of Ar, the nanogap volume calculation is crucial, but it is challenging to calculate the accurate, effective volume due to the occupying spaces near the solid surfaces (repulsion forces). Here, for the volume of nanogap with bare surfaces, we used  $L_z = 5$  or  $10 \text{ nm}$ , whereas for the volume of nanogap with nanoposts, we subtract the volume of nanoposts from the nanogap volume. The calculated number density from GCMC agrees to Ar number density for bulk liquid,  $n_f = 21.086 \text{ nm}^{-3}$  [186] which is used for volume calculation validation.

The uncertainty of the number density calculations is estimated based on three separate simulations with different initial conditions near the capillary transition, and the maximum standard error is 0.15. The error bars are too small to be shown in the figures.

### 4.3 Simulation validation

To validate the simulation approaches, we calculated the adsorption isotherm at  $L_z = 5 \text{ nm}$  with both bare surfaces, at  $T = 87 \text{ K}$ , as a function of the relative gas pressure, i.e., normalized gas pressures by saturated pressure at given temperatures. The predicted results are compared to the available experimental results for the adsorption isotherm of Ar on MCM-41 at  $T = 87 \text{ K}$ , including the adsorption-capillary transition [187]. In fact, the adsorbents used in the prediction and experiment are different, although the adsorbate, i.e., Ar, is the same, and the nanostructure sizes, i.e., nanogap with  $L_z = 5 \text{ nm}$  and nanotube with  $d_p = 5.1 \text{ nm}$ , are similar. However, the experimental study for Ar-MCM-41 is chosen for the validation, since there is no better alternative in literature. In experiment, the adsorption isotherm has been originally reported as  $\text{cm}^3 \text{ STP g}^{-1}$ , but here, it is equivalently translated into the number density for the comparison with the GCMC simulation. In

the experiment, the adsorption isotherm increases as the relative pressure increases, and it completely fills the pores above the transition pressure. The predicted adsorption isotherm underestimates the experimental results, since the gas-solid interaction in the simulation (Ar-Pt) is lower than one used in experiment (Ar-MCM-41). However, as the adsorbed layers thicken, the gas-solid interaction becomes less important, since the thick adsorbed layers serve as the solid surface (adsorbent). Thus, the capillary transition pressure becomes independent of the adsorbent material [188, 189]. The GCMC simulation predicts the measured capillary transition at  $p^*_{tr} = 0.55$ , which reasonably validates the simulation.

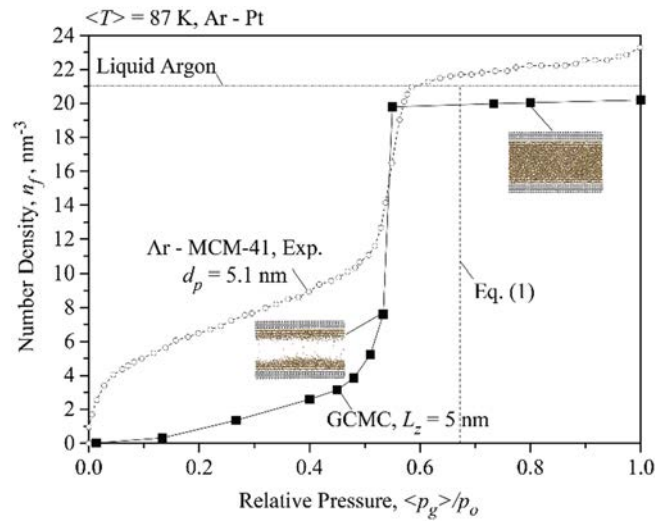


Figure 4.2. Comparison of the predicted adsorption isotherm of Ar in a Pt-based nanogap,  $L_z = 5$  nm, at  $T = 87$  K using GCMC with the measured one for Ar in a MCM-41 with a 5.1 nm pore diameter [187].

In fact, the modified Kelvin equation [Eq. (4.1)], does not agree GCMC simulation and experimental results, due to the lack of the gas-solid interaction and oversimplified assumption (adsorbed layer is considered as bulk liquid) in Eq. (4.1) [138].

## 4.4 Results and discussion

### 4.4.1 Nanopost pitch distance ( $l_p^*$ ) effect

Figure 4.3(a) shows the number density of Ar particles at  $T = 86.8$  K as a function of relative pressure. In the nanogap with bare surfaces,  $L_z = 5$  nm and  $l_p^* = 1$ , the Ar particles begin to form adsorbed layers near the solid surfaces, and Ar number density increases gradually by increasing gas pressure up to  $\langle p_g \rangle / p_o = 0.55$ . At this pressure, the capillary transition occurs and Ar particles fill the entire nanogap. By further increasing the gas pressure, the number density does not significantly change due to liquid incompressibility. With the nanoposts having the height of  $l_z^* = 0.63$  and the nanopost pitch distance of  $l_p^* = 0.67$ , the adsorption increases at low gas pressure and the capillary transition pressure decreases compared to the bare surfaces,  $l_z^* = 0$  and  $l_p^* = 1$ . These changes are primarily caused by the increased, effective gas-solid interactions in presence of the nanoposts, i.e., the increased surface forces due to the overlapping surface forces across the nanopost gaps. In addition, the adsorption-capillary transition occurs in two steps, so called bimodal transition; the first transition,  $\langle p_g \rangle / p_o = 0.4$ , occurs due to the filling of the gap among the nanoposts, and the second transition,  $\langle p_g \rangle / p_o = 0.5$ , results from the filling of the entire nanogap. As the pitch distance decreases, i.e.,  $l_p^* = 0.5$ , the Ar number density further increases and the bimodal transition becomes more pronounced with the increased pressure difference between the two transition pressures. The difference between the two transition pressures increases as the distance among the nanoposts decreases i.e.,  $l_p^* = 0.33$ , with the second capillary transition pressure of  $\langle p_g \rangle / p_o = 0.39$ . In fact, the height of nanoposts,  $l_z^* = 0.63$ , would be expected to effectively reduce the gas space in nanogap, i.e.,  $L_z = 2$  nm. Note that the results for  $L_z = 2$  nm with the bare surfaces show only a single step capillary transition, at  $\langle p_g \rangle / p_o = 0.26$  with relatively lower adsorption, compared to the nanogap with one surface having nanoposts at similar gas space.

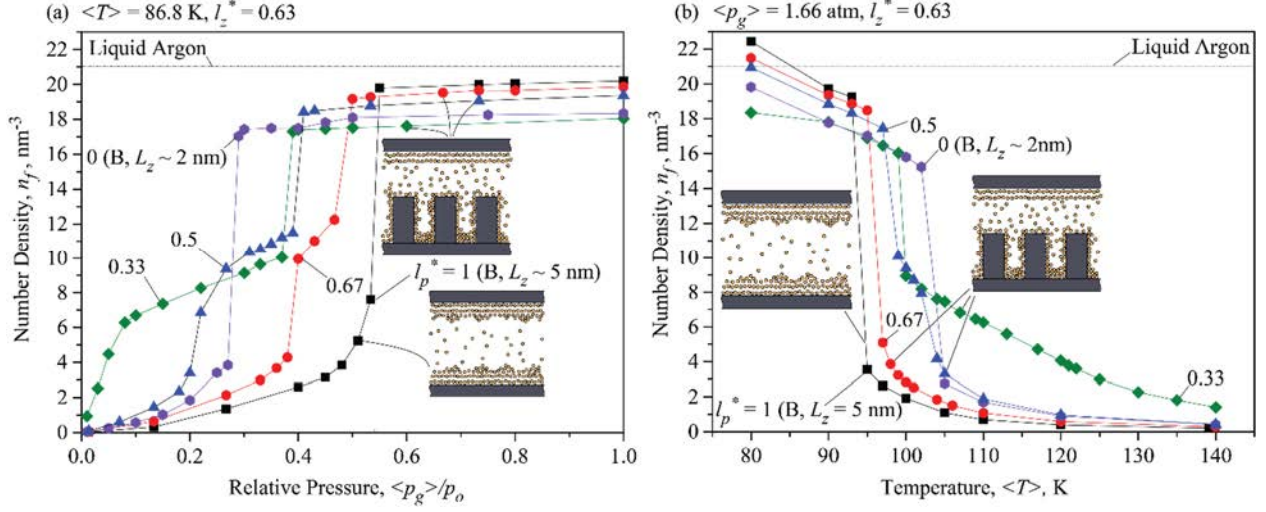


Figure 4.3. Variation of Ar number density,  $n_f$ , for  $l_z^* = 0.63$ ,  $\varepsilon^* = 1.0$ , and  $l_p^* = 0$  (bare surface with  $L_z \sim 2$  nm),  $0.33$ ,  $0.5$ ,  $0.67$ , and  $1.0$  (bare surface with  $L_z \sim 5$  nm); a) as a function of relative pressure,  $\langle p_g \rangle / p_o$ , at  $\langle T \rangle = 86.8$  K; b) as a function of temperature,  $\langle T \rangle = 80$  to  $140$  K in  $\langle p_g \rangle = 1.66$  atm. The insets correspond to the nanogaps with bare surfaces and one surface with nanoposts. (B) represents the bare surface. Error bars are too small to be observed.

This difference is caused by the fact that the capillary filling among the nanoposts increases the adsorption in the low pressure and the nanopost structures (nanoscale surface roughness) increases the capillary transition pressure.

Figure 4.3(b) shows the transition for the same structures in constant pressure ( $p_g = 1.66$  atm). Increasing temperature decreases Argon number density gradually. At  $T = 95$  K, the nanogap is emptied as a result of capillary transition, and Ar number density continues to gradually decrease to a very small number density at  $T = 140$  K. Including nanoposts decreases the rate of Ar number density change before the capillary transition and with decreasing  $l_p^*$  the transition happens at temperatures as high as  $100$  K. No bimodal transition is found for  $l_p^* = 0.67$ , while it is observed for  $l_p^* = 0.5$ . There is also an increase in Ar number density after the capillary transition. For the nanoposts with  $l_p^* = 0.33$ , the number density difference before and after the capillary transition is comparatively small and number density remains as high as  $4$  at  $T \sim 120$  K. For temperatures higher than  $140$  K (close to  $T_{cr} = 150.1$  K), there is just gaseous state and as a result the values of

$n_f$  are small. The simulations for a bare nanogap with  $L_z = 2$  nm are also shown in Figure 4.3(a) and (b) as a reference. The simulations generating the points before and after the capillary transition shown in Figure 4.3(a) and (b) are each repeated three times with different initial conditions and the error bars are so small that they do not appear in the Figures.

#### 4.4.2 Nanopost height ( $l_z^*$ ) effect

Figure 4.4(a) shows the number density of Ar particles at  $T = 86.8$  K as a function of relative pressure,  $0 < \langle p_g \rangle / p_o < 1$  at given nanopost heights,  $l_z^* = 0, 0.23, 0.41, 0.63,$  and  $0.81$ , and pitch distance,  $l_p^* = 0.5$ . A small nanopost height,  $l_z^* = 0.23$ , considerably increases Ar number density below the capillary transition, compared to the bare surfaces, but it does not significantly change the capillary transition pressure,  $p_{tr}^* \sim 0.55$ . A larger height,  $l_z^* = 0.41$ , results in a higher number density below the capillary transition and a bimodal transition due to the smaller effective gas space among nanoposts and larger effective gas space across the nanogap. However, it does not significantly change the capillary transition pressure. Increasing the nanoposts height to  $l_z^* = 0.63$ , results in an apparent bimodal transition, starting at  $\langle p_g \rangle / p_o = 0.22$  and it also decreases the bimodal capillary transition pressure to  $p_{tr}^* = 0.41$ . Eventually, a large height,  $l_z^* = 0.81$ , causes a sharp increase in Ar number density, and a single-mode capillary transition in a small relative pressure, i.e.,  $p_{tr}^* \sim 0.2$ . The simulation results for the bare surfaces with  $L_z = 1$  nm is shown in Figure 4.4(a) to compare with the results of  $l_z^* = 0.81$ , since those have the same effective gas space. Apparently, the results of  $l_z^* = 0.81$  are significantly different from bare surfaces with  $L_z = 1$  nm, showing smaller adsorption in low gas pressure and a higher capillary transition pressure,  $p_{tr}^* \sim 0.2$ , compared to the bare surfaces. This is related to the fact that the smaller nanogap size,  $L_z = 1$  nm, with the bare surfaces provides a stronger surface force overlap across the nanogap than the one surface having nanoposts (nano surface roughness) at similar gas space. For all the

nanopost heights, the Ar number density approaches to the number density of liquid Ar,  $n_f = 21.1 \text{ nm}^{-3}$ , at pressures above the capillary transition, representing the complete fillings of the nanogaps. Similar results are observed, when the temperature changes in a given gas pressure,  $\langle p_g \rangle$  as shown in Figure 4.4(b).

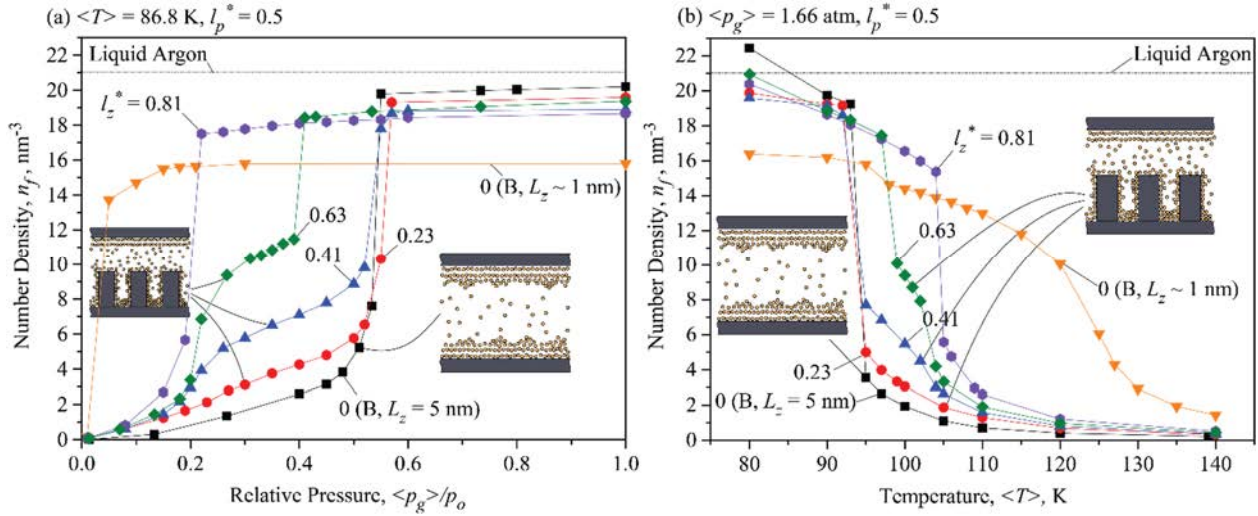


Figure 4.4. Variation of the Ar number density,  $n_f$ , for  $l_p^* = 0.5$ ,  $\varepsilon^* = 1.0$ , and  $l_z^* = 0$  (bare surface with  $L_z = 5 \text{ nm}$ ), 0.23, 0.41, 0.63, 0.81, and bare surface with  $L_z \sim 1 \text{ nm}$ ; a) as a function of the relative pressure,  $\langle p_g \rangle / p_o$ , at  $\langle T \rangle = 86.8 \text{ K}$ ; b) as a function of the temperature,  $\langle T \rangle = 80 \text{ to } 140 \text{ K}$  in  $\langle p_g \rangle = 1.66 \text{ atm}$ . The insets correspond to the nanogaps with bare surfaces and one surface with nanoposts. (B) represents the bare surface. Error bars are too small to be observed.

A small nanopost height,  $l_z^* = 0.23$ , slightly increases Ar number density before capillary transition but it does not significantly change the capillary transition temperature,  $T_{tr} \sim 95 \text{ K}$ . A larger height,  $l_z^* = 0.41$ , does not change the capillary transition temperature, but it results in a bimodal transition with a transition temperature difference of  $\Delta T_{tr} \sim 10 \text{ K}$ . Increasing the nanoposts height to  $l_z^* = 0.63$  results in an apparent bimodal transition starting at  $T_{tr} = 99 \text{ K}$ . Eventually, a large height,  $l_z^* = 0.81$ , causes a sharp decrease in the Ar number density, and a single-mode capillary transition at a higher transition temperature, i.e.,  $T_{tr} \sim 105 \text{ K}$ . Near the critical temperature, the adsorbed Ar number density is very small, since it becomes non-condensable gas. The results of  $l_z^* = 0.81$  are significantly different from bare surfaces with  $L_z = 1 \text{ nm}$ , showing a

lower capillary transition temperature,  $T_{tr} \sim 105$  K. This represents the nanoposts allow for early emptying (evaporation) process at the similar gas space. The uncertainty analysis is done repeating each simulation in the transition area for three times but the standard errors are smaller than the symbols in Figure 4.4(a) and (b).

#### 4.4.3 Surface interaction ( $\epsilon^*$ ) effect

Figure 4.5(a) shows the predicted adsorption isotherm for the nanogaps with bare surfaces and one surface having nanoposts with pitch distance of  $l_p^* = 0.5$  and height  $l_z^* = 0.81$  at given gas-solid interatomic potentials,  $\epsilon^* = 0.5, 1, \text{ and } 2$ . For the bare surfaces, the reduced interatomic potential,  $\epsilon^* = 0.5$ , results in a significant increase in capillary transition pressure,  $p_{tr}^* \sim 1.3$ , and a significant decrease in adsorption isotherm below  $p_{tr}^*$ , compared to  $\epsilon^* = 1.0$ . However, the increased interatomic potential,  $\epsilon^* = 2$ , allows for the capillary transition similar to  $\epsilon^* = 1.0$ ,  $p_{tr}^* \sim 0.55$ , while the adsorption isotherm increases below the capillary transition pressure due to the stronger gas-solid interaction. For the reduced gas-solid interaction,  $\epsilon^* = 0.5$ , the nanoposts decrease the capillary transition pressure from  $p_{tr}^* \sim 1.3$  to  $\sim 0.9$  without changing adsorption isotherm below the capillary transition pressure, while for  $\epsilon^* = 2.0$ , they reduce  $p_{tr}^*$  from  $\sim 0.55$  to  $0.05$ . No significant increase in Ar number density is observed for pressures above the capillary transition pressure.

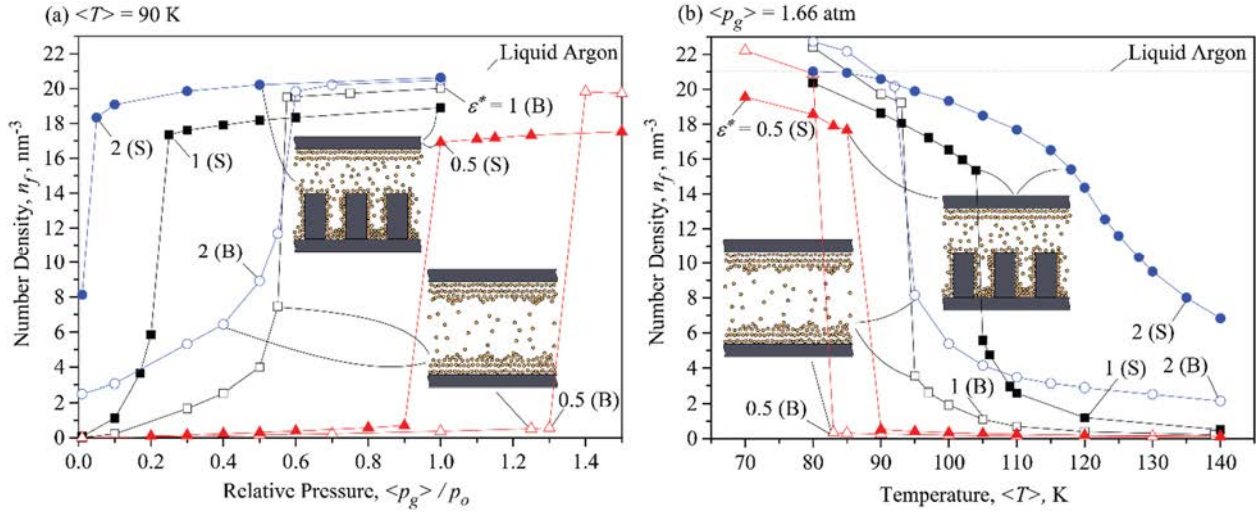


Figure 4.5. Variations of Ar number density,  $n_f$ , for nanogaps with bare surfaces and one surface having nanoposts ( $l_p^* = 0.5$  and  $l_z^* = 0.81$ ) at gas-solid interactions,  $\epsilon^* = 0.5, 1.0$ , and  $2.0$ ; a) as a function of the relative pressure,  $\langle p_g \rangle / p_o$ , at  $\langle T \rangle = 90$  K; b) as a function of the temperature,  $\langle T \rangle = 70$  to  $140$  K in  $\langle p_g \rangle = 1.66$  atm. The insets correspond to the nanogaps with bare surfaces and one surface with nanoposts. (S) represents the one surface having nanoposts and (B) represents the bare surface. Error bars are too small to be observed.

Figure 4.5(b) shows the simulation results as a function of the surface temperature,  $80 < \langle T \rangle < 140$  K, at given gas pressure,  $1.66$  atm. For the bare surfaces, the reduced gas-solid interaction,  $\epsilon^* = 0.5$ , leads to the capillary transition temperature reduction from  $T_{tr} = 95$  to  $82$  K, without changing the adsorption isobar above the capillary transition temperature. The increased gas-solid interaction,  $\epsilon^* = 2.0$ , shows the similar capillary transition temperature compared to  $\epsilon^* = 1.0$ , but with a significant increase in adsorption isobar above the capillary transition temperature. For  $\epsilon^* = 0.5$ , the nanoposts increase the capillary transition temperature from  $T_{tr} = 82$  K to  $90$  K without changing the adsorption isotherm above the capillary transition temperature, while for  $\epsilon^* = 2$ , the capillary transition temperature significantly increases,  $T_{tr} \sim 125$  K, with a smooth transition and Ar number density is as large as  $7 \text{ nm}^{-3}$  for  $T_{tr} = 140$  K. The uncertainty analysis is performed by repeating three simulations with different initial conditions at the capillary transition state, but the standard errors are too small to be found in Figure 4.5(a) and (b).

#### 4.4.4 Nanogap size ( $L_z$ ) effect

Figure 4.6(a) shows the predicted adsorption isotherm in the nanogaps with bare surfaces with nanogap sizes of  $L_z = 5$  nm and 10 nm, as a function of relative pressure at given temperature,  $\langle T \rangle = 86.8$  K. These results are also compared with the ones with one surface having nanoposts with pitch distance and height of  $l_p^* = 0.5$  and  $l_z^* = 0.63$ , respectively.

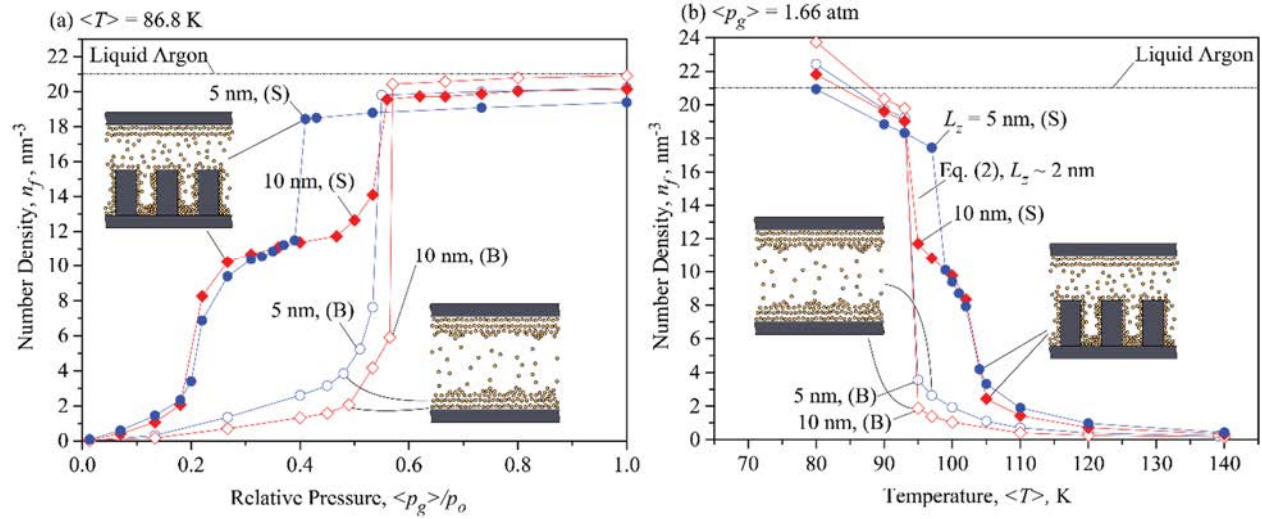


Figure 4.6. Predicted Ar number density,  $n_f$ , in nanogaps with bare surfaces and one surface having nanoposts ( $l_p^* = 0.5$  and  $l_z^* = 0.63$ ); a) as a function of the relative pressure,  $\langle p_g \rangle / p_o$ , at  $\langle T \rangle = 86.8$  K; b) as a function of the temperature,  $\langle T \rangle = 70$  to 140 K in  $\langle p_g \rangle = 1.66$  atm. The insets correspond to the nanogaps with bare surfaces and one surface with nanoposts. (S) represents the nanogap with nanoposts on one surface, and (B) represents the bare surface. Error bars are too small to be observed.

For the bare surfaces, the capillary transition pressures are similar,  $p_{tr}^* = 0.55$  and  $0.57$ , respectively for the small and large nanogaps. Below the capillary transition pressures, the adsorption isotherm in the smaller nanogap,  $L_z = 5$  nm, is larger than  $L_z = 10$  nm, due to the overlapping surface force across the nanogap. However, the presence of the nanoposts significantly increases the adsorption in low pressures including bimodal capillary transitions for both nanogap sizes, compared to the bare surfaces. The number densities in adsorption are similar in both nanogap sizes, but for the larger nanogap size,  $L_z = 10$  nm, the second capillary transition

occurs at a higher relative pressure,  $\langle p_g \rangle / p_o = 0.56$ , compared to that of smaller nanogap size,  $L_z = 5$  nm,  $\langle p_g \rangle / p_o = 0.41$ . This increased capillary transition pressure is caused by the larger effective nanogap size (larger gas space excluding nanoposts,  $\sim 4$  nm) for  $L_z = 10$  nm, compared to  $\sim 2$  nm for  $L_z = 5$  nm, i.e., the smaller effective nanogap size results in early capillary transition, Eq. (4.1).

Figure 4.6(b) shows the predicted adsorption as a function of nanogap surface temperature,  $80 < T > < 140$  K, at given gas pressure,  $\langle p_g \rangle = 1.66$  atm, both for nanogaps with bare surfaces and one surface having nanoposts. For the bare surfaces, the adsorption is similar below the capillary transition temperature,  $T_{tr} \sim 95$  K for both nanogap sizes, while for  $L_z = 5$  nm, a larger adsorption is predicted above the transition temperature, due to the overlapping surface force across the nanogap. With the nanoposts on one surface, both nanogap sizes show similar results except the first capillary transition temperature for  $L_z = 10$  nm decreases to 95 K compared to 99 K for  $L_z = 5$  nm, since it requires a lower temperature for larger effective nanogap size ( $\sim 4$  nm). Ar number density above the capillary transition temperature is slightly larger for the smaller nanogap size, and this difference disappears with a further increase in temperature (close to the critical temperature,  $T_c = 151$  K). The error bars are calculated using three separate simulation results with different initial conditions, which are too small to be observed.

#### 4.4.5 Hysteresis

Figure 4.7(a) reveals a hysteresis for adsorption in the Ar-filled Pt-based nanogaps at given temperature  $\langle T \rangle = 86.8$  K. For bare surfaces, the capillary transition pressure in desorption occurs at  $p_{tr}^* = 0.15$ , which is considerably smaller than that in adsorption,  $p_{tr}^* = 0.55$ , having only one capillary transition for each. With nanoposts on one surface having  $l_p^* = 0.5$  and  $l_z^* = 0.63$ , only one capillary transition is predicted at  $p_{tr}^* = 0.2$  in desorption, whereas the bimodal adsorption capillary transition is observed at  $p_{tr}^* = 0.22$  and 0.4. Note that only one capillary transition in the

desorption represents a single step evaporation, whereas the bimodal capillary transition in the adsorption means two-step condensations, i.e., the first condensation is caused by filling the space between the nanoposts and the second one results from fillings of the nanogap. The capillary transition pressure in desorption is similar to the first transition pressure in the adsorption. Here, as well the number densities from the GCMC simulations before capillary evaporation and after the second jump in adsorption isotherm are equal in adsorption and desorption isotherms. Similarly, the hysteresis is observed at given gas pressure as a function of temperature,  $\langle p_g \rangle = 1.66$  atm, as shown in Figure 4.7(b). For the bare surfaces, the capillary transition in desorption occurs at a higher temperature,  $T_{tr} = 104$  K compared to the adsorption,  $T_{tr} = 95$  K. Note that for the bare surfaces, both the adsorption and desorption capillary transition processes are single step. However, with the nanoposts, a bimodal transition occurs in the adsorption, whereas only a single step capillary transition occurs in desorption. The capillary evaporation temperature is similar to the temperature related to the second transition temperature,  $T_{tr} = 105$  K. Note that only one capillary transition temperature in the desorption means a single step evaporation, whereas the bimodal capillary transition temperatures in the adsorption represent the two-step condensations, i.e., the first condensation is caused by filling the nanoposts and the second one results from the filling of the nanogap. The predicted number densities are average values of three individual simulations with different initial conditions before and after the capillary transition pressure or temperature, but the error bars are too small to be found in Figure 4.7(a) and (b).

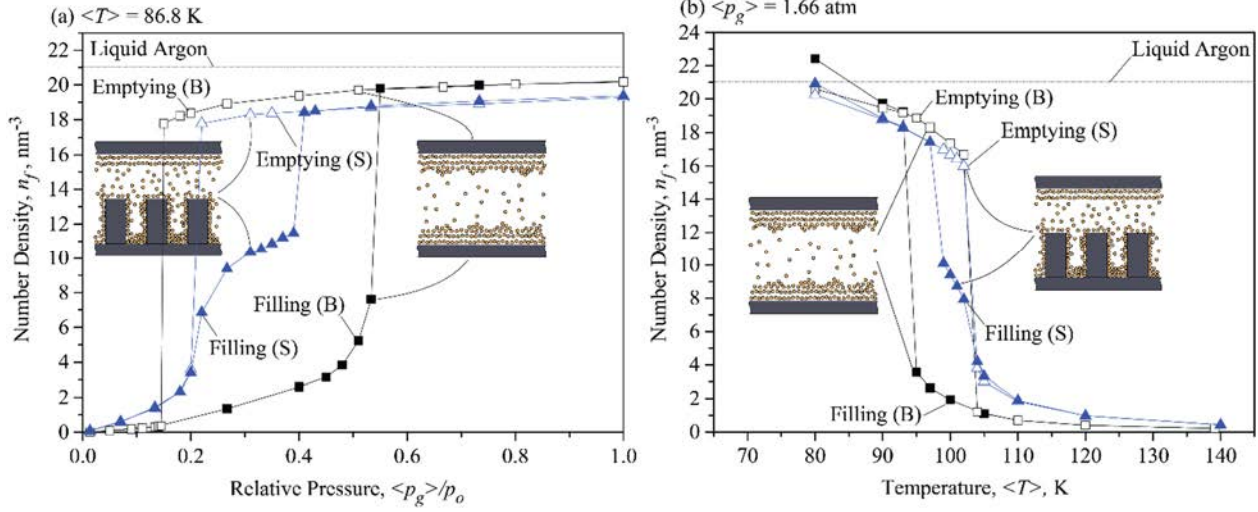


Figure 4.7. Hysteresis in nanogaps with bare surfaces and one surface with nanoposts ( $l_p^* = 0.5$  and  $l_z^* = 0.63$ ); a) as a function of the relative pressure,  $\langle p_g \rangle / p_o$ , at  $\langle T \rangle = 86.8\text{ K}$ ; b) as a function of the temperature,  $\langle T \rangle = 70$  to  $140\text{ K}$  at  $\langle p_g \rangle = 1.66\text{ atm}$ . The insets for the nanogaps with bare surfaces and one surface with nanoposts are also shown. (S) represents the one surface with nanoposts, and (B) represents the bare surface. Error bars are too small to be observed.

#### 4.5 Conclusion

In this chapter, the adsorption and adsorption-capillary transition for Ar-filled Pt-based nanogaps having one surface with nanoposts, are examined using the GCMC simulations. Results show that the adsorption-capillary transition pressure decreases at given temperature (or the transition temperature increases at given pressure), by increasing the nanopost height,  $l_z$ , decreasing the nanopost gap size,  $l_p$ , and increasing the solid-fluid interatomic potential,  $\varepsilon_{sf}$ . The bimodal adsorption-capillary transition is also observed, and this is more pronounced when the two characteristic sizes are similar, i.e., one for the nanoposts at lower gas pressure and the other for the nanogap at higher gas pressure. Also, it is observed that as the distance between the nanoposts decreases, the difference between the bimodal capillary transition pressures become larger, especially at lower relative pressures. The small nanoposts ( $l_z^* < 0.4$ ) do not change the capillary transition pressure,  $p_{tr}^*$ , but they increase the adsorption, due to the increased effective surface force below  $p_{tr}^*$ . The bimodal capillary transition is also observed in presence of the

nanoposts with moderate heights ( $0.4 < l_z^* < 0.8$ ), which reduce the second capillary transition pressure. For large nanoposts, only one capillary transition occurs at a very low relative gas pressure,  $\langle p_g \rangle / p_o < 0.05$ , since it significantly reduces the effective nanogap size. It is also observed that the stronger gas-solid interaction effectively reduces the capillary transition pressure and increases the adsorption isotherm with the inclusion of nanoposts. For the bare surfaces, the doubled nanogap size shows no apparent size-effect, whereas for the nanogaps with nanoposts, the second capillary transition pressure increases. The nanoposts reduce the hysteresis compared to the bare surfaces, and they show no apparent bimodal capillary transition in the desorption curve. The difference found between the adsorption isotherm in nanogaps with both bare surfaces and one surface with nanopost can be used to design thermal switches with high degrees of thermal switching,  $S$ . This will be discussed in chapter 6.

## CHAPTER 5

### CAPILLARY-CONTROLLED THERMAL DIODE IN HETEROGENEOUS NANOSTRUCTURES<sup>1</sup>

#### 5.1 Introduction

A thermal diode is a key component to substantially improve the operating energy efficiency in waste heat recovery [3-5], smart building [6] systems, and even open brand new applications including thermal logic gates and computers [7-11]. The thermal diode (rectifier) allows for an asymmetric heat flux, i.e., favorable heat flux in only one direction of the temperature gradient.

Various diode designs have employed nonlinear heat transfer characteristics, both experimentally and theoretically, and detailed literature review is available in recent studies [10, 12, 111]. Thermal diode has been predominantly explored in nonlinear thermal conduction mechanisms, as the first thermal diode mechanism has been demonstrated in the asymmetric thermal conductivity through Cu/CuO interface [14]. The nonlinear conduction-based thermal diodes have employed the asymmetric phononic thermal transport through heterogeneous solid-solid junctions [5, 18-22, 35, 190, 191], heterogeneous solid-liquid junctions [23-25], heterogeneity in asymmetric geometries [8, 9, 26-41, 43-49, 192], heterogeneity with asymmetric mass distribution [34, 57, 193, 194] without the external energy control. The thermal diode has also been explored with the assistance from the external energy controlling [58-64]. Asymmetric free electron thermal transport across heterogeneous interfaces has been also explored and thermal

---

<sup>1</sup> This entire chapter has been submitted for publication to the following source:

- Avanesian, T. and Hwang, G., *Thermal diode using controlled capillary in heterogeneous nanopores*. International Journal of Heat and Mass Transfer, Submitted November 2017.

diodicity is demonstrated due to tailored electron transport through conducting/insulating materials (macroscale) or in quantum state (atomic-scale) [15-17]. Other conduction-based designs include electrochemically tuned thermal conductivity change during delithiation of  $\text{LiCoO}_2$  [82], shape memory alloy-based passive solid state diode [195], and liquid-state thermal expansion-based thermal diode [196]. A thermal diode has been also achieved through the asymmetric liquid-solid or gas-solid thermal conductivity near the rough surface [197].

The thermal diode has been also achieved by capillary-assisted nonlinear heat transfer in heat pipes [66, 67], heterogeneous water wetting using hydrophobic and hydrophilic surfaces [68, 69], or gravity-driven asymmetric natural convection between solid plates [12, 65]. The primary working principle is to utilize the asymmetric thermofluid transport, which in turn allows for the efficient thermal diodicity. However, those have been demonstrated at macro-scale system.

The nonlinear radiation-based thermal diode has utilized photon transport in tailored micro/nanostructures using temperature-dependent optical resonance [70, 75], dielectric coating [71], different doping concentration [72, 76], phase-change radiation [73, 74], blackbody sandwiched by plates with different emissivities [12, 77], or by near-field nanothermomechanical rectification [198].

Several studies have demonstrated the thermal diode effect in quantum (atomic-scale) systems such as heterogeneous junctions [50], nonlinear electron-gas-dispersion relation transport [51, 52], quantum dot structure [4, 53, 54], or nonlinear quantum circuits [55]. Despite interesting scientific phenomena and approaches, the thermal diode effect in quantum systems primarily remains in theoretical approaches.

Although various theoretical approaches have been explored for the thermal diode, the thermal diode efficiency in the experiments remains poor, especially at nano-/microscale [8, 11, 14, 30,

82, 198], primarily due to challenging manufacturing and expensive operations [8, 12, 87, 95, 110]. Indeed, the efficient thermal diode has been experimentally demonstrated in nonlinear convection mechanisms [12, 65-69, 199, 200], but it requires bulky system, which limits the system mobility and leads to slow transient response. Also, the radiation-based thermal diodes require very high operating temperatures, which may limit the practical applications.

To overcome aforementioned challenges, a new class of thermal diode is examined by employing a larger thermal conductivity contrast between gas (adsorption) and liquid (capillary) states in heterogeneous nanopores, so called capillary-controlled thermal diode. The effects of the structural/material heterogeneity on the thermal diode have been explored using Ar-filled Pt-based nanogap and Grand Canonical Monte Carlo (GCMC) simulation combined with Non-Equilibrium Molecular Dynamics (NEMD) simulation.

## **5.2 Working principle**

The key working principle of the capillary-controlled-based thermal diode is to employ the large contrast in thermal conductivity between the gas (adsorption) and liquid (capillary) states in nanopores. In fact, the capillary transition inherently brings hysteresis for the capillary condensation/evaporation under the cyclic operations [138, 139], which in turn results in poor controllability in the thermal diode operation. To improve the operational controllability, the structural heterogeneity, i.e., nanopillars on one surface only is employed as shown in Figure 5.1. Ar particles fill the nanogap with the size  $L_z$  as a thermal energy carrier between the surfaces and Ar physical state, i.e., adsorption or capillary, regulates the heat flux magnitude. The adsorption and capillary states are related to the surface temperature, gas pressure, and nanogap size [138, 139]. Here the upper surface temperature,  $T_2$ , is controlled, while the lower surface temperature,  $T_1$ , remains the same during the operation. For the adsorption-capillary transition, the upper surface

temperature,  $T_2$ , operates above and below the capillary transition temperature,  $T_{tr}$ , at given gas pressure,  $p_g$ , and nanogap size,  $L_z$ , whereas the bottom temperature is maintained above the capillary transition temperature but below the critical temperature,  $T_c$ , i.e.,  $T_{tr} < T_1 < T_c$ .

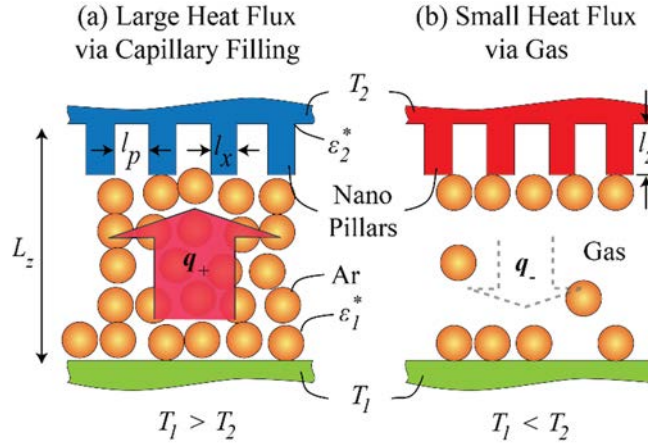


Figure 5.1. Schematic of capillary-controlled thermal diode using Ar-filled Pt-based heterogeneous nanogap (a)  $q_+ \gg 0$  for  $T_1 > T_2$  due to the high thermal conductivity of liquid-like (capillary) state, and (b)  $q_- \sim 0$  for  $T_1 < T_2$  due to the low thermal conductivity of gas (adsorption) state. The surface temperatures,  $T_1$  and  $T_2$ , heat fluxes,  $q_+$ , and  $q_-$ , dimensionless fluid-solid interactions,  $\epsilon_1^*$  and  $\epsilon_2^*$ , nanogap and nanopillar size parameters,  $L_z$ ,  $l_p$ ,  $l_x$ ,  $l_z$ , and Ar particles are also shown.

Note that the nanopillars considerably increase the surface interacting with Ar particles and the temperature of the surface having the nanopillars dominantly controls the average gas temperature inside the nanogap. If the upper surface temperature is lower than the transition temperature and the lower surface, i.e.,  $T_2 < T_{tr} < T_1$ , such a low temperature results in capillary transition (liquid-like) even though the bottom surface,  $T_1$ , is above the capillary transition temperature,  $T_{tr}$ , and this in turn leads to the high thermal conductivity and consequently high heat flux in upward direction,  $q_+ \gg 0$  for  $T_1 > T_2$ , as shown in Figure 5.1(a). On the other hand, the upper surface temperature higher than both the lower surface temperature and the transition temperature, i.e.,  $T_2 > T_1 > T_{tr}$ , maintain Ar in adsorption state (gas), and the low thermal conductivity of gas leads to poor downward heat flux,  $q_- \sim 0$ , as shown in Figure 5.1(b). The larger contrast of Ar thermal

conductivity between the gas (adsorption) and liquid (capillary) at different temperature gradient direction leads to the capillary-controlled thermal diode.

The Ar-filled Pt-based heterogeneous nanostructure is chosen because of the reasonable interatomic potentials and small computational cost (monatomic gas). However, the key approach is to utilize the capillary-controlled thermal conductivity change across heterogeneous nanopores for the thermal diode, and this principle can be extended to any condensable fluid operating between the melting and critical temperatures at a given pressure.

### 5.3 Simulation method

To demonstrate the aforementioned working principle, the GCMC simulations combined with NEMD simulations are employed where the nanogap dimensions are  $L_x = 8.864$  nm,  $L_y = 7.676$  nm, and  $L_z = 5$  or 10 nm. Periodic boundary conditions are used for the  $x$ - and  $y$ - axes, while the fixed non-periodic boundary is used for  $z$ -axis. Each surface of the bare nanogap consists of three layers of Face Centered Cubic (FCC, 111 plane) Pt-based solid. One fixed layer is added as the outermost layer to the upper and lower surfaces to fix the nanogap during the simulation. For the structured surface, the nanopillars are added to the innermost solid layer of the upper surface with the same FCC pattern having uniform height and space among the columns. The simulations are run independently for each characteristic nanopillar height. The simulations are performed in two steps. Firstly, GCMC simulation is used [183] to determine the number of Ar particles for desired pressure in the nanogap with/without nanopillars. Secondly, the subsequent NVT simulation is run using the determined number density from GCMC for the desired pressure. For MD, the velocity-Verlet algorithm is used for the time integration over the time step of 2 fs [129] and the equilibrium state is achieved by simulating it for 6 ns using Nose-Hoover thermostat at average nanogap temperature  $T_{ave}$  for the entire system [130, 131]. Then, the temperature gradient is created by

imposing the upper/lower surface temperatures using Langevin thermostat [132] for 14 ns, while the kinetic energy (temperature) of the solid atoms is maintained using the random force input to control the temperature relaxation. Depending on the direction of temperature gradient, calculated heat flux is used as  $q_+$  or  $q_-$  in Eq. (1.2). To run the GCMC and NEMD simulations, the Large-scale Atomic/Molecular Massively Parallel Simulator (LAMMPS) was used [134, 135]. Lennard-Jones potential between Ar-Ar and Ar-solid particles is used, given as

$$\varphi_{ij}(r) = 4\varepsilon_{ij} \left[ \left( \frac{\sigma}{r_{ij}} \right)^{12} - \left( \frac{\sigma}{r_{ij}} \right)^6 \right], \quad r_{ij} < r_{cut-off}, \quad (5.1)$$

where  $\varepsilon_{ff} = 0.2403$  kcal/mol for Ar-Ar [133],  $\varepsilon_{sf} = 0.1573$  kcal/mol for Ar-Pt with  $r_{cut-off} = 1.2$  nm [117], and  $\sigma$  indicates the distance for which no repulsive or attractive potential exists between particles. For Ar-Ar interaction  $\sigma_{Ar-Ar} = 3.405$  Å and for Ar-Pt interaction the geometric mixing rule is used to determine  $\sigma_{Ar-Pt} = 2.938$  Å based on  $\sigma_{Ar-Ar}$  and  $\sigma_{Pt-Pt} = 2.5346$  Å [118]. The Pt-Pt particle interaction is modeled by harmonic potential given as

$$\varphi_p(r_{ij}) = \frac{1}{2} \Gamma (r_{ij} - r_o)^2, \quad (5.2)$$

where  $\Gamma = 67.360$  kcal/mol-Å<sup>2</sup>, and  $r_o = 2.77$  Å. The surface interaction ratio,  $\varepsilon^* = \varepsilon_{sf} / \varepsilon_{sf,Ar-Pt}$ , is used to indicate the material selection of the solid surface. Geometrical dimensionless parameters,  $l_p^*$  and  $l_z^*$  are defined as given in Eqs. (5.3) and (5.4), for the space between the nanopillars and their height as given as

$$l_p^* = \frac{l_{p,x}}{l_{p,x} + l_x}, \quad (5.3)$$

$$l_z^* = \frac{l_z}{L_z}, \quad (5.4)$$

where  $l_{p,x}$  is the distance among the nanopillars along the  $x$ -axis.  $l_x = 1.108$  nm,  $l_y = 0.960$  nm, and  $l_z$  varying from 0 to 3.169 nm are the nanopillar dimensions as shown in Figure 5.1. The same  $l_p^*$  is used for the  $y$ -axis.

For the condensation (filling) process, it is assumed that the thermal diode operation starts from  $T_2 > T_1 > T_{tr}$ , where Ar is in gaseous state with low number density (80 Ar particles are uniformly distributed inside the nanogap as the initial condition). As the upper surface temperature is gradually reduced during independent GCMC simulations, the number of Ar particles increases to reach the desired gas pressure. At the upper surface temperature  $T_2$  below the transition temperature,  $T_{tr}$ , the capillary transition (condensation) occurs, resulting in high Ar number density (liquid-like). The high Ar number density is used to calculate the initial distribution of Ar particles for the emptying process in the GCMC simulation, while gradually increasing  $T_2 = 70$  to 150 K.

The uncertainty of the heat flux based on the different initial Ar distributions is estimated for the capillary and adsorption state by repeating the simulations 3 times with the different initial Ar distributions. Note that the uncertainty of the heat flux of the adsorption state is higher than that of the capillary state [201]. However, the predicted uncertainty is negligibly small as shown below.

Near-field radiation across the nanogap, especially for the low pressure region, i.e., “off” mode, can be an additional source of heat transfer, which may potentially decrease the thermal isolation efficiency. However, the heat flux contribution of the near-field radiation is negligibly small since it is expected to be an order of  $0.01$  kW/cm<sup>2</sup> with  $\Delta T \sim 10$  K for a nanogap size of 5 nm [113, 202-204].

To validate the simulation setup and calculation approach, the predicted gas pressure and heat flux calculations are verified with the existing theories. For the NEMD simulations in adsorption state, the steady-state gas pressure and heat flux of the Ar-filled nanogap are validated using the

ideal gas law and kinetic theory [113]. The validation for the heat flux in condensed Ar (liquid-like) state is performed by comparing NEMD simulation results with the heat flux calculated by Fourier's law based on MD-predicted liquid Ar thermal conductivity,  $k_f = 0.127$  W/m-K [205]. The detailed validations for the heat flux in gaseous and liquid-like state are available in previous studies [201, 206-208].

## 5.4 Results and discussion

### 5.4.1 Nanopillar height ( $l_z^*$ ) effect

Figure 5.2(a) demonstrates the effect of nanopillar height  $l_z^*$  (one surface only) on the heat flux through the nanogap both in positive,  $T_1 > T_2$ , and negative,  $T_1 < T_2$ , heat flux directions at  $p_g = 1.66$  atm,  $T_1 = 110$  K, and  $T_2 = 70 - 150$  K including the complete nanogap filling/emptying cycle. Note that  $l_z^* = 0$  indicates no nanopillars (bare surface). For the bare surface, at the upper surface temperature,  $T_2 = 150$  K, the nanogap remains in the gas (adsorption) state, resulting in low heat flux,  $q_- = -0.135$  kW/cm<sup>2</sup>. As the upper surface temperature,  $T_2$ , decreases down to the lower surface temperature,  $T_1$ , the heat flux decreases since  $\Delta T$  reduces down to 0 at  $T_2 = T_1$ . As  $T_2$  further reduces below  $T_1$ , the heat flux direction changes as the temperature gradient direction shifts upward, i.e.,  $T_2 < T_1$ , and when  $T_2 < 80$  K (filling curve), the capillary transition occurs and it significantly increases the heat flux due to the high thermal conductivity (liquid-like Ar) such that  $q_+ = 11.5$  kW/cm<sup>2</sup> at  $T_2 = 70$  K. As  $T_2$  increases (emptying curve), the heat flux decreases almost linearly with increasing  $T_2$  up to 100 K with the noticeable hysteresis (different heat flux pathway between the emptying and filling curves). At  $T_2 > 100$  K, the capillary transition (evaporation) occurs and the capillary “bridge” across the nanogap is broken, resulting in adsorption (gas) state with low thermal conductivity and heat flux reduces from 3.424 to 0.122 kW/cm<sup>2</sup>. As the upper surface temperature further increases up to  $T_2 = 150$  K, no significant hysteresis is found. Note that

the noticeable hysteresis in heat flux stems from the hysteresis in the capillary filling and emptying [138, 139], and this potentially causes poor controllability of the thermal diode operation, i.e., additional temperature control system is required for desired thermal diode performance.

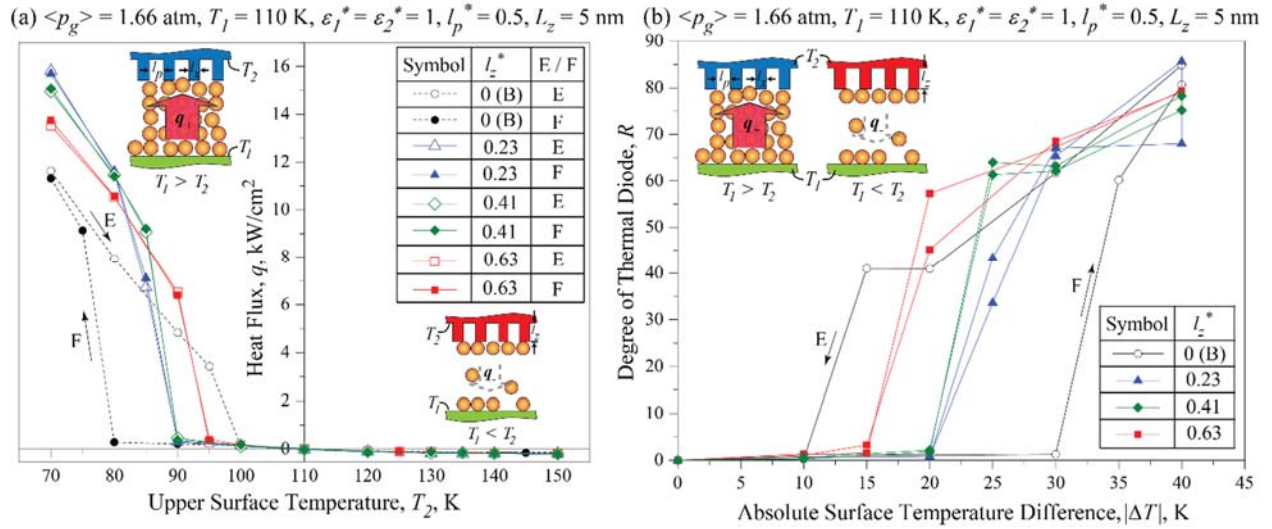


Figure 5.2. Variation of (a) heat flux through the nanogap as a function of the upper surface temperature,  $T_2$ , and (b) the degree of thermal diode,  $R$ , as a function of absolute surface temperature difference,  $|\Delta T|$ , through the nanogap with  $L_z = 5 \text{ nm}$  and  $l_z^* = 0$  (bare surfaces), 0.23, 0.41, and 0.63. “B”, “E”, and “F” represent bare surface, emptying, and filling curves, respectively. Insets correspond to heat flux by Ar particles in positive (capillary state) and negative (gaseous state) directions through the nanogap. Error bars are too small to be observed.

To minimize the hysteresis, nanopillars are employed on only one surface (upper surface). For the nanopillars with  $l_z^* = 0.23$  at  $T_2 > 90 \text{ K}$ , the heat flux is nearly identical to those for the bare surface. However, as  $T_2$  decreases below 90 K, the heat flux significantly increases from  $q_+ = 0.281$  to  $7.103 \text{ kW/cm}^2$  and it increases up to  $q_+ = 16 \text{ kW/cm}^2$  at  $T_2 = 70 \text{ K}$ . As  $T_2$  increases during the emptying curve, the heat flux decreases without significant hysteresis up to  $T_2 = 150 \text{ K}$ . As the nanopillar height increases,  $l_z^* = 0.41$ , the capillary transition temperature is the same as that of  $l_z^* = 0.23$ , although  $l_z^* = 0.41$  results in a larger heat flux at  $T_2 = 85 \text{ K}$ . The larger heat flux stems from the fact that the higher nanopillar heights lead to the larger surface area at the onset of the capillary transition. A further increase in the nanopillar height,  $l_z^* = 0.63$ , results in capillary transition at

the elevated temperature,  $T_2 = 90$  K. Resulting heat fluxes are  $q_+ = 6.392$  and  $13.742$  kW/cm<sup>2</sup> at  $T_2 = 90$  K and  $70$  K, respectively, and no significant hysteresis is found as  $T_2$  increases to  $150$  K.

The degree of thermal diode,  $R$ , is determined using predicted  $q_+$  and  $q_-$  [Figure 5.2(a)] and Eq. (1.2), which is shown in Figure 5.2(b) as a function of the absolute temperature difference between two surfaces,  $|\Delta T| = |T_2 - T_1|$ . For the bare surface, the noticeable thermal diode effect appears at  $|\Delta T| > 30$  K (or  $T_2 < 80$  K) and  $R_{max} \sim 85$  for the filling curve, while it disappears at  $|\Delta T| < 10$  K (or  $T_2 > 100$  K) for the emptying curve, i.e., significant hysteresis. With the inclusion of the nanopillars on one surface only, i.e.,  $l_z^* = 0.23, 0.41,$  and  $0.63$ , the onset temperature gradient of the thermal diode reduces down to  $|\Delta T| = 15$  to  $20$  K from  $|\Delta T| = 30$  K (bare surface), and also the hysteresis significantly reduces. For all nanogaps with  $l_z^* > 0$ , the maximum degree of the thermal diode is similar to that of the bare surface, while for  $l_z^* = 0.41,$  and  $0.63$ ,  $R$  enhances at  $|\Delta T| = 20$  to  $40$  K.

#### 5.4.2 Nanogap size ( $L_z$ ) effect

Figure 5.3(a) demonstrates the nanogap size,  $L_z$ , effect on the heat flux both in positive,  $T_1 > T_2$ , and negative,  $T_1 < T_2$ , directions at  $p_g = 1.66$  atm,  $T_1 = 110$  K, and  $T_2 = 70 - 150$  K including the complete filling/emptying cycle. Note that  $l_z^* = 0$  indicates no nanopillars (bare surface).

For the bare surface, the heat flux variation in the filling curve from  $T_2 = 150$  to  $90$  K with  $L_z = 10$  nm is identical to that with  $L_z = 5$  nm, as discussed in Section 5.4.1. However, the capillary condensation for the larger nanogap is observed at a slightly lower temperature,  $T_2 = 70$  K, compared to  $T_2 = 75$  K for the smaller nanogap with  $L_z = 5$  nm. As  $T_2$  increases, the emptying curve for both small and large nanogaps is similar although the heat flux for  $L_z = 10$  nm is slightly smaller, linearly decreasing from  $10.773$  kW/cm<sup>2</sup> at  $T_2 = 70$  K to  $2.927$  kW/cm<sup>2</sup> at  $T_2 = 95$  K, followed by a significant heat flux decrease down to  $0.085$  kW/cm<sup>2</sup> at  $T_2 = 100$  K due to the

capillary evaporation (adsorption). For  $L_z = 10$  nm, the hysteresis becomes more pronounced compared to that of  $L_z = 5$  nm, which potentially requires additional temperature controllers for the practical thermal diode operations.

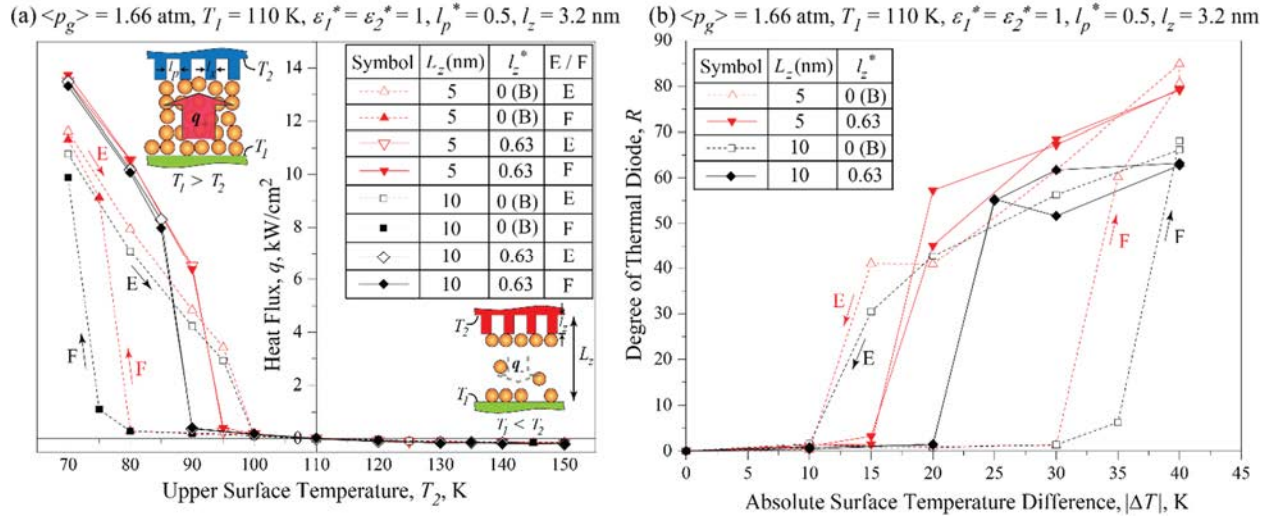


Figure 5.3. Comparison of (a) heat flux through the nanogap as a function of the upper surface temperature,  $T_2$ , and (b) the degree of thermal diode,  $R$ , as a function of absolute surface temperature difference,  $|\Delta T|$ , through the nanogaps with different nanogap size,  $L_z = 5$  and 10 nm, for  $l_z^* = 0$  (bare surfaces) and 0.63. “B”, “E”, and “F” represent bare surface, emptying, and filling, respectively. Insets correspond to heat transfer by Ar particles in positive (capillary state) and negative (gaseous state) directions through the nanogap. Error bars are too small to be observed.

The hysteresis becomes negligibly small by adding nanopillars with  $l_z = 3.2$  nm to the upper surface, where  $l_z = 3.2$  nm is equivalent to  $l_z^* = 0.63$  and 0.32 for  $L_z = 5$  and 10 nm, respectively. For both sizes of the nanogap, as the upper surface temperature decreases from  $T_2 = 150$  to 110 K, heat flux (downward) decreases due to the low gas thermal conductivity for  $T_2 > T_1 > T_{tr}$ . However, as the upper surface temperature further decreases below  $T_1$ , the heat flux direction changes. For the larger nanogap,  $L_z = 10$  nm, heat flux begins to significantly increase at  $T_2 < 90$  K due to the capillary transition, and this is lower than the capillary transition temperature in the smaller nanogap which stems from the weaker overlapping surface force for larger nanogap size [209].

Heat flux for both nanogap sizes becomes similar at  $T_2 < 85$  K with  $q_+ \sim 13.5$  kW/cm<sup>2</sup> at  $T_2 = 70$  K ( $\Delta T = 40$  K). The hysteresis between the filling and emptying curves is not noticeable for any of the nanogaps with nanopillars on one surface only.

The degree of thermal diode,  $R$ , is determined using predicted  $q_+$  and  $q_-$  [Figure 5.3(a)] and Eq. (1.2), which is shown in Figure 5.3(b) as a function of the absolute temperature difference between two surfaces,  $|\Delta T| = |T_2 - T_1|$ . For the large nanogap with bare surfaces, the thermal diode effect is noticeable at  $|\Delta T| > 35$  K (or  $T_2 < 75$  K) and  $R_{max} \sim 70$  for the filling curve, while it becomes small at  $|\Delta T| < 10$  K (or  $T_2 > 100$  K) for the emptying curve, i.e., the hysteresis is even more significant for the larger nanogap with bare surfaces. With the inclusion of the nanopillars on one surface only, i.e.,  $l_z = 3.2$  nm, the onset of the absolute temperature difference for the thermal diode reduces down to  $|\Delta T| = 15$  and 20 K from  $|\Delta T| = 30$  K and 35 K (bare surface) for the small and large nanogaps, respectively, and the hysteresis also significantly reduces.  $R_{max} \sim 65$  for the larger nanogap with nanopillars is smaller than that of the smaller gap,  $R_{max} = 80$ , and this stems from the lower heat flux for the adsorption state with  $L_z = 5$  nm due to higher Knudsen number [121, 201].

#### 5.4.3 Surface interaction ( $\varepsilon^*$ ) effect in nanogaps with both bare surfaces

Figure 5.4(a) shows the effect of nanogap with two different materials (material heterogeneity) on the heat flux both in positive,  $T_1 > T_2$ , and negative,  $T_1 < T_2$ , directions at  $p_g = 1.66$  atm,  $T_1 = 110$  K, and  $T_2 = 70 - 150$  K including the complete filling/emptying cycle. For the material heterogeneity, two sets of simulations are examined. First, the lower surface  $T_1$ , is a surface with a weaker Ar-solid interaction compared to Pt,  $\varepsilon_1^* = 0.6$ , e.g., Pb [118], while the upper surface,  $T_2$ , is Pt surface,  $\varepsilon_2^* = 1$ . Second, the upper surface  $T_2$ , is Pb, and the lower surface  $T_1$ , is Pt, i.e.,  $\varepsilon_1^* = 1$  and  $\varepsilon_2^* = 0.6$ .

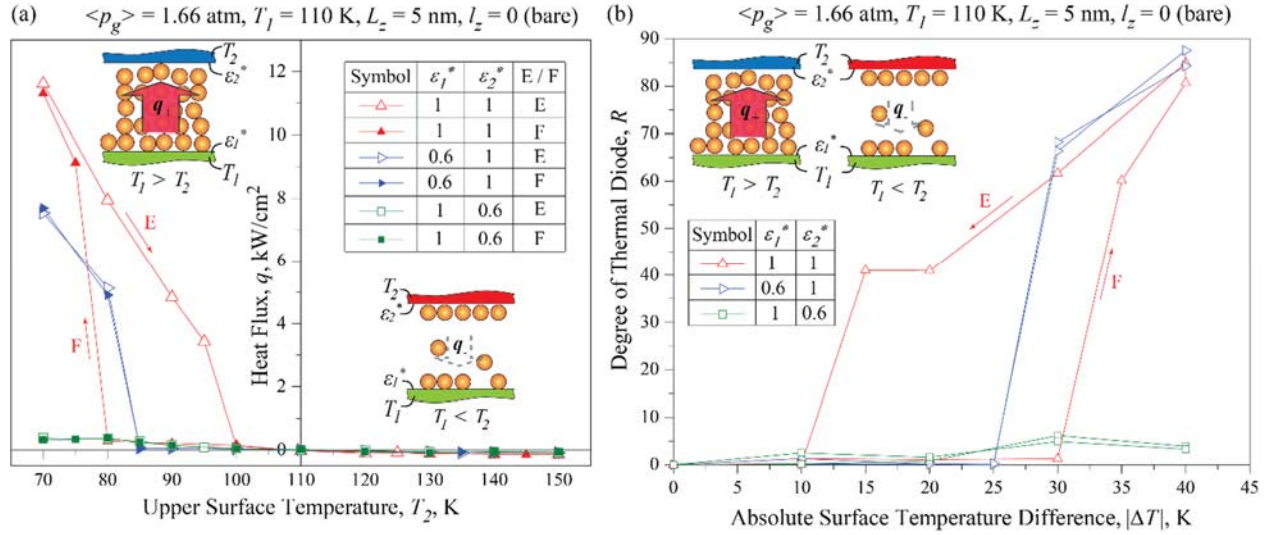


Figure 5.4. Variation of (a) heat flux through the nanogap as a function of the upper surface temperature,  $T_2$ , and (b) the degree of thermal diode,  $R$ , as a function of absolute surface temperature difference,  $|\Delta T|$ , through the nanogaps with  $L_z = 5 \text{ nm}$  and  $l_z^* = 0$  (bare surfaces), where the solid-fluid interaction,  $\varepsilon^*$ , on each surface may be different as indicated in the inset table. “E” and “F” represent emptying and filling, respectively. Insets correspond to heat transfer by Ar particles in positive (capillary state) and negative (adsorption state) directions through the nanogap. Error bars are too small to be observed.

For the nanogap with  $\varepsilon_1^* = 0.6$  and  $\varepsilon_2^* = 1.0$  (first case), at the upper surface temperature,  $T_2 = 150 \text{ K}$ , nanogap remains in the gas (adsorption) state, resulting in low heat flux,  $q_- = -0.090 \text{ kW/cm}^2$ . As the upper surface temperature,  $T_2$  decreases down to the lower surface temperature,  $T_l$ , the heat flux decreases since  $\Delta T$  reduces down to 0 at  $T_2 = T_l$ . As  $T_2$  further reduces below  $T_l$ , the heat flux direction changes as the temperature gradient direction changes, i.e.,  $T_2 < T_l$ , and when  $T_2 < 85 \text{ K}$  (filling curve), the capillary transition occurs and it significantly increases the heat flux due to the high thermal conductivity (liquid-like Ar) such that  $q_+ = 7.7 \text{ kW/cm}^2$  at  $T_2 = 70 \text{ K}$ . As  $T_2$  increases, heat flux through the emptying curve shows a trend very similar to that for filling curve, i.e. negligible hysteresis. In fact, the material heterogeneity equivalently reduces the hysteresis for the thermal diode as demonstrated in the structural heterogeneity (nanopillars on one surface only). However, for the second case, i.e.,  $\varepsilon_1^* = 1$  and  $\varepsilon_2^* = 0.6$ , no capillary transition is

found even at  $T_2 = 70$  K (adsorption state), thereby leading to the low heat flux for  $70 \leq T_2 \leq 150$  K.

The degree of thermal diode,  $R$ , is determined using predicted  $q_+$  and  $q_-$  [Figure 5.4(a)] and Eq. (1.2), as shown in Figure 5.4(b) as a function of the absolute temperature difference between two surfaces,  $|\Delta T| = |T_2 - T_1|$ . The material heterogeneity, i.e.,  $\varepsilon_1^* = 0.6$  and  $\varepsilon_2^* = 1$ , not only reduces the onset of the absolute temperature difference for the thermal diode down to  $|\Delta T| = 25$  K from  $|\Delta T| = 30$  K, but also significantly reduces hysteresis, compared to the nanogap with the homogeneous materials, i.e.,  $\varepsilon_1^* = \varepsilon_2^* = 1$ . The maximum degree of the thermal diode is similar for both cases,  $R_{max} \sim 85$ . For the nanogap with  $\varepsilon_1^* = 1$  and  $\varepsilon_2^* = 0.6$ , no significant thermal diode effect is observed since no capillary transition occurs, i.e., no significant heat flux contrast between the capillary and adsorption states.

#### 5.4.4 Surface interaction ( $\varepsilon^*$ ) effect in nanogaps with one structured surface

Figure 5.5(a) shows the effect of nanogaps with nanopillars on one surface only and two different solid surfaces (coupled structural-material heterogeneity) on the heat flux in positive,  $T_1 > T_2$ , and negative,  $T_1 < T_2$ , directions at  $p_g = 1.66$  atm,  $T_1 = 110$  K,  $L_z = 5$  nm,  $l_z^* = 0.63$ , and  $T_2 = 70 - 150$  K including the complete filling/emptying cycle. For the coupled structural-material heterogeneity, two simulations are considered here. First, the lower surface  $T_1$ , has a weaker fluid-solid interaction compared to Pt surface,  $\varepsilon_1^* = 0.6$ , e.g., Pb [118], while the upper surface with the nanopillars  $T_2$ , is Pt surface,  $\varepsilon_2^* = 1$ . Second, the lower surface,  $T_1$ , is bare Pt surface,  $\varepsilon_1^* = 1$ , while the upper surface with nanopillars  $T_2$  has the weaker fluid-solid interaction  $\varepsilon_2^* = 0.6$ , e.g., Pb.

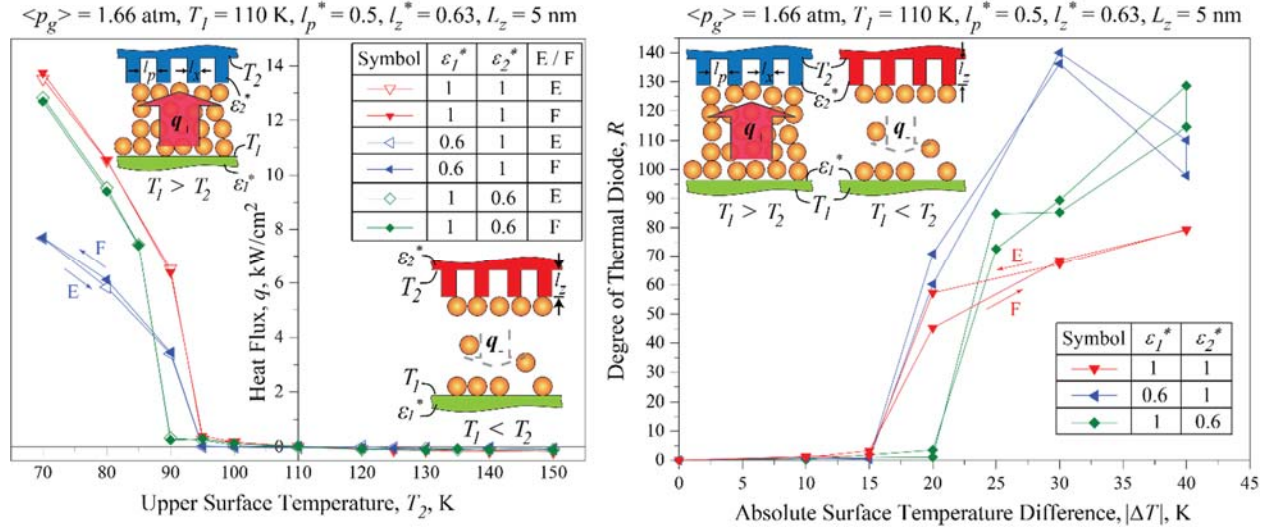


Figure 5.5. Variation of (a) heat flux through the nanogap as a function of the upper surface temperature,  $T_2$ , and (b) the degree of thermal diode,  $R$ , as a function of absolute surface temperature difference,  $|\Delta T|$ , through the nanogaps with  $L_z = 5 \text{ nm}$  and  $l_z^* = 0.63$ , where the solid-fluid interaction,  $\varepsilon^*$ , on each surface may be different as indicated in the inset table. “E” and “F” represent emptying and filling, respectively. Insets correspond to heat transfer by Ar particles in positive (capillary state) and negative (gaseous state) directions through the nanogap. Error bars are too small to be observed.

For the first case, at the upper surface temperature  $T_2 = 150 \text{ K}$ , the nanogap remains in gaseous (adsorption) state, resulting in low heat flux,  $q_- = -0.069 \text{ kW/cm}^2$ . As the upper surface temperature,  $T_2$  decreases down to the lower surface temperature,  $T_1$ , heat flux decreases since  $\Delta T$  reduces down to 0 at  $T_2 = T_1$ . As  $T_2$  further reduces below  $T_1$ , the heat flux direction reverses upward, i.e.,  $T_2 < T_1$ , and when  $T_2 < 95 \text{ K}$  (filling curve), the capillary transition occurs. This in turn results in a significant increase in heat flux due to the high thermal conductivity (liquid-like Ar) such that  $q_+ = 7.7 \text{ kW/cm}^2$  at  $T_2 = 70 \text{ K}$ , however, this is smaller than the nanogap with nanopillars on one surface only using the same materials, i.e.,  $\varepsilon_1^* = \varepsilon_2^* = 1$  due to the reduced fluid-solid interaction at the upper surface. As  $T_2$  increases to  $150 \text{ K}$ , the elevated temperature leads to the capillary to adsorption transition (capillary evaporation), resulting in heat flux reduction. The predicted heat flux for the emptying curve is similar to that for the filling curve at given upper

surface temperature  $T_2$ , i.e. negligible hysteresis. Note that here, the heat flux at  $T_2 > 110$  K is lower due to the reduced fluid-solid interaction on the lower surface, i.e., poor  $q_-$ , and this results in higher  $R$ , as shown in Figure 5.5(b).

For the second case, the capillary transition occurs at  $T_2 = 85$  K ( $\Delta T = 25$  K), i.e. 5 K smaller than the other cases discussed in this section. The capillary transition increases the heat flux from  $0.253$  kW/cm<sup>2</sup> to  $7.414$  kW/cm<sup>2</sup> at  $T_2 = 85$  K, and it increases the heat flux up to  $q_+ \sim 13$  kW/cm<sup>2</sup> as the upper surface temperature is reduced to  $T_2 = 70$  K. This is marginally smaller than that for the nanogap with nanopillars and  $\varepsilon_1^* = \varepsilon_2^* = 1$ , showing that the nanopillars have a dominant effect on increasing the heat flux in liquid-like state.

The degree of thermal diode,  $R$ , is determined using predicted  $q_+$  and  $q_-$  [Figure 5.5(a)] and Eq. (1.2), as shown in Figure 5.5(b) as a function of the absolute temperature difference between two surfaces,  $|\Delta T| = |T_2 - T_1|$ . The coupled structural-material heterogeneity (both cases) significantly improves the thermal diodicity compared to the structural heterogeneity only. For the nanogap with  $\varepsilon_1^* = 0.6$  and  $\varepsilon_2^* = 1$ , the noticeable thermal diode effect appears at  $|\Delta T| > 15$  K, with  $R_{max} \sim 140$  at  $\Delta T = 30$  K. For the nanogap with  $\varepsilon_1^* = 1$  and  $\varepsilon_2^* = 0.6$ , the noticeable thermal diode effect appears at  $|\Delta T| > 20$  K with  $R_{max} \sim 120$  at  $\Delta T = 40$  K, compared to  $R_{max} \sim 80$  for the nanogap with  $\varepsilon_1^* = \varepsilon_2^* = 1$ .

## 5.5 Conclusion

In this study, asymmetric heat flux through the nanogaps with structural and material heterogeneity and coupled structural/material heterogeneity are examined, aiming at developing the compact and efficient adsorption-capillary-transition-controlled thermal diode using GCMC and NEMD simulations. A highly efficient thermal diode,  $R_{max} = 140$  is achieved by a significant thermal conductivity contrast between the gas (adsorption only) and liquid (capillary) states

without significant hysteresis, controlled by the structural heterogeneity (nanopillars on one surface only) and material heterogeneity (two different materials for nanogap surfaces) at constant pressure.

The predicted results show that the homogeneous nanopores (nanogap with both bare surfaces and same solid materials) is not suitable for the capillary-controlled thermal diode design due to the significant hysteresis in capillary transition. It is found that the nanopillars on one surface only ( $l_z^* = 0.23, 0.41, \text{ and } 0.63$ ) minimize the hysteresis, which enables the thermal diode operate without additional temperature controllers. Moreover, the nanopillars decrease the absolute surface temperature difference,  $|\Delta T|$ , for the thermal diode activation, and it also provides  $R \sim 85$ . It is also found that increasing the nanogap size from  $L_z = 5 \text{ nm}$  to  $10 \text{ nm}$ , increase the absolute surface temperature difference,  $|\Delta T|$ , and decrease the degree of thermal diode,  $R$ , by 25 %. The minimal hysteresis in capillary transition is equivalently achieved by employing a weaker fluid-surface interaction only on the lower surface without nanopillars,  $\varepsilon_l^* = 0.6$ , i.e., material heterogeneity, showing  $R_{max} \sim 85$ , but at the reduced heat flux due to the lower solid-fluid interaction (larger interfacial resistance). Employing a weaker fluid-surface interaction only on the upper surface with nanopillars (coupled structural and material heterogeneity) results in  $R \sim 120$  without reducing the heat flux.

The suggested design for the capillary-transition-driven thermal diode has the potential to be used at various temperatures with the careful selection of the condensable gas and operating pressure. This result can be synergetically integrated with a recently demonstrated adsorption-controlled thermal switch [201, 208] for designing advanced thermal management systems, i.e., thermal logic gates and computers.

## CHAPTER 6

### CAPILLARY-CONTROLLED THERMAL SWITCH IN HETEROGENEOUS NANOSTRUCTURES<sup>1</sup>

#### 6.1 Introduction

A thermal switch is a system which maximizes (“on” mode) or minimizes (“off” mode) a thermal transport on demand, and it critically serves as a thermal management system in various applications including energy dissipation and thermal stabilization in miniaturized devices [210, 211], spacecraft [212], energy scavenging [213, 214], and the realization of thermal circuits/logic gates [92]. The efficient thermal switch needs an outstanding contrast between thermal transport in “on” and “off” modes with a reasonable response time, i.e., good thermal conductor in “on” mode and thermal insulator in “off” mode.

To improve the degree of thermal switch, various thermal switching mechanisms have been explored using nonlinear conduction, convection, radiation, or the combination of them. The conduction-based thermal switch primarily benefits from the mechanical movements of thermal switching mechanisms using temperature-controlled and non-temperature controlled actuators. Temperature-controlled actuating approaches include methods based on Differential Thermal Expansion (DTE) [97, 215-218], as well as the characteristics of shape memory alloys [212], bi-metallic materials [86], three-terminal graphene nanoribbons [219], liquid-metal phase-change-based volume expansion [98, 220-223], or different thermal accommodation coefficient on

---

<sup>1</sup> This entire chapter has been submitted for publication to the following source:

- Avanesian, T. and Hwang, G., *Thermal switch using controlled capillary transition in heterogeneous nanostructures*. International Journal of Heat and Mass Transfer, Submitted September 2017.

heterogeneous surfaces of the nanogaps [206]. Thermal switch demonstrations by non-temperature-controlled actuating approaches include gas pressure control in gas-gap setups [87, 88, 95, 213, 214, 224], employing electrostatic actuation [100], liquid water morphological change on Teflon coated substrates [225], dielectric liquids [102], temperature-dependent oscillation of the ferromagnetic materials [104], and carbon nanotube deflection by electrostatic loads [226]. Nonlinear-convection-based thermal switches have been also explored by approaches based on heat pipes controlled by shape memory alloys [99], double-loop heat pumps [227], and three-internally-layered setups with one hydrophilic and one hydrophobic surface [228]. Nonlinear radiation achieved by controllable emissivity [101, 105], near-field radiation [229, 230], thermoelectricity [231], magnetic field between the heat source and sink [84], or VO<sub>2</sub> insulator-to-metal phase transition [211] can also offer thermal switching mechanisms. Applying recent molecular-level theoretical studies explore another branch of thermal switching demonstrations based on quantum thermal shuttling between the source and the sink [232], temperature-biased quantum junctions [233, 234], and three-terminal Coulomb-coupled quantum dots [235].

In gas-filled nanostructures, the gas prematurely turns into liquid state, i.e., adsorption-capillary transition, below the saturation pressure at given temperature [138, 139]. This transition is associated with the gas pressure, temperature, surface-fluid interaction, and structural parameters [209]. This transition between the states includes not only the morphological changes, i.e., adsorption to capillary, but also thermal properties such as the low thermal conductivity of gas to the high thermal conductivity of liquid. This significant gas thermal conductivity change between two states could potentially lead to the thermal switching mechanism, but it has not been fully realized yet.

In this study, we examine an adsorption-capillary-transition-controlled thermal switch in a nanogap with movable nanopost structures where the nanogap surfaces also operate as the heat source and the heat sink. The switch performance is demonstrated with controlled nanopost height on one surface only, using Grand Canonical Monte Carlo (GCMC) simulation combined with Non-Equilibrium Molecular Dynamics (NEMD) simulations. The heat fluxes across the gas-filled nanostructures and degree of thermal switch are predicted as functions of operating temperature, nanostructure geometries, and solid-fluid interaction parameters. Optimal designs and operating conditions are also discussed. This new class of thermal switching mechanism is compatible with the thermal diode and transistor mechanisms [206, 207] and is capable of achieving  $S \sim 170$  in an order of 10 ns.

## 6.2 Working principle

The adsorption-capillary-transition-controlled thermal switch stems from a large thermal transport contrast between the adsorption and capillary states in heterogeneous nanostructures. The adsorption-capillary transition in nanostructures is related to the surface tension of fluid, gas pressure, temperature, and the size of the nanostructures [138, 139]. To further control the adsorption-capillary transition, a heterogeneous nanostructure aiming at designing the thermal switch, i.e., Ar-gas filled Pt-based nanogap with nanoposts on one side only, is employed as shown in Figure 6.1(a) to (c). Detailed discussions on the adsorption-capillary transition in Ar-filled heterogeneous nanostructure are found in previous work [209], but this study primarily focuses on the thermal switching mechanism due to the adsorption-capillary transition. At high temperature and low gas pressure, Ar fills the nanogap as gaseous state, i.e., adsorption state. The thermal conductivity across the Ar-gas filled nanostructure is relatively small due to the low number

density of gas and large interfacial resistance between the gas and solid, i.e., Thermal Accommodation Coefficient (TAC). This low thermal conductivity serves as the “off” mode.

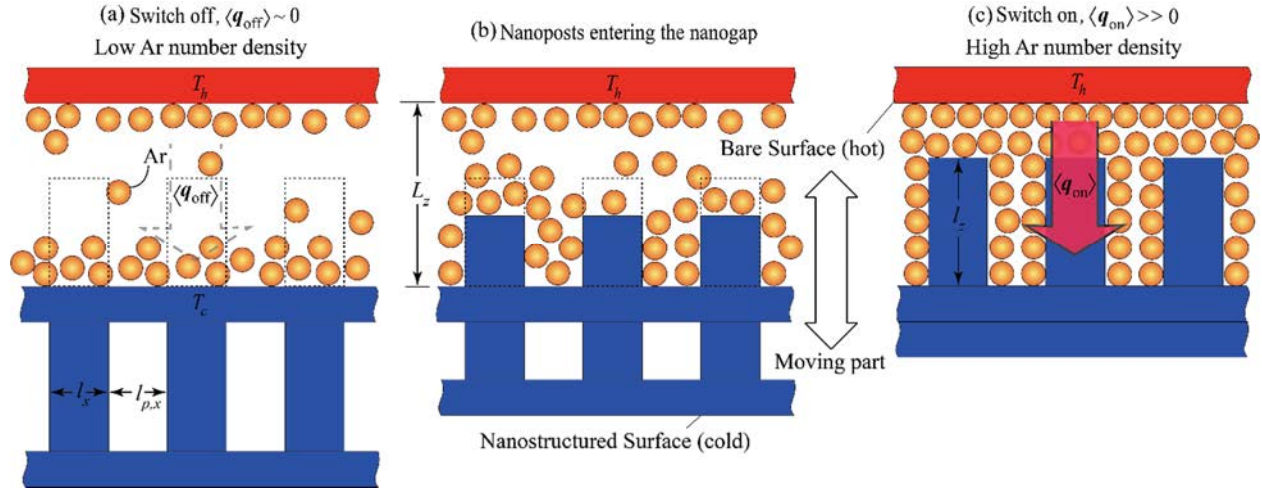


Figure 6.1. Schematic drawing of adsorption-capillary-controlled thermal switch at given pressure and temperature. (a) Nanoposts are located outside the nanogap, aiming at delaying the capillary transition (gas state only) for switch “off” mode. (b) A snapshot of the intermettant stage between switch “on” and “off” under given gas pressure. (c) Nanoposts are mechanically moved into the nanogap to facilitate capillary transition (condensation) at the given temperature, thereby resulting in switch “on” mode. The dimensions for the nanogap and nanoposts are also shown.

For the “on” mode, a higher thermal conductivity across the capillary-condensed Ar in a heterogeneous nanostructure is achieved by inserting nanoposts into the nanogap as shown in Figure 6.1(c). The higher thermal conductivity for the condensed Ar in the nanostructure primarily stems from the higher Ar number density and phononic energy transfer, given as [113, 236]

$$k_f = \frac{3R_g}{N_A^{1/3}} \frac{\rho_f^{1/6}}{M^{2/3}} \left( \frac{c_{p,f}}{c_{v,f}} \frac{1}{\kappa_f} \right)^{1/2}, \kappa_f = \frac{1}{\rho_f} \frac{\partial \rho_f}{\partial p} \Big|_T \quad (6.1)$$

where  $N_A$  is the Avogadro Number,  $\rho_f$  is the fluid density, and  $c_{p,f}$  and  $c_{v,f}$  are the specific heat at constant pressure and volume, respectively.

Note Ar is chosen here for the proof of concept with relatively well-studied potential in literature [120, 121, 133, 184] and relatively smaller computational cost (monatomic gas).

However, this working principle can be extended to the different types of fluid as long as the gas is condensable at given temperature and pressure, for example, water at ambient pressure and temperature.

To insert/remove the nanoposts into/from the nanogap, thermally-expandable V-shaped bent beam actuators can be used [198]. Note that the main advantage of the adsorption-capillary-transition-controlled thermal switch over other thermal switching mechanisms using a direct mechanical contact between the heat source and sink is a non-mechanical thermal switching mechanism, i.e., thermal “bridging” by capillary filling between the heat source and sink, thereby allowing for a minimal maintenance.

In fact, the aforementioned thermal switch working principle can be equivalently achieved by controlling the gas pressure for the adsorption-capillary transition without the nanopost movement. The expected level of the thermal switch is very similar to the nanopost-movement-based approach at given pressure, however, we focus on the thermal switch using the nanopost-movement-controlled working principle, since it provides a passive thermal switch mechanism compared to the active, complex gas pressure control [87, 88, 95, 213, 214, 224]. For the nanogap size of 5 nm, the nanoposts need to move only 1 to 4 nm as discussed below, and this can be achieved based on the thermal expansion controlled mechanical movement [198].

### **6.3 Simulation method**

To demonstrate the aforementioned working principle, the GCMC simulations combined with NEMD simulations are employed where the nanogap dimensions are  $L_x = 8.864$  nm,  $L_y = 7.676$  nm, and  $L_z = 5$  nm, Figure 6.1(a). Periodic boundary conditions are used for the  $x$ - and  $y$ - axes, while the fixed non-periodic boundary is used for  $z$ -axis. The upper and lower surfaces of the bare nanogap each consist of three layers of Face Centered Cubic (FCC, 111 plane) Pt-based solid. One

fixed layer is added as the outermost layer to the upper and lower plates in order to prevent the setup from moving freely. For simulating the structured surface, the nanoposts are added to the innermost solid layer with the same FCC pattern having uniform height and space between the columns. The simulations run independently for each characteristic spacing and height of the nanogap. The simulations are performed in two steps. Firstly, GCMC simulation is used [183] to determine the number of Ar particles for desired pressure in the nanogap with/without nanoposts. Secondly, NEMD runs using the determined number density from GCMC as initial position and velocity distributions. For MD, the velocity-Verlet algorithm is used for the time integration over time steps of 2 fs [129], and the equilibrium state is achieved by simulating it for 6 ns using Nose-Hoover thermostat at  $T_{ave}$  for the entire system [130, 131]. Then, the temperature gradient is created by imposing the upper/lower surface temperatures using Langevin thermostat [132] for 14 ns, while the kinetic energy (temperature) of the solid atoms is maintained using the random force input to control the temperature relaxation. To run the GCMC and NEMD simulations, the Large-scale Atomic/Molecular Massively Parallel Simulator (LAMMPS) was used [134, 135].

Lennard-Jones potential between Ar-Ar and Ar-solid particles is used, given as

$$\varphi_{ij}(r) = 4\varepsilon_{ij} \left[ \left( \frac{\sigma}{r_{ij}} \right)^{12} - \left( \frac{\sigma}{r_{ij}} \right)^6 \right], \quad r_{ij} < r_{cut-off}, \quad (6.2)$$

where  $\varepsilon_{ff} = 0.2403$  kcal/mol for Ar-Ar [133],  $\varepsilon_{sf} = 0.1573$  kcal/mol for Ar-Pt with  $r_{cut-off} = 1.2$  nm [184], and  $\sigma$  indicates the distance for which no repulsive or attractive potential exists between particles. For Ar - Ar interaction  $\sigma_{Ar-Ar} = 3.405$  Å and for Ar - Pt interactions the geometric mixing rule is used to determine  $\sigma_{Ar-Pt} = 2.938$  Å based on  $\sigma_{Ar-Ar}$  and  $\sigma_{Pt-Pt} = 2.5346$  Å [118]. The Pt-Pt particle interactions are modeled by harmonic potential given as

$$\varphi_{ij}(r_{ij}) = \frac{1}{2} \Gamma (r_{ij} - r_o)^2, \quad (6.3)$$

where  $\Gamma = 67.360 \text{ kcal/mol-}\text{\AA}^2$ , and  $r_o = 2.77 \text{ \AA}$ . The surface interaction ratio,  $\varepsilon^* = \varepsilon_{sf}/\varepsilon_{sf,Ar-Pt}$ , is used to indicate the material selection of the solid surface. Geometrical dimensionless parameters,  $l_p^*$  and  $l_z^*$  are defined as given in Eqs. (6.4) and (6.5), for the space between the nanoposts and their height as given as

$$l_p^* = \frac{l_{p,x}}{l_{p,x} + l_x}, \quad (6.4)$$

$$l_z^* = \frac{l_z}{L_z}, \quad (6.5)$$

where  $l_{p,x}$  is the distance among the nanoposts along the  $x$ -axis. The  $l_x = 1.108 \text{ nm}$ ,  $l_y = 0.960 \text{ nm}$ , and  $l_z$  varying from 0 to 4.074 nm are the nanopost dimensions as shown in Figure 6.1(a). The same  $l_p^*$  is used for the  $y$ -axis.

The capillary state is determined at the onset of the significant Ar number density change, while gradually increasing temperature in GCMC simulations. The detailed discussions on the effects of nanopost geometrical parameters and surface interaction on the adsorption isotherm and isobar (including capillary transition) are found in the previous work [209, 237].

Near-field radiation across the nanogap, especially for the low pressure region, i.e., “off” mode, can be an additional source of heat transfer, which may potentially decrease the thermal isolation efficiency. However, the contribution from the near-field radiation is negligibly small since it is expected to be an order of  $0.01 \text{ kW/cm}^2$  with  $\Delta T \sim 10 \text{ K}$  for a nanogap size of 5 nm [113, 202-204].

## 6.4 Validation

To validate the simulation setup and calculation approach, the predicted gas pressure and heat flux calculations are verified against existing theories. The validation is performed for the bare surfaces only due to the simple geometry, assuming that the simulation approaches on the heat

flux calculation are valid for the nanogap with nanoposts without sacrificing generality. For the NEMD simulations in adsorption state, the validation of steady-state gas pressure and heat flux of the Ar-filled nanogap is discussed in chapter 2. The validation for the heat flux in condensed Ar (liquid-like state) is performed comparing NEMD simulation with  $\Delta T = 10$  K at  $T_{ave} = 93$  K with the predicted result using the Fourier's law with MD-predicted liquid Ar thermal conductivity,  $k_f = 0.127$  W/m-K [205]. Note that the temperature jump at the interfaces due to the Kapitza resistance makes this comparison convoluted [238, 239] (see Ar local temperature distribution for bare surfaces and surface with the nanoposts shown in Figure 6.2). However, we focus on the heat flux through the Ar excluding the Kapitza resistance for validation.

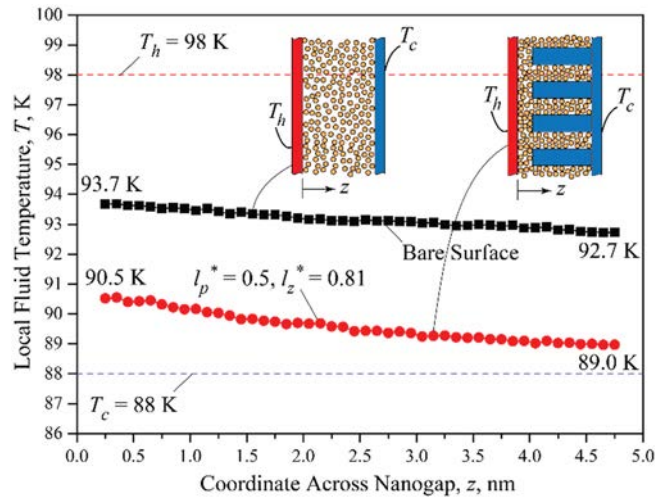


Figure 6.2. Local temperature distributions across the Ar-filled nanogap with bare surfaces and nanoposts on one surface only, including the interfacial temperature jumps, i.e., Kapitza resistance. The insets show the schematic drawings of the simulation setups and the direction of the temperature gradient.

In other words, the heat flux through the nanogap with bare surfaces is calculated only through the liquid Ar excluding the temperature jumps and  $q = 2.848$  kW/cm<sup>2</sup> predicted here using the NEMD reasonably agrees with  $q = 2.771$  kW/cm<sup>2</sup> using Fourier's law and  $k_f$  given in literature [205].

## 6.5 Results and discussion

### 6.5.1 Nanopost height ( $l_z^*$ ) effect

Figure 6.3(a) shows the variations of the heat flux across the nanogap surfaces as a function of the dimensionless nanopost height,  $l_z^*$ , at different nanogap average temperatures,  $T_{ave} = 93$  to 120 K, for  $\Delta T = 10$  K,  $p = 1.66$  atm,  $L_z = 5$  nm, and  $l_p^* = 0.33$ . It is noted that the thermal switching is critically related to the adsorption to capillary state transition in the nanostructure at given geometrical parameters of nanoposts, pressure and temperature. The detailed adsorption isotherm and isobar are discussed in the previous work [209]. Here, we focus on the resulting heat flux and the degree of thermal switch,  $S$ . At  $T_{ave} = 93$  K, Ar remains in capillary condensate (liquid-like) state due to the low temperature, and the higher liquid thermal conductivity in turn results in  $q = 3$  to 3.5 kW/cm<sup>2</sup> for  $l_z^* = 0$  to 0.81. At  $T_{ave} = 100$  K, Ar in the small nanopost height,  $l_z^* \leq 0.5$  is in adsorption state, and the resulting heat flux is small because of the low thermal conductivity of gas. At  $l_z^* = 0.63$ , capillary condensation occurs since the effective nanogap size decreases, and this in turn results in a significantly higher heat flux due to the high liquid thermal conductivity. A further increase in the nanopost height results in  $\sim 24\%$  decrease in the heat flux due to a reduced Ar number density in the nanogap in presence of higher nanoposts in nanogap resulting from larger occupying regions near the nanopost surfaces. At  $T_{ave} = 104$  K, the capillary transition occurs at a higher nanopost height,  $l_z^* = 0.72$ , since the higher temperature delays the adsorption to capillary transition [209]. At the elevated temperatures, 105 K and 110 K, the capillary transition requires the higher nanopost height,  $l_z^* = 0.81$ . Note that the capillary transition is not observed for temperatures above 120 K at  $\langle p_g \rangle = 1.66$  atm due to the high kinetic energy from the high temperature, i.e., the temperature is too high for capillary condensation.

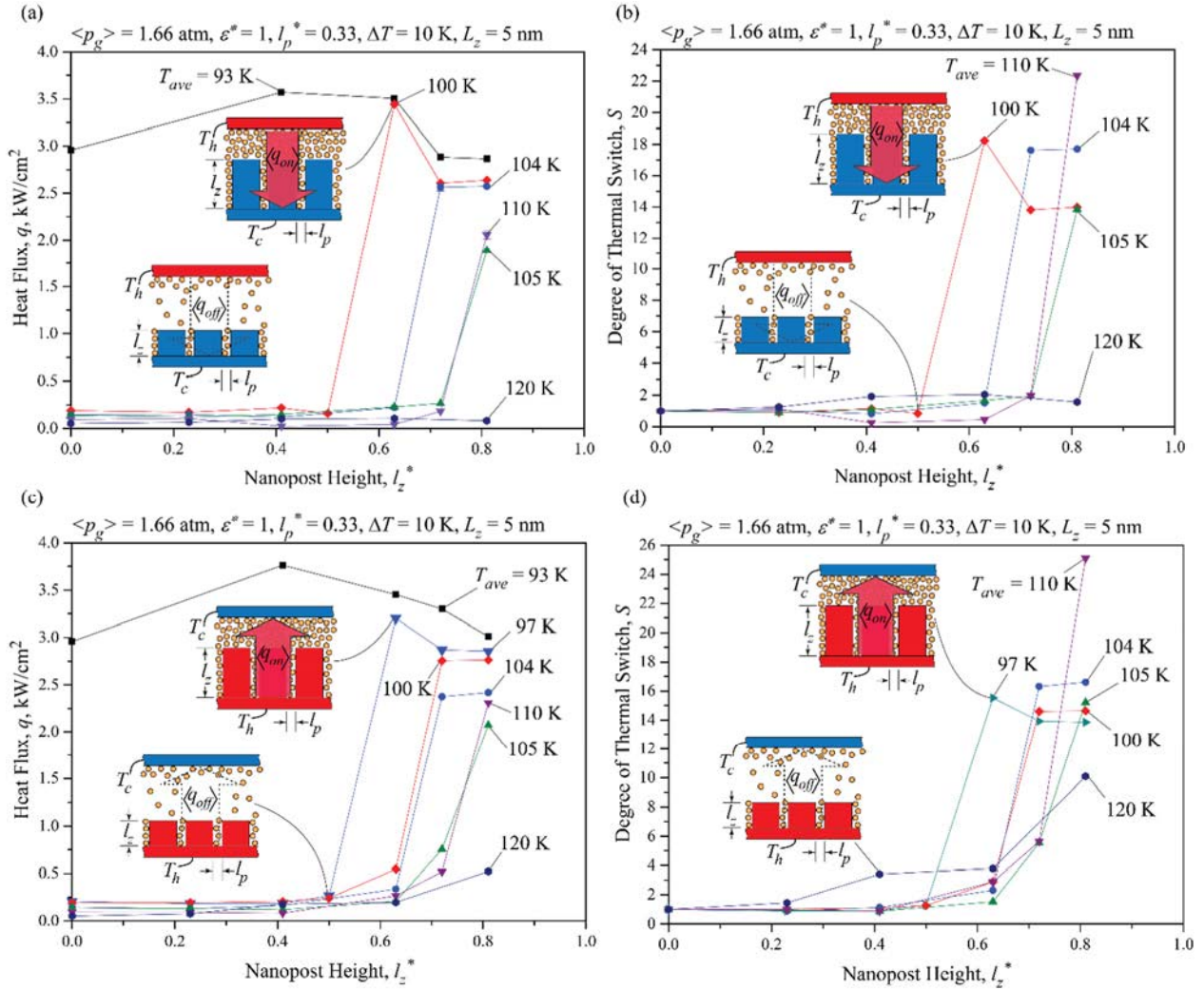


Figure 6.3. Variations of heat flux,  $q$ , and the degree of thermal switch,  $S$ , at  $T_{ave} = 93, 97, 100, 104, 105, 110,$  and  $120 \text{ K}$  as a function of the nanopost height,  $l_z^*$ . (a) Heat flux,  $q$ , and (b) degree of thermal switch,  $S$ , where the structured surface is the cold side, (c) heat flux,  $q$ , and (d) degree of thermal switch,  $S$ , where the structured surface is the hot side. Insets correspond to nanogaps having nanoposts on one surface only. Error bars are too small to be observed.

Note that the heat flux across the nanogap is calculated only through Ar, excluding the conduction through the Pt nanoposts in this study. The nanoposts increase the effective surface area at the interface between Ar and Pt nanoposts, which in turn results in increasing the heat flux by decreasing the thermal contact/boundary resistances.

Figure 6.3(b) shows the variations of the degree of the thermal switch,  $S$ , which is calculated using Eq. (1.3), i.e., ratio of  $q_{on}$  for the heat flux with different nanopost height to  $q_{off}$  for the heat

flux with bare surface. No thermal switching is observed for temperatures lower than 97 K (capillary state and high magnitude of heat flux for all heights of  $l_z^*$ ) and higher than 110 K (adsorption state and low magnitude of heat flux for all magnitudes of  $l_z^*$ ). For temperatures in between, the thermal switch is turned on by reaching  $l_z^* = 0.63$  at 100 K ( $S \sim 18$ ), 0.72 at 104 K ( $S \sim 18$ ), and 0.81 at 105 and 110 K ( $S \sim 14$  and 22, respectively).

To further understand the effects of the temperature gradient direction across the nanogap with heterogeneous (asymmetric) nanostructure on the heat flux and resulting thermal switch, the temperature gradient is reversed, i.e., nanostructures are on the hot side, and the calculations on the heat flux and degree of thermal switch are repeated. Figure 6.3(c) shows the variations of the heat flux between the nanogap surfaces when the nanoposts gradually enter the nanogap at different nanogap average temperatures,  $T_{ave}$ , for  $\Delta T = 10$  K. Here, the results are similar to those given in Figure 6.3(a). The reason is that for a small temperature gradient of 10 K, the average fluid temperature does not change significantly with reversing the temperature gradient between the nanostructured and bare surfaces. However, as shown in Figure 6.3(c), the capillary transition occurs at a higher nanopost height for  $T_{ave} = 100$  K. A larger solid-fluid interface is provided on the structured side compared to the bare side of the nanogap. As a result, the minimal increase in fluid temperature compared to the case of  $T_{ave} = 100$  K with the nanostructures on the cold side prevents the capillary condensation, and the heat flux still remains low for the nanogap at  $T_{ave} = 100$  K when the nanostructures are on the hot side.

Figure 6.3(d) shows the variation of the degree of the thermal switch,  $S$ , with respect to different nanopost heights at the given temperatures with  $\Delta T = 10$  K and the nanostructures on the hot side. Since the heat flux is nearly the same for the reversed temperature gradient, the degree of thermal switch results shown in Figure 6.3(d) are similar with the results given in Figure 6.3(b)

except at  $T_{ave} = 100$  K where the switching effect appears for  $l_z^* \geq 0.72$  instead of  $l_z^* \geq 0.63$ . The obtained results indicate that the effects of the temperature gradient direction on the thermal switch for  $\Delta T = 10$  K is minor even if the nanostructure is asymmetric. The simulation results before and after the capillary transition are repeated three times with different initial conditions, but the error bars are too small to be identified in Figure 6.3.

### 6.5.2 Nanopost pitch distance ( $l_p^*$ ) effect

Figure 6.4(a) shows the variations of the heat flux across the nanogap as a function of the dimensionless nanopost height,  $l_z^*$ , at different nanogap interpost spacings,  $l_p^* = 0.33, 0.5,$  and  $0.67$ ,  $p = 1.66$  atm,  $L_z = 5$  nm, and  $T_{ave} = 100$  K for  $\Delta T = 10$  K. As discussed in Section 6.5.1, for  $l_p^* = 0.33$ , Ar in small nanopost heights,  $l_z^* \leq 0.5$ , remains in adsorption state with low thermal conductivity and heat flux. The capillary condensation in  $l_z^* = 0.63$  results in a significantly higher heat flux due to the high liquid thermal conductivity. For  $l_p^* = 0.5$ , the heat flux predicted for  $l_z^* < 0.72$  is low, as Ar is in the adsorption state and the small gas thermal conductivity results in poor heat flux. Compared to the nanogap with  $l_p^* = 0.33$ , here the jump in the heat flux occurs for a higher nanopost height,  $l_z^* = 0.72$ , since a larger interpost spacing delays the adsorption to capillary state transition [209]. Note that the capillary transition is not observed for  $l_p^* = 0.67$  at  $T_{ave} = 100$  K and  $\langle p_g \rangle = 1.66$  atm and the heat flux magnitude is small for all heights of the nanoposts.

Figure 6.4(b) shows the variations of the degree of the thermal switch,  $S$ , as a function of the nanopost height at given interpost spacing,  $l_p^*$ , using Eq. (1.3).

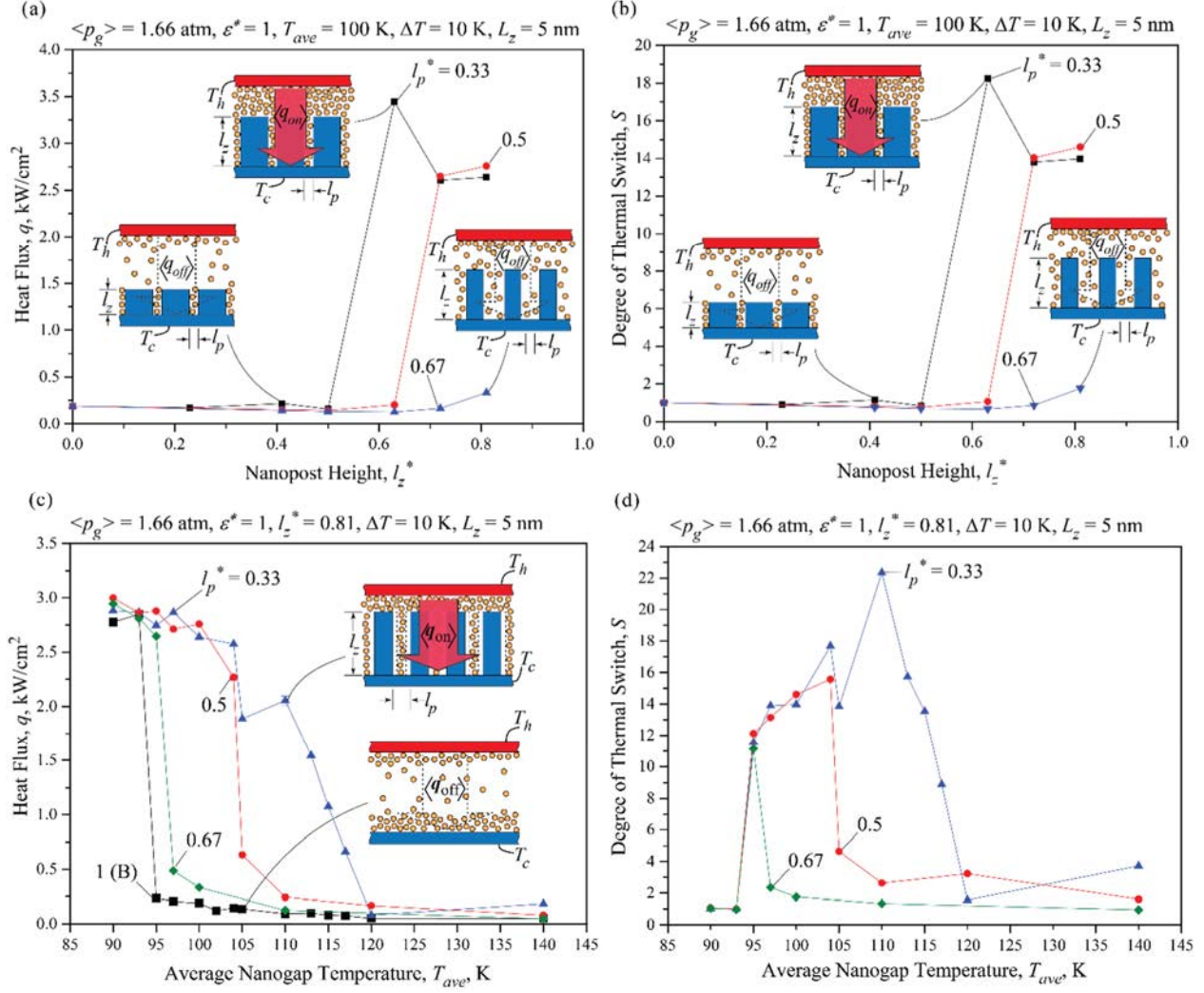


Figure 6.4. (a) Variations of heat flux,  $q$ , for  $l_p^* = 0.67, 0.5$ , and  $0.33$  as a function of the nanopost height,  $l_z^*$ , at  $T_{ave} = 100 \text{ K}$ . (b) Variations of the degree of thermal switch,  $S$ , for  $l_p^* = 0.67, 0.5$ , and  $0.33$  as a function of the nanopost height,  $l_z^*$ , at  $T_{ave} = 100 \text{ K}$ . (c) Variations of heat flux,  $q$ , for  $l_p^* = 1, 0.67, 0.5$ , and  $0.33$  as a function of the average nanogap temperature,  $T_{ave}$ , at  $l_z^* = 0.81$ . (d) Variations of the degree of thermal switch,  $S$ , for  $l_p^* = 1, 0.67, 0.5$ , and  $0.33$  as a function of the average nanogap temperature,  $T_{ave}$ , at  $l_z^* = 0.81$ . Insets correspond to nanogaps having nanoposts on one surface only. Error bars are too small to be observed.

As discussed in Section 6.5.1,  $S_{max} \sim 18$  is achieved for  $l_p^* = 0.33$  and  $l_z^* = 0.63$ . Switching effect is observed for the nanogap with  $l_p^* = 0.5$  at nanopost heights of  $l_z^* \geq 0.72$  and  $S_{max} \sim 14$  due to the large difference in the heat flux before and after capillary condensation in the nanogap. As small heat flux is predicted for  $l_p^* = 0.67$ , such a wide space among the nanoposts does not allow

for thermal switching at  $T_{ave} = 100$  K. Another conclusion from Figure 6.4(b) is that at  $T_{ave} = 100$  K,  $l_z^* > 0.5$  is required to achieve capillary-driven thermal switching.

Since the degree of thermal switch is also strongly dependent on the operating temperature, Figure 6.4(c) shows the variations of the heat flux across the nanogap surfaces as a function of the average nanogap temperature,  $T_{ave}$ . This also shows the different nanogap interpost spacing effects,  $l_p^* = 0.33, 0.5, 0.67$ , and 1 (bare surfaces) for the nanostructured surface with  $p = 1.66$  atm,  $L_z = 5$  nm, and  $l_z^* = 0.81$ .

For  $l_p^* = 0.33$ , Ar in the average nanogap temperatures,  $T_{ave}$ , below 110 K is in capillary (liquid-like) state, and the resulting heat flux is high because of the high thermal conductivity of liquid Ar. As the average nanogap temperature increases from  $T_{ave} = 110$  to 120 K, the heat flux decreases gradually as the capillary transition does not occur suddenly. This is caused by the fact that the Ar number density gradually decreases by increasing the temperature until they reach a gaseous state at  $T_{ave} = 120$  K, especially for the Ar in the interpost spacings. For  $l_p^* = 0.5$ , the switching occurs at a lower average nanogap temperature,  $T_{ave} = 104$  K, since a larger interpost spacing results in lowering the capillary transition temperature [209]. Unlike the nanogaps with  $l_p^* = 0.33$ , here the capillary evaporation occurs suddenly with respect to the small temperature change from  $T_{ave} = 104$  to 105 K. For  $l_p^* = 0.67$ , the heat flux variation by average temperature is similar to that of the bare surface, i.e.,  $l_p^* = 1$ , due to the similar adsorption isobar, i.e., interpost spacing effects of nanoposts on the adsorption isobar is negligibly small at  $l_p^* > 0.67$  [209].

To understand the switch operating temperature window for  $l_p^* = 0.33, 0.5$ , and  $0.67$ , the degree of thermal switch,  $S$ , is calculated as a function of operating temperature using Eq. (1.3), with  $q_{on}$  for the heat flux when  $l_z^* \geq 0$  and  $q_{off}$  for the heat flux when  $l_z^* = 0$  as shown in Figure 6.4(d). At temperatures below 95 K, the high heat flux are predicted and Ar is in capillary state regardless of

the existence of the nanoposts in the nanogap. This in turn results in no thermal switching effect. The  $S$  variation is almost the same for the ones with  $l_p^* = 0.33$  and  $0.5$  at the range  $95 \text{ K} \leq T_{ave} \leq 105 \text{ K}$ . However, for  $l_p^* = 0.5$ , it suddenly decreases at  $T_{ave} > 105 \text{ K}$  due to the sudden evaporation, while for  $l_p^* = 0.33$ , it continues increasing up to  $S_{max} \sim 23$  followed by the gradual decrease due to progressive evaporation until it reaches  $T_{ave} = 120 \text{ K}$ . This indicates that the design with  $l_p^* = 0.5$  provides a narrower thermal switch operating window width,  $10 \text{ K}$ , with the sudden switching mechanism. However, with  $l_p^* = 0.33$ , a wider thermal switch operating window width,  $20 \text{ K}$ , is achieved with the gradual switching mechanism. For  $l_p^* = 0.67$ ,  $S$  has a peak at  $T_{ave} = 95 \text{ K}$  with a very narrow temperature operating window width meaning that  $l_p^* = 0.67$  is challenging to produce thermal switching for a wide average nanogap temperature range, as the “switching operation window”. The results before and after the capillary transition are repeated three times with different initial conditions, but the error bars are too small to be identifiable in Figure 6.4.

### 6.5.3 Surface interaction ( $\varepsilon^*$ ) effect

Figure 6.5(a) shows the variations of the heat flux across the nanogap surfaces as a function of the dimensionless nanopost height,  $l_z^*$ , at different solid-fluid interactions, i.e., different solid materials, represented by  $\varepsilon^* = 0.5, 1, \text{ and } 2$  at  $p = 1.66 \text{ atm}$ ,  $l_z^* = 0.33$ ,  $L_z = 5 \text{ nm}$ , and  $T_{ave} = 100 \text{ K}$  for  $\Delta T = 10 \text{ K}$ . For  $\varepsilon^* = 1$  (see the details in Section 6.5.1), the small nanopost height,  $l_z^* \leq 0.50$ , results in a low heat flux,  $q \sim 0.16 \text{ kW/cm}^2$ , since it is in the adsorption state. However, a larger nanopost height,  $l_z^* > 0.5$ , allows for the capillary transition, thereby much higher heat flux,  $q \sim 3.5 \text{ kW/cm}^2$ .

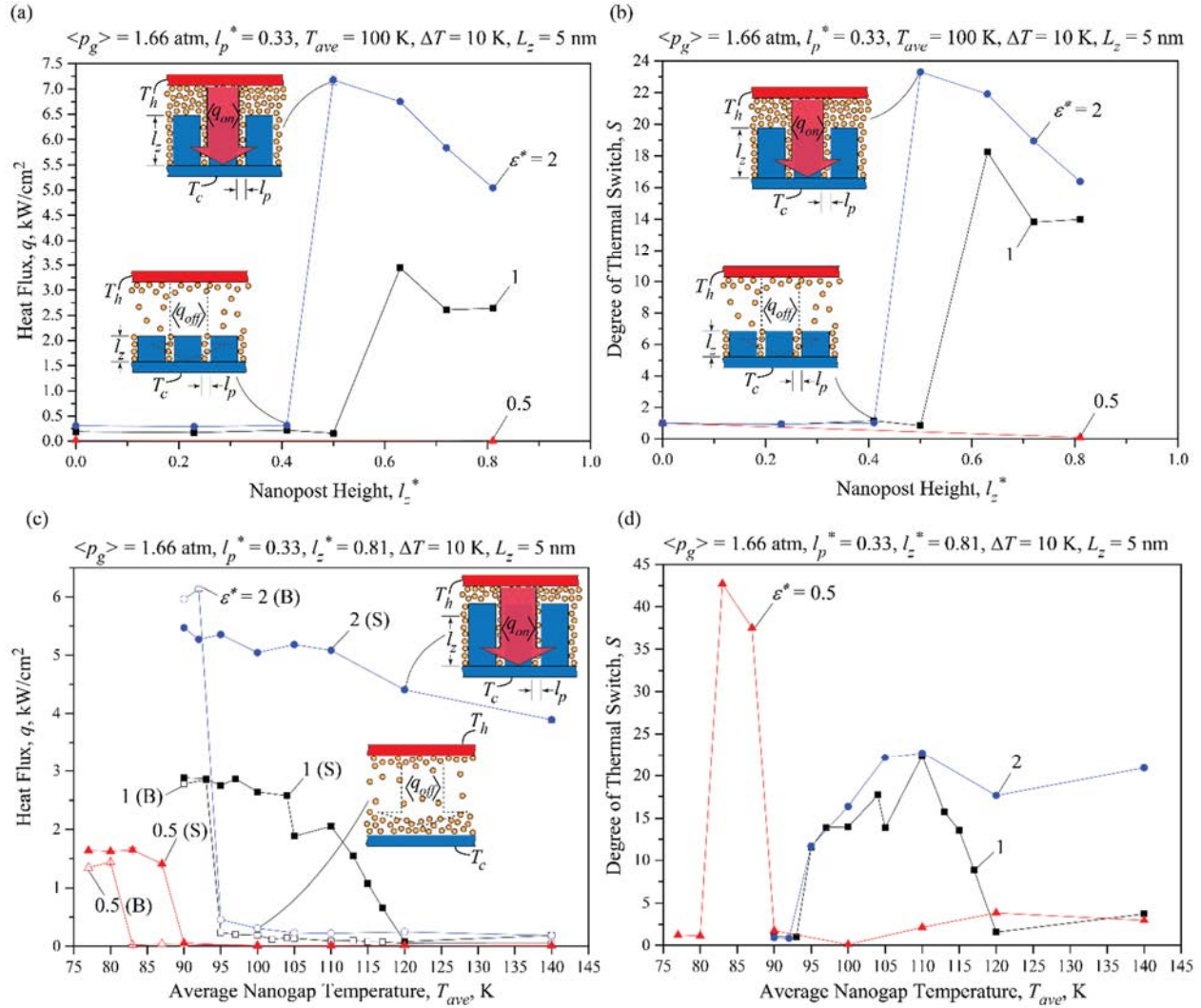


Figure 6.5. (a) Variations of heat flux,  $q$ , for  $\epsilon^* = 0.5, 1$ , and  $2$  as a function of the dimensionless nanopost height,  $l_z^*$ , at  $l_p^* = 0.33$  and  $T_{ave} = 100$  K. (b) Variations of the degree of thermal switch,  $S$ , for  $\epsilon^* = 0.5, 1$ , and  $2$  as a function of the nanopost height,  $l_z^*$ , at  $l_p^* = 0.33$  and  $T_{ave} = 100$  K. (c) Variations of heat flux,  $q$ , for  $\epsilon^* = 0.5, 1$ , and  $2$  as a function of the average nanogap temperature,  $T_{ave}$ , at  $l_p^* = 0.33$  and  $l_z^* = 0.81$ . (d) Variations of the degree of thermal switch,  $S$ , for  $\epsilon^* = 0.5, 1$ , and  $2$  as a function of the average nanogap temperature,  $T_{ave}$ , at  $l_p^* = 0.33$  and  $l_z^* = 0.81$ . Insets illustrate nanogaps with bare surfaces and nanogaps having nanoposts on one surface only. Error bars are too small to be observed.

For  $\epsilon^* = 0.5$  at  $T_{ave} = 100$  K, the Ar remains in gaseous state and the heat flux is small,  $q < 0.02$  W/cm<sup>2</sup>, for the entire range of  $l_z^*$  varying from 0 to 0.81. This very small heat flux is caused by the fact that the weak interaction between the solid and fluid particles does not allow for the capillary transition, i.e., only adsorption state, resulting in low gas thermal conductivity. Moreover, the weak

solid-fluid interaction results in a poor interfacial heat transfer between the solid and fluid particles due to the small TAC [207] even with high nanopost height  $l_z^* = 0.81$ . For  $\varepsilon^* = 2$ , the low heat flux is observed for  $l_z^* \leq 0.41$  as the Ar remains in the gaseous state with low gas thermal conductivity, i.e. adsorption state, but the heat flux is higher than those with  $\varepsilon^* = 1$ . The higher heat flux is attributed to higher interfacial heat transfer between the solid and fluid particles, i.e., higher TAC, due to the stronger solid-fluid interactions [207]. A sudden heat flux jump from  $q = 0.3 \text{ kW/cm}^2$  to  $q = 7.2 \text{ kW/cm}^2$  is found when the nanopost height increases to  $l_z^* = 0.5$ . This heat flux jump is related to the capillary transition at  $l_z^* = 0.5$  where the nanoposts promote the capillary transition by reducing the effective nanogap size. The increased solid-fluid interaction from  $\varepsilon^* = 1$  to 2 results in the early heat flux jump at reduced nanopost heights from  $l_z^* = 0.5$  to 0.41 due to the early capillary transition. Also, the higher peak heat flux from  $q = 3.5 \text{ kW/cm}^2$  to  $7.2 \text{ kW/cm}^2$  due to a higher energy exchange between the solid and fluid particles both on the source and the sink side of the nanogap.

A further increase in the nanopost height gradually decreases the heat flux from  $q \sim 7$  to  $q \sim 5 \text{ kW/cm}^2$  due to reduced Ar number density resulting from increased Ar-empty regions near the nanopost surfaces (strong repulsive forces near the nanoposts prevent from Ar occupation).

Figure 6.5(b) shows the variations of the degree of the thermal switch,  $S$ , with respect to the nanopost height at given solid-fluid interaction,  $\varepsilon^*$ . The  $S$  is determined using Eq. (1.3), as the ratio of the heat flux for the nanogap with nanoposts on one surface ( $q_{on}$ ) to the heat flux through the nanogap with bare surfaces ( $q_{off}$ ). As the heat flux for  $\varepsilon^* = 0.5$  is always in gaseous state regardless of  $l_z^*$ , no thermal switching is achieved with such a low solid-fluid interaction at  $T_{ave} = 100 \text{ K}$ . For  $\varepsilon^* = 1.0$ ,  $S \sim 1$  is achieved before the capillary transition occurs and jumps to  $S \sim 18$  at  $l_z^* = 0.63$ , as the thermal conductivity of Ar in capillary state is close to liquid state and the fluid particles

exchanges considerably more heat flux between the nanogap. The jump from  $S \sim 1$  to higher values for  $\varepsilon^* = 2$  at  $T_{ave} = 100$  K is observed for shorter nanoposts ( $l_z^* = 0.50$ ). The  $S_{max} \sim 23$  is achieved for  $\varepsilon^* = 2$  at  $l_z^* = 0.50$ , which is greater than  $S_{max} \sim 18$  for  $\varepsilon^* = 1$  at  $l_z^* = 0.63$ . In fact,  $S$  for  $\varepsilon^* = 2$  is higher than that for  $\varepsilon^* = 1$  at entire nanopost heights.

To further examine the effects of the operating temperatures, i.e., average nanogap temperature, on the thermal switch performance, Figure 6.5(c) shows the variations of the heat flux across the nanogap with both bare surfaces or one structured surface ( $l_p^* = 0.33$  and  $l_z^* = 0.81$ ) as a function of the average nanogap temperature,  $T_{ave}$ , for different solid-fluid interactions,  $\varepsilon^* = 0.5, 1.0,$  and  $2.0$ . For  $\varepsilon^* = 1$ , the heat flux across the bare surfaces is high,  $q = 2.7$  kW/cm<sup>2</sup>, at low average nanogap temperatures,  $T_{ave} < 95$  K, where the Ar is in capillary state for high liquid thermal conductivity (“on” mode). At  $T_{ave} = 95$  K, the capillary transition occurs, and Ar is in gaseous state for low gas thermal conductivity (“off” mode) at  $T_{ave} > 95$  K. With one structured surface ( $l_p^* = 0.33$  and  $l_z^* = 0.81$ ), the heat flux remains high at the average nanogap temperatures below 110 K, since such a low temperature allows for the capillary state for high liquid thermal conductivity (“on” mode). However, the heat flux begins to gradually decrease as the average nanogap temperature increases. However, the Ar state changes from capillary to adsorption state gas, i.e. capillary transition, until it reaches a completely gaseous state at  $T_{ave} \geq 120$  K for low gas thermal conductivity (“off” mode). This large heat flux difference between the bare and structured surface (by inserting the structured surface into the nanogap) results in a switching window of 20 K as discussed in Section 6.5.1. For  $\varepsilon^* = 0.5$ , the heat flux suddenly decreases by capillary transition for both bare and one-surface-structured nanogaps, at much lower average nanogap temperatures,  $T_{ave} = 83$  K and 90 K, respectively, and this results in a narrower switching operation window within only 7 K, compared to  $\varepsilon^* = 1$ . The weaker solid-fluid interaction not only reduces the capillary

transition temperatures [209], but also decreases the heat flux for the entire average nanogap temperatures, due to a poor interfacial heat transfer, i.e., TAC. For  $\varepsilon^* = 2$ , the heat flux across the bare surfaces becomes nearly doubled compared to  $\varepsilon^* = 1$  at low temperature,  $T_{ave} < 93$  K, primarily due to the enhanced energy exchange across the interfaces (“on” mode). However, it suddenly decreases at  $T_{ave} = 95$  K, due to the transition from the capillary to the adsorption state. In any case, it is still higher than that for  $\varepsilon^* = 1$ , due to higher TAC. For this case, the heat flux variations of the nanogap with structured surface is relatively small with respect to the average nanogap temperature without significant heat flux jump i.e.,  $q > 4$  kW/cm<sup>2</sup> for the entire temperature range (only “on” mode). This is considerably different from that with  $\varepsilon^* = 0.5$  and 1, due to larger solid-fluid interactions as discussed above.

The significantly different heat flux over the broad operating temperatures results in the large operating temperature window as a thermal switch. Figure 6.5(d) shows the variations of the degree of the thermal switch,  $S$ , as a function of the average nanogap temperature,  $T_{ave}$  for  $\varepsilon^* = 0.5$ , 1.0, and 2.0, to further examine the thermal switch. It remains in capillary states regardless of the nanoposts at low temperatures, i.e.,  $T_{ave} < 83$  K for  $\varepsilon^* = 0.5$  and  $T_{ave} < 95$  K for  $\varepsilon^* = 1$  and 2 or in adsorption state at high temperatures, i.e.,  $T_{ave} > 87$  K for  $\varepsilon^* = 0.5$  and  $T_{ave} > 120$  K for  $\varepsilon^* = 1$ , which do not allow for a thermal switch. For  $\varepsilon^* = 1$ ,  $10 < S < 25$  is observed between 93 K and 117 K, while the  $S$  is low below 95 K and above 115 K, i.e., no significant switching effect. For  $\varepsilon^* = 0.5$ ,  $S \sim 40$  at  $80 < T_{ave} < 90$  K, since it requires a comparatively lower temperature to create the heat flux variations by nanopost-driven capillary transition. On one hand, the weak solid-surface interaction ( $\varepsilon^* = 0.5$ ) does not allow for the large difference between the bare ( $l_z^* = 0$ ) and structured surface ( $l_z^* = 0.81$ ), which limits the operating temperature window only between 83 K and 90 K, i.e.,  $\Delta T \sim 7$  K. On the other hand, the very low heat flux in adsorption state due to the low TAC

results in very high degrees of thermal switch,  $S_{max} \sim 45$  in this narrow switching window. Note that below 83 K, there is no thermal switch effect as both bare and structured surfaces operate at high heat flux (“on” mode). For  $\varepsilon^* = 2$ ,  $S \sim 20$  is achieved at  $T_{ave} > 95$  K by effectively controlling the heat flux via the capillary transition through the nanopost height between the bare and structured surfaces. This indicates that the strong solid-fluid interaction increases the sensitivity of the heat flux control by capillary transition to the thermal switch operation over a larger operating temperature window. Note that below 95 K, the thermal switch effect is minimal as both bare and structured surfaces operate at high heat flux (“on” mode). The simulation results before and after the capillary transition are repeated three times with different initial conditions, but the error bars are so small and cannot be clearly observed in Figure 6.5.

#### 6.5.4 Temperature difference ( $\Delta T$ ) effect

To further examine the effects of the heat flux direction and temperature difference across the nanogap on the thermal switch, three different cases are studied, namely the nanogap with both bare surfaces, nanogap with the structured surface as the hot side (heat source), and nanogap with the structured surface as the cold side (heat sink) at  $p = 1.66$  atm,  $L_z = 5$  nm,  $l_p^* = 0.33$ ,  $l_z^* = 0.81$ , and  $\varepsilon^* = 1$ . Figure 6.6(a) shows the variations of the heat flux across the nanogap surfaces as a function of the hot side temperature up to 140 K, while maintaining the cold side temperature at 80 K. For small temperature difference,  $\Delta T < 20$  K, the heat flux difference among the three cases is minimal due to the fact that Ar is in capillary (liquid-like) state with high thermal conductivity in all of them. However, for  $\Delta T = 30$  K, the heat flux for the nanogap with both bare surfaces begins to decrease down to  $q \sim 0.26$  W/cm<sup>2</sup>, as a result of Ar capillary transition and low gas thermal conductivity. For the nanogap with the hot surface structured, the existence of the nanoposts maintains high heat flux reaching a maximum of  $q \sim 6$  kW/cm<sup>2</sup> at  $\Delta T = 30$  K, followed

by the gradual decrease down to  $q \sim 1 \text{ kW/cm}^2$  at  $\Delta T = 60 \text{ K}$ , due to the capillary transition at higher temperatures.

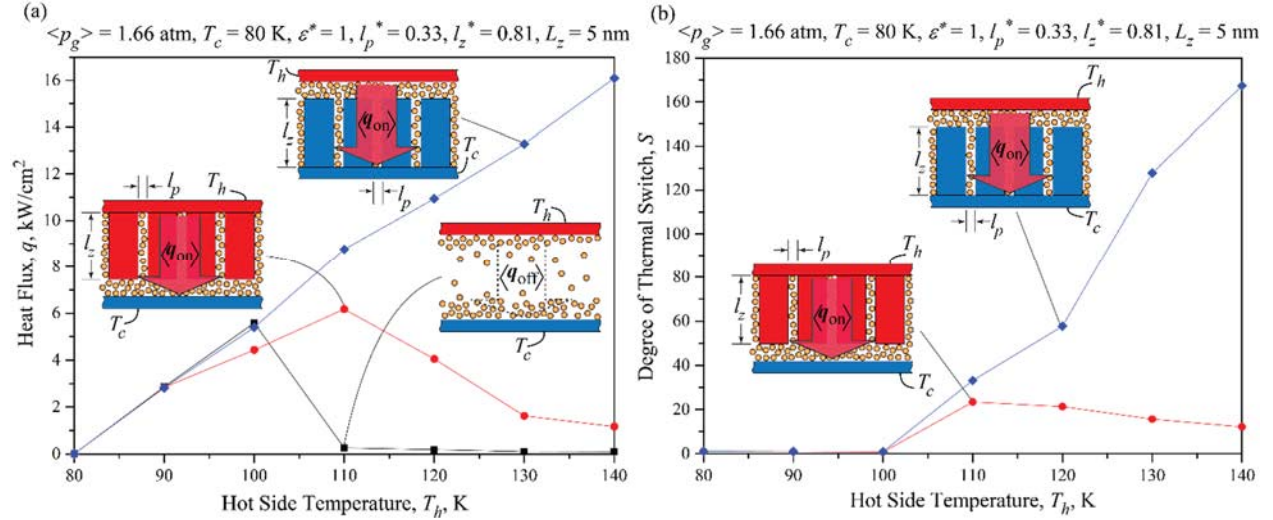


Figure 6.6. Variations of (a) heat flux,  $q$ , and (b) the degree of thermal switch,  $S$ , through the nanogap for  $T_c = 80 \text{ K}$ ,  $l_p^* = 0.33$ , and  $l_z^* = 0.81$  as a function of the hot surface temperature,  $T_h$ . Insets correspond to nanogaps with bare surfaces and nanogaps having nanoposts on one surface only.

However, the heat flux for the nanogap with the cold structured surface proportionally increases as the temperature difference increases up to  $q \sim 16 \text{ kW/cm}^2$  at  $\Delta T = 60 \text{ K}$ , while maintaining capillary state even at  $T_h = 140 \text{ K}$ . The persistent capillary state stems from the dominant energy exchange effect between the Ar and structured surface over that between the Ar and bare surface, i.e., the temperature of the Ar remains close to the cold surface due to the larger surface interaction with the structured surface.

Figure 6.6(b) shows the predicted degree of thermal switch,  $S$ , as a function of the hot side temperature for all three cases.  $S$  is calculated using the ratio of the heat flux with the structured surface ( $q_{on}$ ) to the bare surface ( $q_{off}$ ). Figure 6.6(b) shows minimal  $S$  at low  $T_h$ . The higher structured surface temperature case results in  $S_{max} \sim 25$  at  $\Delta T = 30 \text{ K}$ , but for the lower structured surface temperature,  $S$  continues to increase up to  $S_{max} \sim 170$  due to lack of the capillary transition.

## 6.6 Conclusion

In this study, the adsorption-capillary-transition-controlled thermal switch mechanism is examined using the Ar gas-filled movable heterogeneous nanostructure (nanogap having movable nanoposts on one side only) along with GCMC and NEMD simulations. It is found that a key thermal switch mechanism is associated with a significant thermal conductivity contrast between the gas (adsorption only) and liquid (capillary) states, controlled by the nanopost heights, interspacing, and gas-solid interaction.

The predicted results show that the higher operating temperature results in the larger nanopost height for the switch “on” mode for  $T_{ave} = 100$  to 120 K, but no thermal switching is achieved for the entire nanopost heights below 100 K due to capillary state from the low temperature at  $\langle p_g \rangle = 1.66$  atm,  $\varepsilon^* = 1.0$ ,  $l_p^* = 0.33$ ,  $\Delta T = 10$  K, and  $L_z = 5$  nm. The results also show that the reversing temperature gradient direction across the nanogap does not significantly change the switching effect for small temperature difference,  $\Delta T = 10$  K. A small interpost spacing,  $l_p^* \leq 0.5$ , is required to provide the thermal switching, and the smaller interpost spacing needs the smaller nanopost height to operate the thermal switch. The higher degrees of thermal switch,  $S$ , and wider switching operation windows are observed with higher  $l_z^*$  and smaller  $l_p^*$ . A solid-fluid interaction higher than that of Ar-Pt ( $\varepsilon^* = 1.0$ ) widens the switching operation window from  $\sim 20$  K (for  $\varepsilon^* = 1.0$ ) to  $\sim 45$  K (for  $\varepsilon^* = 2.0$ ) such that  $S \sim 20$  is achievable at average temperatures as high as 140 K for  $\varepsilon^* = 2.0$ . A weak surface interaction results in a considerably low heat flux and narrow operating window,  $\sim 7$  K, but relatively high degrees of thermal switch,  $S_{max} \sim 45$ , at  $T_{ave} = 83$  K. For large temperature difference,  $\Delta T > 20$  K, between the nanogap surfaces, the fluid capillary transition temperature, heat flux, and  $S$  are dominantly controlled by the structured surface temperature. The  $S_{max} \sim 25$  at  $\Delta T = 30$  K is achieved when the nanoposts enter the hot side of the nanogap and  $S$

decreases by further increase in  $\Delta T$ . When the nanoposts enter the cold side,  $S$  gradually increases to  $S_{max} \sim 170$  given providing  $\Delta T = 60$  K is achievable.

Although the capillary-transition-driven thermal switch mechanism is demonstrated using Ar in Pt-based nanostructures at the cryogenic temperature, the working principle would be valid for different condensable gas, e.g., water, when it is operated at the temperature between the melting and critical temperature at given pressure. This result can be synergetically integrated into a recent adsorption-controlled thermal diode [207] for designing advanced thermal management systems, i.e., thermal logic gates.

## CHAPTER 7

### CONCLUSION

#### 7.1 Contributions

This study fundamentally examines the tailored nanoscale thermal transport through gas-filled heterogeneous nanostructures using NEMD and GCMC simulations, to develop novel thermal management systems such as thermal diodes and thermal switches. The temperature-dependent asymmetric adsorption in condensable gas-filled heterogeneous nanostructures leads to the controlled nanoscale thermal transport via asymmetric gas pressure TACs, resulting in the design of adsorption-controlled thermal diodes and switches. Controlling capillary transition in heterogeneous nanostructures also leads to design thermal switches with high degrees of thermal switching,  $S$ , and thermal diodes with high degrees of thermal rectification,  $R$ .

Key contributions of this work are summarized below:

- ***Development of adsorption-controlled thermal diode in heterogeneous nanostructures:***  
the adsorption-controlled thermal diode is examined using the Ar-gas-filled heterogeneous nanogap. It is found that a maximum degree of rectification,  $R_{max} \sim 7$  is predicted for  $\epsilon^* = 0.75$  at  $T = 80$  K. For  $\epsilon^* = 0.75$ , the thermal diode is originated by the combination of the adsorption-controlled asymmetric gas pressure and TACs, while for  $\epsilon^* = 0.5$ , it is dominantly controlled by the asymmetric gas pressure. The obtained results for the Ar-filled Pt-based nanogap with the tailored materials provides a design guideline for the thermal diode using real materials.  $\epsilon^* = 0.75$  and  $0.5$  can be designed using Pt/Ni and Pt/Al as strong/weak surfaces based on the LJ potential in literature, respectively.
- ***Development of adsorption-controlled thermal switch in heterogeneous nanostructures:***  
the adsorption-controlled thermal switch is investigated using Ar gas-filled nanostructures

(two nanogaps) with heterogeneous solid-gas interactions, using NEMD. The maximum degree of the thermal switch,  $S_{max} \sim 13$ , can be achieved at  $T_3 = 110$  K (middle plate temperature) under  $T_1 = 100$  K and  $T_2 = 80$  K (the lower and upper plate temperatures), which is controlled by a weak surface interaction plate ( $\varepsilon^* = 0.4$ ) between two stronger plates ( $\varepsilon^* = 1.0$ ). The efficiency of the thermal switch can be further improved by using optimal material selections and nanostructure geometries to further decrease the TAC.

- ***Investigation of the adsorption and capillary transition in heterogeneous nanostructures:*** the adsorption and adsorption-capillary transition is fundamentally studied for Ar-filled Pt-based nanogaps having one surface with nanoposts using the GCMC simulations. The adsorption-capillary transition pressure decreases at given temperature (or the transition temperature increases at given pressure), by increasing the nanopost height,  $l_z$ , decreasing the nanopost gap size,  $l_p$ , and increasing the solid-fluid interatomic potential,  $\varepsilon_{sf}$ . It is also observed that the stronger gas-solid interaction effectively reduces the capillary transition pressure and increases the adsorption isotherm with the inclusion of nanoposts. For the bare surfaces, the doubled nanogap size shows no apparent size-effect, whereas for the nanogaps with nanoposts, the second capillary transition pressure increases. The nanoposts also reduce the hysteresis compared to the bare surfaces.
- ***Development of capillary-controlled thermal diode in heterogeneous nanostructures:*** Asymmetric heat flux through the nanogaps with structural and/or material heterogeneity are examined, aiming at developing the compact and efficient adsorption-capillary-transition-controlled thermal diode using GCMC and NEMD simulations. The highly efficient thermal diode,  $R_{max} = 140$  is achieved by the significant thermal conductivity

contrast between the gas (adsorption only) and liquid (capillary) states without significant hysteresis. Homogeneous nanopores (nanogap with both bare surfaces and same solid materials) result in a significant hysteresis in capillary transition. Nanoposts on one surface only ( $l_z^* = 0.23, 0.41, \text{ and } 0.63$ ) minimize the hysteresis, which enables the thermal diode operate without additional temperature controllers. Moreover, the nanogaps decrease the absolute surface temperature difference,  $|\Delta T|$ , for the thermal diode activation. The minimal hysteresis in capillary transition is equivalently achieved by employing a weaker fluid-surface interaction only on the lower surface without nanopillars,  $\varepsilon_l^* = 0.6$ , i.e., material heterogeneity, showing  $R_{max} \sim 85$ , but at the reduced heat flux due to the lower solid-fluid interaction (larger interfacial resistance). Employing a weaker fluid-surface interaction only on the upper surface with nanopillars (coupled structural and material heterogeneity) results in  $R \sim 120$  without reducing the heat flux.

- ***Development of capillary-controlled thermal switch in heterogeneous nanostructures:*** A thermal switch mechanism is fundamentally investigated using the significant thermal conductivity contrast between the gas (adsorption only) and liquid (capillary) states, controlled by the nanopost heights, interspacing, and gas-solid interaction. A small interpost spacing,  $l_p^* \leq 0.5$ , is required to provide the thermal switching, and the smaller interpost spacing needs the smaller nanopost height to operate the thermal switch. Higher degrees of thermal switch,  $S$ , and wider switching operation windows are observed with higher  $l_z^*$  and smaller  $l_p^*$ . A solid-fluid interaction higher than that of Ar-Pt ( $\varepsilon^* = 1.0$ ) widens the switching operation window from  $\sim 20$  K (for  $\varepsilon^* = 1.0$ ) to  $\sim 45$  K (for  $\varepsilon^* = 2.0$ ) such that  $S \sim 20$  is achievable at average temperatures as high as 140 K for  $\varepsilon^* = 2.0$ . A weak surface interaction results in a considerably low heat flux and narrow operating window,  $\sim$

7 K, but relatively high degrees of thermal switch,  $S_{max} \sim 45$ , at  $T_{ave} = 83$  K. For large temperature difference,  $\Delta T > 20$  K, between the nanogap surfaces, the fluid temperature, heat flux, and  $S$  are dominantly controlled by the structured surface temperature. When the nanoposts enter the cold side,  $S$  gradually increases to  $S_{max} \sim 170$  given providing  $\Delta T = 60$  K is achievable.

Although these mechanisms are demonstrated using Ar in Pt-based nanostructures at cryogenic temperatures, the working principle would be valid for a different condensable gas, e.g., water, when it is operated at the appropriately selected temperature and pressure range. These mechanisms can be synergetically integrated to design advanced thermal management systems, i.e., thermal logic gates.

## 7.2 Proposed future work

There are three extensions of the current study that can be pursued:

**1:** Understanding the roles of nanoposts for enhanced degree of thermal diode,  $R$ , in the adsorption-controlled thermal diode.

The roles of the nanostructures, i.e., nanoposts, on the degree of the thermal diode can be examined. Adding nanoposts over the strong surface of the thermal diode discussed in chapter 2 may not affect the heat flux magnitude in positive direction much. However, a nanostructured surface with stronger surface interaction and lower temperature can adsorb much more fluid particles compared to a bare surface with weak surface interaction and high temperature. This may considerably decrease the heat flux magnitude in negative direction, i.e., a higher amount of  $R$ . GCMC along with NEMD simulations can be used to find the optimum pressure to increase the degree of thermal diode,  $R$ .

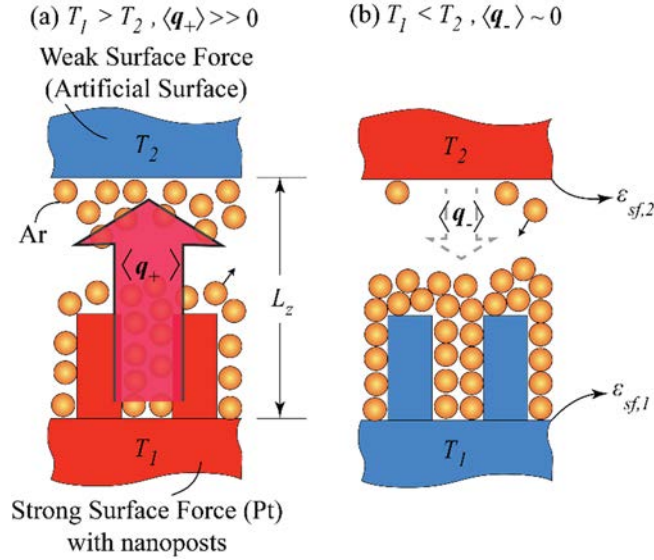


Figure 7.1. A schematic of the adsorption-controlled thermal diode with nanostructured strong surface. (a)  $\langle q_+ \rangle \gg 0$  for  $T_1 > T_2$ , and (b)  $\langle q_- \rangle \sim 0$  for  $T_1 < T_2$  due to the adsorption-controlled asymmetric isotherm and thermal accommodation coefficient (TAC). The surface temperatures,  $T_1$  and  $T_2$ , heat fluxes,  $\langle q_+ \rangle$ , and  $\langle q_- \rangle$ , gas-solid interactions,  $\epsilon_{sf,1}$  and  $\epsilon_{sf,2}$ , nanogap size,  $L_z$ , and the adsorbed particles are also shown.

**2:** Understanding the effect of nanoposts for enhanced degree of thermal switch,  $S$ , in the adsorption-controlled thermal switch.

The nanoscale, switchable thermal transport phenomena can be examined assisted by the nanostructures, i.e., nanoposts. Adding nanoposts over the high temperature strong surface of the thermal switch discussed in chapter 3 may not considerably affect the heat flux magnitude from the lower surface to the middle surface when the switch is on. However, a nanostructured surface with stronger surface interaction and lower temperature (lower plate when the switch is off) can adsorb much more fluid particles compared to a bare surface with weak surface interaction and high temperature (middle plate when the switch is off). This may considerably decrease the heat flux magnitude in the nanogap at the bottom, i.e., a higher degree of thermal switching,  $S$ . GCMC along with NEMD simulations can be used to find the optimum pressure in the lower and upper nanogaps to increase the degree of thermal switch,  $S$ .

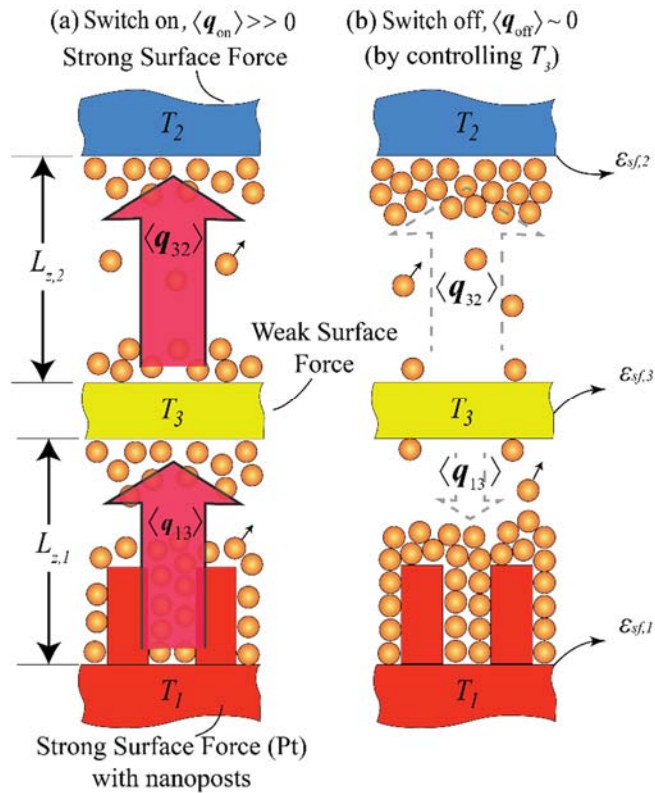


Figure 7.2. A schematic of the adsorption-controlled thermal switch with nanoposts on the strong surface with the high temperature. (a) Large heat flux for “on” mode by the high thermal accommodation coefficients and (b) small heat flux for “off” mode by poor thermal accommodation coefficients (adsorption-free surface on the middle surface).

### 3: Understanding the adsorption-capillary-transition-driven thermal transistor mechanism.

Figure 7.3 shows the schematic drawing of adsorption-capillary-controlled thermal transistor at a given pressure and temperature distribution. Here, the surface interaction between Ar and the surfaces creating the lower nanogap is weaker than the ones forming the nanogap at the top. It is assumed that the top surface is connected to a heat source and the bottom surface is connected to a heat sink.

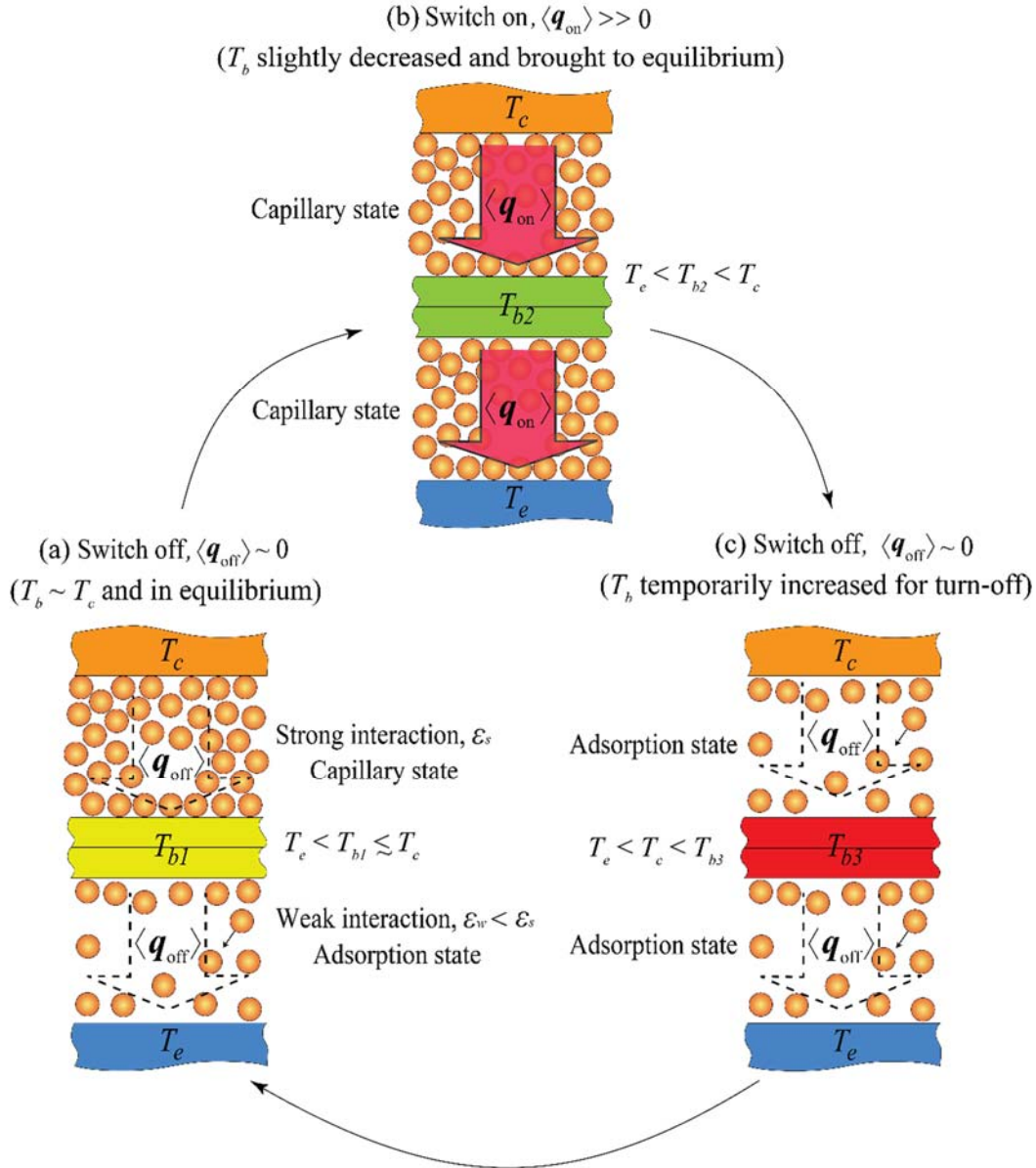


Figure 7.3. Schematic drawing of adsorption-capillary-controlled thermal transistor at given pressure and temperature distribution in a double-gap nanostructure with lower surface interaction at the bottom. (a) “Off” mode; Middle surface temperature,  $T_b$ , is close to the top surface temperature, capillary state at the top and adsorption state at the bottom of the structure. (b) “On” mode;  $T_b$  slightly decreases and Ar in the lower gap condensates as a result of capillary transition. (c) Back to “Off” mode by temporarily increasing the middle surface temperature to empty the nanogaps.

As the capillary state at the bottom is achieved at a lower temperature compared to the upper nanogap, the initial temperatures can be selected in a way that the middle surface temperature,

base temperature,  $T_b$ , is close to the top surface temperature, collector temperature,  $T_c$ , because the upper nanogap is filled with Ar particles and heat is properly transferred through the upper nanogap keeping the temperature difference between the surfaces small [Figure 7.3(a)].

Ar in the lower gap is in gaseous state because of the lower surface interaction at the lower nanogap and this results in a greater temperature difference between the middle and lower surfaces and at the same time a low heat flux because of the low thermal conductivity of gaseous Ar.

As shown in Figure 7.3(b), to turn the thermal transistor “on” one can slightly decrease  $T_b$  and as a result Ar in the lower gap condensates due to capillary transition. This helps the middle surface to reach a new thermal equilibrium state transferring heat from the source (collector) to the sink (emitter) uniformly. In order to turn the transistor “off”,  $T_b$  should temporarily increase to a temperature where capillary transition is achieved in the nanogaps and they are emptied from Ar particles, Figure 7.3(c). The nanogap will go back to the initial “off” state when the middle surface cools back to a temperature close to  $T_c$ . Preliminary study shows that  $S \sim 30$  is achievable using this inactive switching method.

### 7.3 Outlook

This study primarily focuses on the atomic-scale simulation work, to fundamentally understand the roles of the heterogeneous nanostructures/materials on the controlled thermal transport, aiming at designing thermal diode and switch. However, the anticipated results provide insights into future experimental work using the current and emerging nanotechnologies, i.e., MEMS/NEMS technology [202, 240-242] and Atomic Force Microscopy (AFM), as outlined below:

- *MEMS-based platform for generating a nanogap.* As shown in Figure 7.4, a wire heater (shown in red) attached to the heat source at the top, and an Al heat sink (shown in blue) at the bottom create the required temperature gradient [243]. Metals with different surface

interactions, e.g. Pt and Pb (shown in grey) can be deposited on a wafer (shown in green). The grooves can be generated by reactive ion etching (RIE). A spacer (shown in yellow) is used to minimize the conductive heat transfer through the nanogap at the center. At the beginning of each measurement, the wire heater can be heated by a DC power supply, and digital multi-meters can be used to measure the electrical resistances of the source and the receiver by the four-wire method. The measured resistance of the source and the receiver can then be converted to temperature and heat flux using calibration factors.

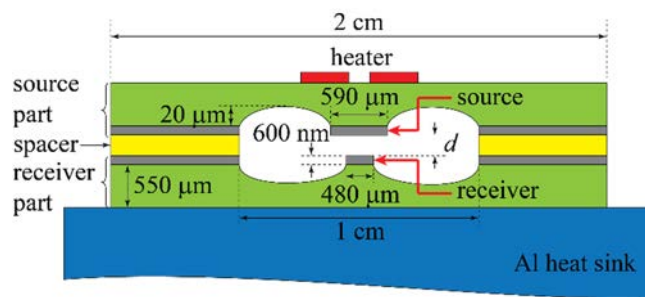


Figure 7.4. Proposed MEMS-based platform for measuring the heat flux and the degree of thermal diode,  $R$ , or switch,  $S$ , through a nanogap [243].

- *The gap between a substrate and an AFM probe.* As shown in Figure 7.5, a substrate can be coated by a metal, e.g. Pt, and the tip of the AFM probe can be coated with another metal with a weaker surface interaction, e.g. Pb. The temperature gradient can be provided by a wire heater. At the beginning of each measurement, the wire heater is heated by a DC power supply, and digital multi-meters can be used to measure the electrical resistances of the source and the receiver by the four-wire method. The measured resistance of the source and the receiver can then be converted to temperature and heat flux using calibration factors.

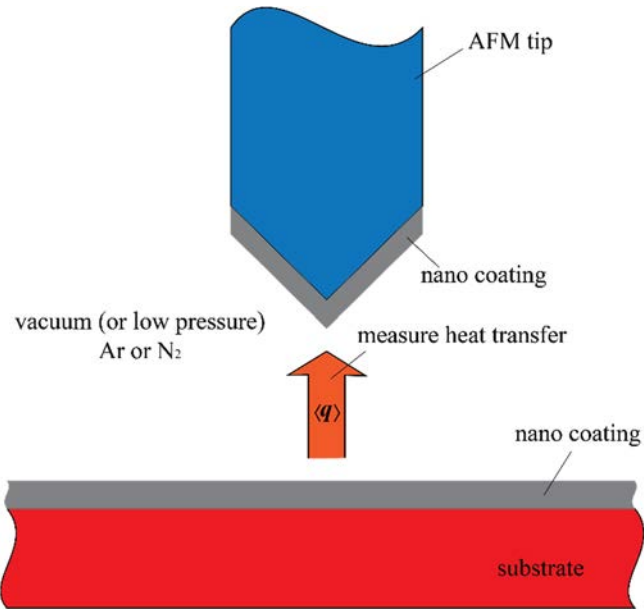


Figure 7.5. Nanogap generated with nano-coated substrate and AFM tip for measuring the heat flux and the degree of thermal diode,  $R$ , or switch,  $S$ .

## REFERENCES

## REFERENCES

- [1] J. J. Conti, P. D. Holtberg, J. R. Diefenderfer, S. A. Napolitano, A. M. Schaal, J. T. Turnure, *et al.*, "Annual Energy Outlook 2015 with Projections to 2040," U.S. Energy Information Administration 2015.
- [2] B. T. Fichman, "Estimated U.S. Energy Use in 2013," Department of Energy, Lawrence Livermore National Laboratory 2014.
- [3] A. A. Mohamad, "Integrated solar collector-storage tank system with thermal diode," *Solar Energy*, vol. 61, pp. 211-218, 9// 1997.
- [4] D. M. T. Kuo and Y.-C. Chang, "Thermoelectric and thermal rectification properties of quantum dot junctions," *Physical Review B*, vol. 81, p. 205321, 05/26/ 2010.
- [5] N. A. Roberts and D. G. Walker, "Computational study of thermal rectification from nanostructured interfaces," *Journal of Heat Transfer*, vol. 133, pp. 092401-092401, 2011.
- [6] S. Varga, A. C. Oliveira, and C. F. Afonso, "Characterisation of thermal diode panels for use in the cooling season in buildings," *Energy and Buildings*, vol. 34, pp. 227-235, 3// 2002.
- [7] L. Wang and B. Li, "Thermal Logic Gates: Computation with Phonons," *Physical Review Letters*, vol. 99, p. 177208, 10/24/ 2007.
- [8] C. W. Chang, D. Okawa, A. Majumdar, and A. Zettl, "Solid-state thermal rectifier," *Science*, vol. 314, pp. 1121-1124, November 17, 2006 2006.
- [9] G. Casati, "Device physics: The heat is on- and off," *Nature Nanotechnology*, vol. 2, pp. 23-24, 01//print 2007.
- [10] N. Li, J. Ren, L. Wang, G. Zhang, P. Hänggi, and B. Li, "Colloquium: Phononics: Manipulating heat flow with electronic analogs and beyond," *Reviews of Modern Physics*, vol. 84, pp. 1045-1066, 07/17/ 2012.
- [11] Z. Chen, C. Wong, S. Lubner, S. Yee, J. Miller, W. Jang, *et al.*, "A photon thermal diode," *Nature Communications*, vol. 5, 11/17/online 2014.
- [12] N. A. Roberts and D. G. Walker, "A review of thermal rectification observations and models in solid materials," *International Journal of Thermal Sciences*, vol. 50, pp. 648-662, 5// 2011.
- [13] D. G. Gilmore and M. Donabedian, *Spacecraft Thermal Control Handbook: Cryogenics* vol. 2: AIAA, 2003.
- [14] C. Starr, "The copper oxide rectifier," *Journal of Applied Physics*, vol. 7, pp. 15-19, 1936.

- [15] T. Ruokola and T. Ojanen, "Single-electron heat diode: Asymmetric heat transport between electronic reservoirs through Coulomb islands," *Physical Review B*, vol. 83, p. 241404, 2011.
- [16] J. Ren and J.-X. Zhu, "Anomalous energy transport across topological insulator superconductor junctions," *Physical Review B*, vol. 87, p. 165121, 2013.
- [17] M. Martínez-Pérez and F. Giazotto, "Efficient phase-tunable Josephson thermal rectifier," *Applied Physics Letters*, vol. 102, p. 182602, 2013.
- [18] D. Segal and A. Nitzan, "Spin-boson thermal rectifier," *Physical Review Letters*, vol. 94, p. 034301, 2005.
- [19] B. Hu, L. Yang, and Y. Zhang, "Asymmetric heat conduction in nonlinear lattices," *Physical Review Letters*, vol. 97, p. 124302, 2006.
- [20] D. G. Walker, "Thermal rectification mechanisms including noncontinuum effects," in *Proceedings of the Joint ASME-ISHMT Heat Transfer Conference*, IIT Guwahati, India, 2006.
- [21] X.-K. Chen, Z.-X. Xie, W.-X. Zhou, L.-M. Tang, and K.-Q. Chen, "Thermal rectification and negative differential thermal resistance behaviors in graphene/hexagonal boron nitride heterojunction," *Carbon*, 2016.
- [22] I. Carlomagno, V. Cimmelli, and D. Jou, "Computational analysis of heat rectification in composition-graded systems: From macro-to-nanoscale," *Physica B: Condensed Matter*, vol. 481, pp. 244-251, 2016.
- [23] M. Hu, J. V. Goicochea, B. Michel, and D. Poulikakos, "Thermal rectification at water/functionalized silica interfaces," *Applied Physics Letters*, vol. 95, pp. 279-285, 2009.
- [24] S. Murad and I. K. Puri, "Communication: Thermal rectification in liquids by manipulating the solid-liquid interface," *The Journal of Chemical Physics*, vol. 137, p. 081101, 2012.
- [25] F. Yuan and L. Xin-Gang, "Heat transport through a solid-liquid interface system and its thermal rectification phenomena by molecular dynamics simulations," in *ASME 2014 4th Joint US-European Fluids Engineering Division Summer Meeting and 12th International Conference on Nanochannels, Microchannels, and Minichannels*, Chicago, 2014.
- [26] B. Li, L. Wang, and G. Casati, "Thermal diode: rectification of heat flux," *Physical Review Letters*, vol. 93, p. 184301, 10/27/ 2004.
- [27] M. Terraneo, M. Peyrard, and G. Casati, "Controlling the energy flow in nonlinear lattices: a model for a thermal rectifier," *Physical Review Letters*, vol. 88, p. 094302, 02/14/ 2002.
- [28] C.-W. Chang, W.-Q. Han, and A. Zettl, "Thermal conductivity of BCN and BN nanotubes," *Journal of Vacuum Science and Technology B Microelectronics and Nanometer Structures*, vol. 23, p. 1883, 2005.

- [29] J. Hone, M. Whitney, C. Piskoti, and A. Zettl, "Thermal conductivity of single-walled carbon nanotubes," *Physical Review B*, vol. 59, p. R2514, 1999.
- [30] H. Tian, D. Xie, Y. Yang, T.-L. Ren, G. Zhang, Y.-F. Wang, *et al.*, "A novel solid-state thermal rectifier based on reduced graphene oxide," *Scientific Reports*, vol. 2, pp. 1-7, 07/23/online 2012.
- [31] J. Hu, X. Ruan, and Y. P. Chen, "Thermal conductivity and thermal rectification in graphene nanoribbons: a molecular dynamics study," *Nano Letters*, vol. 9, pp. 2730-2735, 2009/07/08 2009.
- [32] X. Ni, G. Zhang, and B. Li, "Thermal conductivity and thermal rectification in unzipped carbon nanotubes," *Journal of Physics: Condensed Matter*, vol. 23, p. 215301, 2011.
- [33] Y. Wang, S. Chen, and X. Ruan, "Tunable thermal rectification in graphene nanoribbons through defect engineering: A molecular dynamics study," *Applied Physics Letters*, vol. 100, p. 163101, 2012.
- [34] M. Alaghemandi, F. Leroy, E. Algaer, M. C. Böhm, and F. Müller-Plathe, "Thermal rectification in mass-graded nanotubes: a model approach in the framework of reverse non-equilibrium molecular dynamics simulations," *Nanotechnology*, vol. 21, p. 075704, 2010.
- [35] S. Pal and I. K. Puri, "Thermal rectification in a polymer-functionalized single-wall carbon nanotube," *Nanotechnology*, vol. 25, p. 345401, 2014.
- [36] Q. Zheng, D. Xia, Q. Xue, K. Yan, X. Gao, and Q. Li, "Computational analysis of effect of modification on the interfacial characteristics of a carbon nanotube-polyethylene composite system," *Applied Surface Science*, vol. 255, pp. 3534-3543, 2009.
- [37] S. Frankland, A. Caglar, D. Brenner, and M. Griebel, "Molecular simulation of the influence of chemical cross-links on the shear strength of carbon nanotube-polymer interfaces," *The Journal of Physical Chemistry B*, vol. 106, pp. 3046-3048, 2002.
- [38] N. G. Sahoo, S. Rana, J. W. Cho, L. Li, and S. H. Chan, "Polymer nanocomposites based on functionalized carbon nanotubes," *Progress in Polymer Science*, vol. 35, pp. 837-867, 2010.
- [39] G. Wu and B. Li, "Thermal rectification in carbon nanotube intramolecular junctions: Molecular dynamics calculations," *Physical Review B*, vol. 76, p. 085424, 08/17/ 2007.
- [40] N. Yang, G. Zhang, and B. Li, "Carbon nanocone: A promising thermal rectifier," *Applied Physics Letters*, vol. 93, p. 243111, 2008.
- [41] N. Yang, G. Zhang, and B. Li, "Thermal rectification in asymmetric graphene ribbons," *Applied Physics Letters*, vol. 95, p. 033107, 2009.
- [42] J. Jiang, J. Wang, and B. Li, "Topology-induced thermal rectification in carbon nanodevice," *Europhysics Letters*, vol. 89, p. 46005, 2010.

- [43] G. Zhang and H. Zhang, "Thermal conduction and rectification in few-layer graphene Y Junctions," *Nanoscale*, vol. 3, pp. 4604-4607, 2011.
- [44] J. Lee, V. Varshney, A. K. Roy, J. B. Ferguson, and B. L. Farmer, "Thermal rectification in three-dimensional asymmetric nanostructure," *Nano letters*, vol. 12, pp. 3491-3496, 2012.
- [45] Y. Wang, A. Vallabhaneni, J. Hu, B. Qiu, Y. P. Chen, and X. Ruan, "Phonon lateral confinement enables thermal rectification in asymmetric single-material nanostructures," *Nano Letters*, vol. 14, pp. 592-596, 2014/02/12 2014.
- [46] J. Zhu, K. Hippalgaonkar, S. Shen, K. Wang, Y. Abate, S. Lee, *et al.*, "Temperature-gated thermal rectifier for active heat flow control," *Nano letters*, vol. 14, pp. 4867-4872, 2014.
- [47] X. Cartoixà, L. Colombo, and R. Rurali, "Thermal rectification by design in telescopic Si nanowires," *Nano letters*, vol. 15, pp. 8255-8259, 2015.
- [48] Y.-Y. Liu, W.-X. Zhou, and K.-Q. Chen, "Conjunction of standing wave and resonance in asymmetric nanowires: a mechanism for thermal rectification and remote energy accumulation," *Scientific Reports*, vol. 5, 2015.
- [49] F. Pan, C. Li, X. Fu, F. Wang, Q. Sun, and Y. Jia, "Heat-pulse rectification in graphene Y junctions: A molecular dynamics simulations," *Physica E: Low-dimensional Systems and Nanostructures*, 2016.
- [50] J.-P. Eckmann and C. Mejía-Monasterio, "Thermal rectification in billiardlike systems," *Physical Review Letters*, vol. 97, p. 094301, 08/28/ 2006.
- [51] D. Segal, "Single mode heat rectifier: controlling energy flow between electronic conductors," *Physical Review Letters*, vol. 100, p. 105901, 03/13/ 2008.
- [52] L.-A. Wu and D. Segal, "Sufficient conditions for thermal rectification in hybrid quantum structures," *Physical Review Letters*, vol. 102, p. 095503, 03/06/ 2009.
- [53] X.-O. Chen, B. Dong, and X.-L. Lei, "Condensed matter: electronic structure, electrical, magnetic, and optical properties: thermal rectification effect of an interacting quantum dot," *Chinese Physics Letters*, vol. 25, pp. 3032-3035, 2008.
- [54] R. Scheibner, M. König, D. Reuter, A. D. Wieck, C. Gould, H. Buhmann, *et al.*, "Quantum dot as thermal rectifier," *New Journal of Physics*, vol. 10, p. 083016, 2008.
- [55] T. Ruokola, T. Ojanen, and A.-P. Jauho, "Thermal rectification in nonlinear quantum circuits," *Physical Review B*, vol. 79, p. 144306, 04/27/ 2009.
- [56] T. Ojanen, "Selection-rule blockade and rectification in quantum heat transport," *Physical Review B*, vol. 80, p. 180301, 11/18/ 2009.

- [57] G. Balasubramanian, I. K. Puri, M. C. Bohm, and F. Leroy, "Thermal conductivity reduction through isotope substitution in nanomaterials: predictions from an analytical classical model and nonequilibrium molecular dynamics simulations," *Nanoscale*, vol. 3, pp. 3714-3720, 2011.
- [58] G. Casati, C. Mejía-Monasterio, and T. Prosen, "Magnetically induced thermal rectification," *Physical Review Letters*, vol. 98, p. 104302, 2007.
- [59] S. Murad and I. K. Puri, "Thermal rectification in a fluid reservoir," *Applied Physics Letters*, vol. 100, p. 121907, 2012.
- [60] D. Bagchi, "Thermal rectification and negative differential thermal resistance in a driven two segment classical Heisenberg chain," *Journal of Physics: Condensed Matter*, vol. 25, p. 496006, 2013.
- [61] P. H. Guimarães, G. T. Landi, and M. J. de Oliveira, "Thermal rectification in anharmonic chains under an energy-conserving noise," *Physical Review E*, vol. 92, p. 062120, 2015.
- [62] G. T. Landi and M. J. de Oliveira, "Fourier's law from a chain of coupled anharmonic oscillators under energy-conserving noise," *Physical Review E*, vol. 87, p. 052126, 2013.
- [63] S. Suwunnarat, H. Li, R. Fleischmann, and T. Kottos, "Low-temperature linear thermal rectifiers based on Coriolis forces," *Physical Review E*, vol. 93, p. 042115, 2016.
- [64] C. Tso and C. Y. Chao, "Solid-state thermal diode with shape memory alloys," *International Journal of Heat and Mass Transfer*, vol. 93, pp. 605-611, 2016.
- [65] S. Globe and D. Dropkin, "Natural convection heat transfer in liquids confined by two horizontal plates and heated from below," *Journal of Heat Transfer*, vol. 81, pp. 24-28, 1959.
- [66] M. Groll, W. D. Munze, W. Supper, and C. J. Savage, "Development of a liquid-trap heat pipe thermal diode," *Journal of Spacecraft and Rockets*, vol. 16, pp. 195-202, 1979/07/01 1979.
- [67] J. Alario, "Cryogenic Thermal Diode Heat Pipes," Grumman Aerospace Corporation, NASA/AMES Research Center NASA CR-152, 268, 1979.
- [68] J. B. Boreyko, Y. Zhao, and C.-H. Chen, "Planar jumping-drop thermal diodes," *Applied Physics Letters*, vol. 99, p. 234105, 2011.
- [69] T. Hirayanagi, T. Tsukamoto, M. Esashi, and S. Tanaka, "Micro thermal diode with glass thermal insulation structure embedded in vapor chamber," *Journal of Physics: Conference Series*, vol. 476, p. 012019, 2013.
- [70] C. R. Otey, W. T. Lau, and S. Fan, "Thermal rectification through vacuum," *Physical Review Letters*, vol. 104, p. 154301, 04/13/ 2010.

- [71] H. Iizuka and S. Fan, "Rectification of evanescent heat transfer between dielectric-coated and uncoated silicon carbide plates," *Journal of Applied Physics*, vol. 112, p. 024304, 2012.
- [72] S. Basu and M. Francoeur, "Near-field radiative transfer based thermal rectification using doped silicon," *Applied Physics Letters*, vol. 98, p. 113106, 2011.
- [73] P. Ben-Abdallah and S.-A. Biehs, "Phase-change radiative thermal diode," *Applied Physics Letters*, vol. 103, p. 191907, 2013.
- [74] Y. Yang, S. Basu, and L. Wang, "Radiation-based near-field thermal rectification with phase transition materials," *Applied Physics Letters*, vol. 103, pp. 163101-163101-5, 2013.
- [75] L. Zhu, C. R. Otey, and S. Fan, "Ultrahigh-contrast and large-bandwidth thermal rectification in near-field electromagnetic thermal transfer between nanoparticles," *Physical Review B*, vol. 88, p. 184301, 2013.
- [76] L. P. Wang and Z. M. Zhang, "Thermal rectification enabled by near-field radiative heat transfer between intrinsic silicon and a dissimilar material," *Nanoscale and Microscale Thermophysical Engineering*, vol. 17, pp. 337-348, 2013/11/01 2013.
- [77] M. F. Modest, *Radiative heat transfer*: Academic Press, 2013.
- [78] E. Mascarenhas, D. Gerace, D. Valente, S. Montangero, A. Auffèves, and M. F. Santos, "A quantum optical valve in a nonlinear-linear resonators junction," *Europhysics Letters*, vol. 106, p. 54003, 2014.
- [79] M. Keidar, A. Shashurin, S. Delaire, X. Fang, and I. Beilis, "Inverse heat flux in double layer thermal metamaterial," *Journal of Physics D: Applied Physics*, vol. 48, p. 485104, 2015.
- [80] E. Mascarenhas, M. Santos, A. Auffèves, and D. Gerace, "A quantum rectifier in a one-dimensional photonic channel," *Physical Review A*, vol. 93, p. 043821, 2015.
- [81] G. Schaller, G. G. Giusteri, and G. L. Celardo, "Collective couplings: Rectification and supertransmittance," *Phys Rev E*, vol. 94, p. 032135, Sep 2016.
- [82] J. Cho, M. D. Losego, H. G. Zhang, H. Kim, J. Zuo, I. Petrov, *et al.*, "Electrochemically tunable thermal conductivity of lithium cobalt oxide," *Nature Communications*, vol. 5, 06/03/online 2014.
- [83] J. H. Cho, L. W. Weiss, C. D. Richards, D. F. Bahr, and R. F. Richards, "Power production by a dynamic micro heat engine with an integrated thermal switch," *Journal of Micromechanics and Microengineering*, vol. 17, p. S217, 2007.
- [84] T. Nast, G. Bell, and C. Barnes, "Development of gas gap cryogenic thermal switch," in *Proceedings of the Cryogenic Engineering Conference*, San Diego, CA, USA, 1982, pp. 1117-1124.

- [85] S. Vanoost, G. Bekaert, R. S. Bhatti, S. Scull, and C. I. Jewell, "A heat switch for space cryocooler applications," in *4th European Symposium on Space Environmental Control Systems*, 1991, pp. 209-216.
- [86] M. Wang, L. Yang, T. Yan, J. Cai, and J. Liang, "Development of a cryogenic thermal switch," in *International Cryocooler Conference*, Boulder, CO, USA, 2007, pp. 589-594.
- [87] I. Catarino, G. Bonfait, and L. Duband, "Neon gas-gap heat switch," *Cryogenics*, vol. 48, pp. 17-25, 2008.
- [88] I. Catarino and C. Paine, "3 He gas gap heat switch," *Cryogenics*, vol. 51, pp. 45-48, 2011.
- [89] D. A. Wolf, "Heat pipe thermal switch," NASA1983.
- [90] J. W. Nilsson and S. A. Riedel, *Electric Circuits*: Pearson Education, Limited, 2014.
- [91] J. Bardeen and W. H. Brattain, "The transistor, a semi-conductor triode," *Physical Review*, vol. 74, p. 230, 1948.
- [92] B. Li, L. Wang, and G. Casati, "Negative differential thermal resistance and thermal transistor," *Applied Physics Letters*, vol. 88, p. 143501, 2006.
- [93] K. Joulain, J. Drevillon, Y. Ezzahri, and J. Ordóñez-Miranda, "Quantum thermal transistor," *arXiv preprint arXiv:1602.04175*, 2016.
- [94] S. Narayana and Y. Sato, "Heat flux manipulation with engineered thermal materials," *Physical Review Letters*, vol. 108, p. 214303, 05/21/ 2012.
- [95] R. P. Bywaters and R. A. Griffin, "A gas-gap thermal switch for cryogenic applications," *Cryogenics*, vol. 13, pp. 344-349, 6// 1973.
- [96] D. J. Frank and T. C. Nast, "Getter-Activated Cryogenic Thermal Switch," in *Advances in Cryogenic Engineering*. vol. 31, R. W. Fast, Ed., ed: Springer US, 1986, pp. 933-940.
- [97] B. Marland, D. Bugby, and C. Stouffer, "Development and testing of advanced cryogenic thermal switch concepts," in *AIP Conference Proceedings*, 2000, pp. 837-846.
- [98] J. Cho, T. Wiser, C. Richards, D. Bahr, and R. Richards, "Fabrication and characterization of a thermal switch," *Sensors and Actuators A: Physical*, vol. 133, pp. 55-63, 1/8/ 2007.
- [99] O. Benafan and R. Vaidyanathan, "A shape memory alloy controlled heat pipe based thermal switch," in *ASME 2009 International Mechanical Engineering Congress and Exposition*, 2009, pp. 107-109.
- [100] T. Slater, P. Van Gerwen, E. Masure, F. Preud'homme, and K. Baert, "Thermomechanical characteristics of a thermal switch," *Sensors and Actuators A: Physical*, vol. 53, pp. 423-427, 5// 1996.

- [101] M. A. Beasley, S. L. Firebaugh, R. L. Edwards, A. C. Keeney, and R. Osiander, "MEMS thermal switch for spacecraft thermal control," in *Proceedings of the SPIE*, 2004, pp. 98-105.
- [102] A. R. McLanahan, C. D. Richards, and R. F. Richards, "A dielectric liquid contact thermal switch with electrowetting actuation," *Journal of Micromechanics and Microengineering*, vol. 21, p. 104009, 2011.
- [103] M. B. Duriska, S. M. Neville, B. Moubaraki, J. D. Cashion, G. J. Halder, K. W. Chapman, *et al.*, "A nanoscale molecular wwitch triggered by thermal, light, and guest perturbation," *Angewandte Chemie*, vol. 121, pp. 2587-2590, 2009.
- [104] K. E. Bulgrin, Y. S. Ju, G. P. Carman, and A. S. Lavine, "An investigation of a tunable magnetomechanical thermal switch," *Journal of Heat Transfer*, vol. 133, pp. 101401-101401, 2011.
- [105] M. A. Beasley, S. L. Firebaugh, R. L. Edwards, and A. C. Keeney, "Design and packaging for a microelectromechanical thermal switch radiator," in *Thermal and Thermomechanical Phenomena in Electronic Systems, 2004. ITherm'04. The Ninth Intersociety Conference on*, 2004, pp. 629-634.
- [106] T. Takashiro, E. Masayoshi, and T. Shuji, "A micro thermal switch with a stiffness-enhanced thermal isolation structure," *Journal of Micromechanics and Microengineering*, vol. 21, p. 104008, 2011.
- [107] G. Xiaobao, P. Pragnesh, N. Amitabh, and M. Dennis Desheng, "A self-adaptive thermal switch array for rapid temperature stabilization under various thermal power inputs," *Journal of Micromechanics and Microengineering*, vol. 21, p. 085018, 2011.
- [108] S. Murad and I. K. Puri, "Communication: A tractable design for a thermal transistor," *The Journal of Chemical Physics*, vol. 139, p. 151102, 2013.
- [109] S. Murad and I. K. Puri, "A thermal logic device based on fluid-solid interfaces," *Applied Physics Letters*, vol. 102, p. 193109, 2013.
- [110] C. Dames, "Solid-State Thermal Rectification With Existing Bulk Materials," *Journal of Heat Transfer*, vol. 131, pp. 061301-061301, 2009.
- [111] G. Hwang and T. Avanesian, "Multiscale Thermal Diode and Switch for Advanced Thermal Management Systems," in *Multiscale Thermal Transport in Energy Systems*, H. Y.-L. and Y. Zhang, Eds., ed New York: Nova Science Publisher Inc., 2016.
- [112] M. Hu, P. Keblinski, and B. Li, "Thermal rectification at silicon-amorphous polyethylene interface," *Applied Physics Letters*, vol. 92, p. 211908, 2008.
- [113] M. Kaviany, *Heat Transfer Physics*: Cambridge University Press, 2014.

- [114] G. S. Springer, "Heat transfer in rarefied gases," *Advances in heat transfer*, vol. 7, pp. 163-218, 1971.
- [115] D. D. Do, *Adsorption Analysis: Equilibria and Kinetics:(With CD Containing Computer Matlab Programs)* vol. 2: World Scientific, 1998.
- [116] S. Maruyama and T. Kimura, "A study on thermal resistance over a solid-liquid interface by the molecular dynamics method," *Thermal Science and Engineering*, vol. 7, pp. 63-68, 1999.
- [117] P. Spijker, A. J. Markvoort, P. A. Hilbers, S. V. Nedeja, and T. Abe, "Velocity correlations and accommodation coefficients for gas-wall interactions in nanochannels," in *Aip Conference Proceedings*, 2008, p. 659.
- [118] H. Heinz, R. Vaia, B. Farmer, and R. Naik, "Accurate simulation of surfaces and interfaces of face-centered cubic metals using 12–6 and 9–6 Lennard-Jones potentials," *The Journal of Physical Chemistry C*, vol. 112, pp. 17281-17290, 2008.
- [119] G. Hwang and M. Kaviani, "Molecular dynamics simulation of effective thermal conductivity of vapor-filled nanogap and nanocavity," *Journal of Applied Physics*, vol. 106, p. 24317, 2009.
- [120] C. Wang, J. Chen, J. Shiomi, and S. Maruyama, "A study on the thermal resistance over solid–liquid–vapor interfaces in a finite-space by a molecular dynamics method," *International Journal of Thermal Sciences*, vol. 46, pp. 1203-1210, 2007.
- [121] G. S. Hwang and M. Kaviani, "Molecular dynamics simulation of effective thermal conductivity of vapor-filled nanogap and nanocavity," *Journal of Applied Physics*, vol. 106, pp. 024317-024317-6, 2009.
- [122] Z. Liang, W. Evans, and P. Keblinski, "Equilibrium and nonequilibrium molecular dynamics simulations of thermal conductance at solid-gas interfaces," *Physical Review E*, vol. 87, p. 022119, 2013.
- [123] Z. Liang and P. Keblinski, "Parametric studies of the thermal and momentum accommodation of monoatomic and diatomic gases on solid surfaces," *International Journal of Heat and Mass Transfer*, vol. 78, pp. 161-169, 11// 2014.
- [124] H. Heinz, R. A. Vaia, B. L. Farmer, and R. R. Naik, "Accurate Simulation of Surfaces and Interfaces of Face-Centered Cubic Metals Using 12–6 and 9–6 Lennard-Jones Potentials," *The Journal of Physical Chemistry C*, vol. 112, pp. 17281-17290, 2008/11/06 2008.
- [125] S. Vanoost, G. Bekaert, R. Bhatti, S. Scull, and C. Jewell, "A heat switch for space cryocooler applications," in *In ESA, 4th European Symposium on Space Environmental Control Systems, Volume 1 p 209-216 (SEE N92-25828 16-18)*, 1991, pp. 209-216.
- [126] D. Wolf, "Heat pipe thermal switch," 1983.

- [127] T. Avanesian and G. Hwang, "Adsorption-Based Thermal Rectifier," in *ASME 2015 13th International Conference on Nanochannels, Microchannels, and Minichannels collocated with the ASME 2015 International Technical Conference and Exhibition on Packaging and Integration of Electronic and Photonic Microsystems*, 2015, pp. V001T04A024-V001T04A024.
- [128] T. Avanesian and G. Hwang, "Adsorption-controlled thermal diode: nonequilibrium molecular dynamics simulation," in *ASME 2016 14th International Conference on Nanochannels, Microchannels, and Minichannels*, Washington DC, USA, 2016.
- [129] L. Verlet, "Computer experiments" on classical fluids. I. Thermodynamical properties of Lennard-Jones molecules," *Physical review*, vol. 159, p. 98, 1967.
- [130] S. Nosé, "A unified formulation of the constant temperature molecular dynamics methods," *The Journal of chemical physics*, vol. 81, pp. 511-519, 1984.
- [131] W. G. Hoover, "Canonical dynamics: Equilibrium phase-space distributions," *Physical Review A*, vol. 31, pp. 1695-1697, 03/01/ 1985.
- [132] T. Schneider and E. Stoll, "Molecular-dynamics study of a three-dimensional one-component model for distortive phase transitions," *Physical Review B*, vol. 17, p. 1302, 1978.
- [133] S. Maruyama and T. Kimura, "A study on thermal resistance over a solid-liquid interface by the molecular dynamics method," *Therm. Sci. Eng.*, vol. 7, pp. 63-68, 1999.
- [134] S. Plimpton, "Fast parallel algorithms for short-range molecular dynamics," *Journal of computational physics*, vol. 117, pp. 1-19, 1995.
- [135] S. Plimpton, P. Crozier, and A. Thompson, "LAMMPS-large-scale atomic/molecular massively parallel simulator," *Sandia National Laboratories*, vol. 18, 2007.
- [136] K. Kaneko, T. Ohba, Y. Hattori, M. Sunaga, H. Tanaka, and H. Kanoh, "Role of gas adsorption in nanopore characterization," *Studies in Surface Science and Catalysis*, vol. 144, pp. 11-18, 2002.
- [137] E. Barsotti, S. P. Tan, S. Saraji, M. Piri, and J.-H. Chen, "A review on capillary condensation in nanoporous media: Implications for hydrocarbon recovery from tight reservoirs," *Fuel*, vol. 184, pp. 344-361, 2016.
- [138] S. Lowell, J. E. Shields, M. A. Thomas, and M. Thommes, *Characterization of porous solids and powders: surface area, pore size and density* vol. 16: Springer Science & Business Media, 2012.
- [139] J. Rouquerol, F. Rouquerol, P. Llewellyn, G. Maurin, and K. S. Sing, *Adsorption by powders and porous solids: principles, methodology and applications*: Academic press, 2013.

- [140] J. Appel, "Freundlich's adsorption isotherm," *Surface Science*, vol. 39, pp. 237-244, 1973/08/01 1973.
- [141] I. Langmuir, "THE ADSORPTION OF GASES ON PLANE SURFACES OF GLASS, MICA AND PLATINUM," *Journal of the American Chemical Society*, vol. 40, pp. 1361-1403, 1918/09/01 1918.
- [142] S. Brunauer, P. H. Emmett, and E. Teller, "Adsorption of gases in multimolecular layers," *Journal of the American chemical society*, vol. 60, pp. 309-319, 1938.
- [143] R. T. Yang, *Gas separation by adsorption processes*: Butterworth-Heinemann, 2013.
- [144] G. Halsey, "Physical adsorption on non-uniform surfaces," *The Journal of Chemical Physics*, vol. 16, pp. 931-937, 1948.
- [145] T. L. Hill, "Statistical Mechanics of Multimolecular Adsorption. III. Introductory Treatment of Horizontal Interactions. Capillary Condensation and Hysteresis1 a," *The Journal of Chemical Physics*, vol. 15, pp. 767-777, 1947.
- [146] J. Frenkel, "Kinetic Theory of LiquidsOxford Univ," *Press-1946*, 1946.
- [147] L. H. Cohan, "Sorption Hysteresis and the Vapor Pressure of Concave Surfaces," *Journal of the American Chemical Society*, vol. 60, pp. 433-435, 1938/02/01 1938.
- [148] P. H. Emmett and S. Brunauer, "The use of low temperature van der Waals adsorption isotherms in determining the surface area of iron synthetic ammonia catalysts," *Journal of the American Chemical Society*, vol. 59, pp. 1553-1564, 1937.
- [149] A. V. Neimark and P. I. Ravikovitch, "Capillary condensation in MMS and pore structure characterization," *Microporous and Mesoporous Materials*, vol. 44, pp. 697-707, 2001.
- [150] A. V. Neimark, P. I. Ravikovitch, M. Grün, F. Schüth, and K. K. Unger, "Pore size analysis of MCM-41 type adsorbents by means of nitrogen and argon adsorption," *Journal of colloid and interface science*, vol. 207, pp. 159-169, 1998.
- [151] J. Broekhoff and J. De Boer, "Studies on pore systems in catalysts: IX. Calculation of pore distributions from the adsorption branch of nitrogen sorption isotherms in the case of open cylindrical pores A. Fundamental equations," *Journal of Catalysis*, vol. 9, pp. 8-14, 1967.
- [152] M. W. Cole and W. Saam, "Excitation spectrum and thermodynamic properties of liquid films in cylindrical pores," *Physical Review Letters*, vol. 32, p. 985, 1974.
- [153] D. Nicholson, "Molecular theory of adsorption in pore spaces. Part 1.—Isotherms for simple lattice models," *Journal of the Chemical Society, Faraday Transactions 1: Physical Chemistry in Condensed Phases*, vol. 71, pp. 238-255, 1975.
- [154] F. Celestini, "Capillary condensation within nanopores of various geometries," *Physics Letters A*, vol. 228, pp. 84-90, 1997.

- [155] R. J.-M. Pellenq, B. Coasne, R. O. Denoyel, and O. Coussy, "Simple phenomenological model for phase transitions in confined geometry. 2. Capillary condensation/evaporation in cylindrical mesopores," *Langmuir*, vol. 25, pp. 1393-1402, 2009.
- [156] M. F. De Lange, T. J. Vlugt, J. Gascon, and F. Kapteijn, "Adsorptive characterization of porous solids: Error analysis guides the way," *Microporous and Mesoporous Materials*, vol. 200, pp. 199-215, 2014.
- [157] H. Ghasemi and C. Ward, "Surface tension of solids in the absence of adsorption," *The Journal of Physical Chemistry B*, vol. 113, pp. 12632-12634, 2009.
- [158] S. H. Zandavi and C. A. Ward, "Clusters in the adsorbates of vapours and gases: Zeta isotherm approach," *Physical Chemistry Chemical Physics*, vol. 16, pp. 10979-10989, 2014.
- [159] C. Wu, S. H. Zandavi, and C. Ward, "Prediction of the wetting condition from the Zeta adsorption isotherm," *Physical Chemistry Chemical Physics*, vol. 16, pp. 25564-25572, 2014.
- [160] D. Sullivan, "Van der Waals model of adsorption," *Physical Review B*, vol. 20, p. 3991, 1979.
- [161] D. Sullivan, "Surface tension and contact angle of a liquid–solid interface," *The Journal of Chemical Physics*, vol. 74, pp. 2604-2615, 1981.
- [162] R. Evans, U. M. B. Marconi, and P. Tarazona, "Fluids in narrow pores: Adsorption, capillary condensation, and critical points," *The Journal of chemical physics*, vol. 84, pp. 2376-2399, 1986.
- [163] R. Evans, U. M. B. Marconi, and P. Tarazona, "Capillary condensation and adsorption in cylindrical and slit-like pores," *Journal of the Chemical Society, Faraday Transactions 2: Molecular and Chemical Physics*, vol. 82, pp. 1763-1787, 1986.
- [164] W. Van Meegen and I. Snook, "Physical adsorption of gases at high pressure: III. Adsorption in slit-like pores," *Molecular Physics*, vol. 54, pp. 741-755, 1985.
- [165] W. J. Stroud, J. E. Curry, and J. H. Cushman, "Capillary condensation and snap-off in nanoscale contacts," *Langmuir*, vol. 17, pp. 688-698, 2001.
- [166] J. Lane and T. Spurling, "Monte Carlo simulation of the effects of adsorption on interparticle forces," *Australian Journal of Chemistry*, vol. 33, pp. 231-239, 1980.
- [167] J. Lane and T. Spurling, "The thermodynamics of a new type of surface transition," *Australian Journal of Chemistry*, vol. 34, pp. 1529-1533, 1981.
- [168] B. C. Freasier and S. Nordholm, "A generalized van der Waals model for solvation forces between solute particles in a colloidal suspension," *The Journal of chemical physics*, vol. 79, pp. 4431-4438, 1983.

- [169] B. Coasne, A. Grosman, C. Ortega, and M. Simon, "Adsorption in noninterconnected pores open at one or at both ends: a reconsideration of the origin of the hysteresis phenomenon," *Physical review letters*, vol. 88, p. 256102, 2002.
- [170] J. U. Keller, E. Robens, and C. d. F. von Hohenesche, "Thermogravimetric and sorption measurement techniques/instruments," *Studies in Surface Science and Catalysis*, vol. 144, pp. 387-394, 2002.
- [171] Y. He and N. A. Seaton, "Experimental and computer simulation studies of the adsorption of ethane, carbon dioxide, and their binary mixtures in MCM-41," *Langmuir*, vol. 19, pp. 10132-10138, 2003.
- [172] A. Grosman and C. Ortega, "Nature of capillary condensation and evaporation processes in ordered porous materials," *Langmuir*, vol. 21, pp. 10515-10521, 2005.
- [173] K. Morishige, H. Fujii, M. Uga, and D. Kinukawa, "Capillary critical point of argon, nitrogen, oxygen, ethylene, and carbon dioxide in MCM-41," *Langmuir*, vol. 13, pp. 3494-3498, 1997.
- [174] K. Morishige and Y. Nakamura, "Nature of adsorption and desorption branches in cylindrical pores," *Langmuir*, vol. 20, pp. 4503-4506, 2004.
- [175] J.-H. Yun, T. Düren, F. J. Keil, and N. A. Seaton, "Adsorption of methane, ethane, and their binary mixtures on MCM-41: experimental evaluation of methods for the prediction of adsorption equilibrium," *Langmuir*, vol. 18, pp. 2693-2701, 2002.
- [176] K. Morishige, T. Kawai, and S. Kittaka, "Capillary condensation of water in mesoporous carbon," *The Journal of Physical Chemistry C*, vol. 118, pp. 4664-4669, 2014.
- [177] S. Qiao, S. Bhatia, and D. Nicholson, "Study of hexane adsorption in nanoporous MCM-41 silica," *Langmuir*, vol. 20, pp. 389-395, 2004.
- [178] S. H. Zandavi and C. Ward, "Nucleation and growth of condensate in nanoporous materials," *Physical Chemistry Chemical Physics*, vol. 17, pp. 9828-9834, 2015.
- [179] S. H. Zandavi and C. Ward, "Characterization of the pore structure and surface properties of shale using the zeta adsorption isotherm approach," *Energy & Fuels*, vol. 29, pp. 3004-3010, 2015.
- [180] M. Alam, A. Clarke, and J. Duffy, "Capillary condensation and desorption of binary mixtures of N<sub>2</sub>- Ar confined in a mesoporous medium," *Langmuir*, vol. 16, pp. 7551-7553, 2000.
- [181] S. Zandavi and C. Ward, "Contact angles and surface properties of nanoporous materials," *Journal of colloid and interface science*, vol. 407, pp. 255-264, 2013.

- [182] L. Prasetyo, T. Horikawa, P. Phadungbut, S. J. Tan, D. Do, and D. Nicholson, "A GCMC simulation and experimental study of krypton adsorption/desorption hysteresis on a graphite surface," *Journal of Colloid and Interface Science*, vol. 478, pp. 402-412, 2016.
- [183] D. Frenkel and B. Smit, *Understanding molecular simulation: from algorithms to applications* vol. 1: Academic press, 2001.
- [184] P. Spijker, A. J. Markvoort, P. A. Hilbers, S. V. Nedeia, and T. Abe, "Velocity Correlations and Accommodation Coefficients for Gas-Wall Interactions in Nanochannels," in *AIP Conference Proceedings*, 2008, pp. 659-664.
- [185] S. Plimpton, A. Thompson, and P. Crozier, "Molecular Dynamics Simulations from SNL's Large-scale Atomic/Molecular Massively Parallel Simulator (LAMMPS)," 2007.
- [186] E. Lemmon, M. McLinden, and D. Friend, "Thermophysical properties of fluid systems," *NIST chemistry webbook, NIST standard reference database*, vol. 69, 2005.
- [187] M. Kruk and M. Jaroniec, "Accurate method for calculating mesopore size distributions from argon adsorption data at 87 K developed using model MCM-41 materials," *Chemistry of Materials*, vol. 12, pp. 222-230, 2000.
- [188] G. S. Hwang, M. Kaviani, J. T. Gostick, B. Kientiz, A. Z. Weber, and M. H. Kim, "Role of water states on water uptake and proton transport in Nafion using molecular simulations and bimodal network," *Polymer*, vol. 52, pp. 2584-2593, May 26 2011.
- [189] G. S. Hwang, M. Kaviani, J. H. Nam, M. H. Kim, and S. Y. Son, "Pore-Water Morphological Transitions in Polymer Electrolyte of a Fuel Cell," *Journal of The Electrochemical Society*, vol. 156, pp. B1192-B1200, October 1, 2009 2009.
- [190] X. Yang, D. Yu, and B. Cao, "Giant Thermal Rectification from Single-Carbon Nanotube–Graphene Junction," *ACS Applied Materials & Interfaces*, vol. 9, pp. 24078-24084, 2017/07/19 2017.
- [191] G. Lei, H. Cheng, H. Liu, and W. Rao, "Thermal rectification in asymmetric graphyne nanoribbons: A nonequilibrium molecular dynamics study," *Materials Letters*, vol. 189, pp. 101-103, 2017/02/15/ 2017.
- [192] A. Arora, T. Hori, T. Shiga, and J. Shiomi, "Thermal rectification in restructured graphene with locally modulated temperature dependence of thermal conductivity," *Physical Review B*, vol. 96, p. 165419, 10/10/ 2017.
- [193] M. Shavikloo and S. Kimiagar, "Thermal rectification in partially hydrogenated graphene with grain boundary, a non-equilibrium molecular dynamics study," *Computational Materials Science*, vol. 139, pp. 330-334, 2017/11/01/ 2017.
- [194] M. Romero-Bastida and R.-J. Marcelino, "Thermal rectification in one-dimensional mass-graded lattices with an on-site potential," *Journal of Physics A: Mathematical and Theoretical*, vol. 50, p. 015004, 2017.

- [195] C. Y. Tso and C. Y. H. Chao, "Solid-state thermal diode with shape memory alloys," *International Journal of Heat and Mass Transfer*, vol. 93, pp. 605-611, 2// 2016.
- [196] P. R. Gaddam, S. T. Huxtable, and W. A. Ducker, "A liquid-state thermal diode," *International Journal of Heat and Mass Transfer*, vol. 106, pp. 741-744, 3// 2017.
- [197] T. S. Komatsu and N. Ito, "Thermal diode utilizing asymmetric contacts to heat baths," *Physical Review E*, vol. 81, p. 010103, 2010.
- [198] M. Elzouka and S. Ndao, "High Temperature Near-Field NanoThermoMechanical Rectification," *Scientific Reports*, vol. 7, 2017.
- [199] T. Avanesian and G. Hwang, "Adsorption-based thermal rectifier," presented at the Proceedings of ASME 2015 13th International Conference on Nanochannels, Microchannels, and Minichannels (ICNMM2015), San Francisco, 2015.
- [200] N. A. Voinov, D. A. Zemtsov, and O. P. Zhukova, "Study of thermal rectification in a column with low mass transfer on the steps," *Theoretical Foundations of Chemical Engineering*, vol. 51, pp. 191-198, March 01 2017.
- [201] T. Avanesian and G. Hwang, "Thermal switch using controlled capillary transition in heterogeneous nanostructures," *International Journal of Heat and Mass Transfer*, Submitted, 2017.
- [202] C. J. Fu and Z. M. Zhang, "Nanoscale radiation heat transfer for silicon at different doping levels," *International Journal of Heat and Mass Transfer*, vol. 49, pp. 1703-1718, 5// 2006.
- [203] A. Narayanaswamy, S. Shen, L. Hu, X. Chen, and G. Chen, "Breakdown of the Planck blackbody radiation law at nanoscale gaps," *Applied Physics A: Materials Science & Processing*, vol. 96, pp. 357-362, 2009.
- [204] S. Basu, Z. Zhang, and C. Fu, "Review of near-field thermal radiation and its application to energy conversion," *International Journal of Energy Research*, vol. 33, pp. 1203-1232, 2009.
- [205] S. Sarkar and R. P. Selvam, "Molecular dynamics simulation of effective thermal conductivity and study of enhanced thermal transport mechanism in nanofluids," *Journal of applied physics*, vol. 102, p. 074302, 2007.
- [206] T. Avanesian and G. Hwang, "Adsorption-Controlled Thermal Switch Using Nonequilibrium Molecular Dynamics Simulation," in *ASME 2016 International Mechanical Engineering Congress and Exposition*, 2016, p. V010T13A021.
- [207] T. Avanesian and G. Hwang, "Thermal diode in gas-filled nanogap with heterogeneous surfaces using nonequilibrium molecular dynamics simulation," *Journal of Applied Physics*, vol. 120, p. 165306, 2016.

- [208] T. Avanesian and G. Hwang, "Nanostructure-driven thermal switch using molecular simulations," presented at the Submitted to Proceedings of ASME 2017 International Mechanical Engineering Congress and Exposition (IMECE2017), Tampa, FL, 2017.
- [209] T. Avanesian and G. Hwang, "Adsorption and capillary transition in heterogeneous nanostructures using Grand Canonical Monte Carlo simulation," *International Journal of Heat and Mass Transfer, Submitted*, 2017.
- [210] X. Geng, P. Patel, and D. D. Meng, "A self-adaptive thermal switch array to stabilize the temperature of MEMS devices," in *Micro Electro Mechanical Systems (MEMS), 2010 IEEE 23rd International Conference on*, 2010, pp. 148-151.
- [211] Y. Yang, S. Basu, and L. Wang, "Vacuum thermal switch made of phase transition materials considering thin film and substrate effects," *Journal of Quantitative Spectroscopy and Radiative Transfer*, vol. 158, pp. 69-77, 2015.
- [212] V. Krishnan, J. Singh, T. Woodruff, W. Notardonato, and R. Vaidyanathan, "A shape memory alloy based cryogenic thermal conduction switch," in *AIP Conference Proceedings*, 2004, pp. 26-33.
- [213] X. Gou, H. Ping, Q. Ou, H. Xiao, and S. Qing, "A novel thermoelectric generation system with thermal switch," *Applied Energy*, vol. 160, pp. 843-852, 2015.
- [214] R. McCarty, D. Monaghan, K. Hallinan, and B. Sanders, "Experimental verification of thermal switch effectiveness in thermoelectric energy harvesting," *Journal of thermophysics and heat transfer*, vol. 21, pp. 505-511, 2007.
- [215] B. Marland, D. Bugby, and C. Stouffer, "Development and testing of an advanced cryogenic thermal switch and cryogenic thermal switch test bed," *Cryogenics*, vol. 44, pp. 413-420, 2004.
- [216] J.-H. He, S. Singamaneni, C. H. Ho, Y.-H. Lin, M. E. McConney, and V. V. Tsukruk, "A thermal sensor and switch based on a plasma polymer/ZnO suspended nanobelt bimorph structure," *Nanotechnology*, vol. 20, p. 065502, 2009.
- [217] K. Chunhui, C. Liubiao, L. Sixue, Z. Yuan, and W. Junjie, "A 63 K phase change unit integrating with pulse tube cryocoolers," in *IOP Conference Series: Materials Science and Engineering*, 2017, p. 012040.
- [218] M. Criado-Sancho and D. Jou, "A simple model of thermoelastic heat switches and heat transistors," *Journal of Applied Physics*, vol. 121, p. 024503, 2017.
- [219] W.-R. Zhong, D.-Q. Zheng, and B. Hu, "Thermal control in graphene nanoribbons: thermal valve, thermal switch and thermal amplifier," *Nanoscale*, vol. 4, pp. 5217-5220, 2012.

- [220] A. O. Christensen, J. Jacob, C. Richards, D. Bahr, and R. Richards, "Fabrication and characterization of a liquid-metal micro-droplet thermal switch," in *TRANSDUCERS, Solid-State Sensors, Actuators and Microsystems, 12th International Conference on, 2003*, 2003, pp. 1427-1430.
- [221] L. Weiss, J. Cho, K. McNeil, C. Richards, D. Bahr, and R. Richards, "Characterization of a dynamic micro heat engine with integrated thermal switch," *Journal of Micromechanics and Microengineering*, vol. 16, p. S262, 2006.
- [222] J. Cho, C. Richards, D. Bahr, J. Jiao, and R. Richards, "Evaluation of contacts for a MEMS thermal switch," *Journal of Micromechanics and Microengineering*, vol. 18, p. 105012, 2008.
- [223] J.-X. Wang, H.-S. Zhang, Y.-Z. Li, S.-N. Wang, Y.-N. Zhang, and M.-L. Zhong, "Performance analysis of a self-driven adaptive cold-plate, an experimental approach," in *Advanced Intelligent Mechatronics (AIM), 2016 IEEE International Conference on, 2016*, pp. 1503-1508.
- [224] H.-M. Chang and H.-J. Kim, "Development of a thermal switch for faster cool-down by two-stage cryocooler," *Cryogenics*, vol. 40, pp. 769-777, 2000.
- [225] J. Gong, G. Cha, and Y. S. Ju, "Thermal switches based on coplanar EWOD for satellite thermal control," in *Micro Electro Mechanical Systems, 2008. MEMS 2008. IEEE 21st International Conference on, 2008*, pp. 848-851.
- [226] M. Rasekh, S. Khadem, and A. Toghræe, "NEMS thermal switch operating based on thermal expansion of carbon nanotubes," *Physica E: Low-dimensional Systems and Nanostructures*, vol. 59, pp. 210-217, 2014.
- [227] H. Zhang, M. Mi, J. Miao, L. Wang, Y. Chen, T. Ding, *et al.*, "Development and on-orbit operation of loop heat pipes on chinese circumlunar return and reentry spacecraft," *Journal of Mechanical Science and Technology*, vol. 31, pp. 2597-2605, 2017.
- [228] F. Zhou, Y. Liu, S. N. Joshi, E. M. Dede, X. Chen, and A. Justin, "Vapor chamber with thermal diode and switch functions," in *Thermal and Thermomechanical Phenomena in Electronic Systems (ITherm), 2017 16th IEEE Intersociety Conference on, 2017*, pp. 521-528.
- [229] O. Ilic, M. Jablan, J. D. Joannopoulos, I. Celanovic, H. Buljan, and M. Soljačić, "Near-field thermal radiation transfer controlled by plasmons in graphene," *Physical Review B*, vol. 85, p. 155422, 2012.
- [230] W. Gu, G.-H. Tang, and W.-Q. Tao, "Thermal switch and thermal rectification enabled by near-field radiative heat transfer between three slabs," *International Journal of Heat and Mass Transfer*, vol. 82, pp. 429-434, 2015.

- [231] R. Bosisio, S. Valentini, F. Mazza, G. Benenti, R. Fazio, V. Giovannetti, *et al.*, "Magnetic thermal switch for heat management at the nanoscale," *Physical Review B*, vol. 91, p. 205420, 2015.
- [232] E. C. Cuansing and J.-S. Wang, "Transient behavior of heat transport in a thermal switch," *Physical Review B*, vol. 81, p. 052302, 2010.
- [233] M. Royo, A. Antidormi, and R. Rurali, "A Thermal Switch for Coherent Phonons Based on a Molecular Junction," *The Journal of Physical Chemistry C*, vol. 121, pp. 10571-10576, 2017.
- [234] B. Sothmann, F. Giazotto, and E. M. Hankiewicz, "High-efficiency thermal switch based on topological Josephson junctions," *New Journal of Physics*, vol. 19, p. 023056, 2017.
- [235] Y. Zhang, X. Zhang, Z. Ye, G. Lin, and J. Chen, "Three-terminal quantum-dot thermal management devices," *Applied Physics Letters*, vol. 110, p. 153501, 2017.
- [236] P. W. Bridgman, "The thermal conductivity of liquids under pressure," in *Proceedings of the American Academy of Arts and Sciences*, 1923, pp. 141-169.
- [237] T. Avanesian and G. Hwang, "Adsorption and Capillary Condensation in Nanogap With Nanoposts," in *ASME 2017 Heat Transfer Summer Conference*, 2017, pp. V002T13A008-V002T13A008.
- [238] P. Kapitza, "Zh Eksp Theor Fiz 11 1," *J Phys USSR*, vol. 4, p. 181, 1941.
- [239] E. T. Swartz and R. O. Pohl, "Thermal boundary resistance," *Reviews of modern physics*, vol. 61, p. 605, 1989.
- [240] F. Marquier, K. Joulain, J. P. Mulet, R. Carminati, and J. J. Greffet, "Engineering infrared emission properties of silicon in the near field and the far field," *Optics Communications*, vol. 237, pp. 379-388, 7/15/ 2004.
- [241] S. Basu, B. J. Lee, and Z. M. Zhang, "Near-Field Radiation Calculated With an Improved Dielectric Function Model for Doped Silicon," *Journal of Heat Transfer*, vol. 132, pp. 023302-023302-7, 2009.
- [242] M. Lim, S. S. Lee, and B. J. Lee, "Near-field thermal radiation between graphene-covered doped silicon plates," *Optics Express*, vol. 21, pp. 22173-22185, 2013/09/23 2013.
- [243] M. Lim, S. S. Lee, and B. J. Lee, "Near-field thermal radiation between doped silicon plates at nanoscale gaps," *Physical Review B*, vol. 91, p. 195136, 05/26/ 2015.